Three-dimensional intensity reconstruction in single-particle experiments

A spherical symmetry approach

Julien Flamant

October 2015

Master of Philosophy

Department of Electrical and Electronic Engineering
The University of Melbourne

Submitted in total fulfillment of the degree

Abstract

The ability to decipher the three-dimensional structures of biomolecules at high resolution will greatly improve our understanding of the biological machinery. To this aim, X-ray crystallography has been used by scientists for several decades with tremendous results. This imaging method however requires a crystal to be grown, and for most interesting biomolecules (proteins, viruses) this may not be possible. The single-particle experiment was proposed to address these limitations, and the recent advent of ultra-bright X-ray Free Electron Lasers (XFELs) opens a new set of opportunities in biomolecular imaging.

In the single-particle experiment, thousands of diffraction patterns are recorded, where each image corresponds to an unknown, random orientation of individual copies of the biomolecule. These noisy, unoriented two-dimensional diffraction patterns need to be then assembled in three-dimensional space to form the three-dimensional intensity function, which characterizes completely the three-dimensional structure of the biomolecule.

This work focuses on geometrical variations of an existing algorithm, the Expansion-Maximization-Compression (EMC) algorithm introduced by Loh and Elser. The algorithm relies upon an expectation-maximization method, by maximizing the likelihood of an intensity model with respect to the diffraction patterns. The contributions of this work are (i) the redefinition of the EMC algorithm in a spherical design, motivated by the intrinsic properties of the intensity function, (ii) the utilisation of an orthonormal harmonic basis on the three-dimensional ball which allows a sparse representation of the intensity function, (iii) the scaling of the EMC parameters with the desired resolution, increasing computational speed and (iv) the intensity error is analysed with respect to the EMC parameters.

Declaration

This is to certify that:

- The thesis comprises only my original work towards the Master of Philosophy degree except where indicated,
- Due acknowledgement has been made in the text to all other material used,
- This document is fewer than 50 000 words in length, exclusive of tables, maps, bibliography and appendices as approved by the Research Higher Degrees Committee.

Julien Flamant

Acknowledgments

I am pleased to recognize the constant help and support of many people who have made this year at The University of Melbourne a tremendous experience. First, I am very grateful to my thesis supervisors Nicolas Le Bihan, Andrew Martin and Jonathan Manton for their encouragements and advice along this work.

I would like to thank Professor Jonathan Manton for welcoming me in the Electrical Engineering department, and for his constant support during my year in Melbourne. Andrew Martin's expertise in X-ray Physics has been extremely beneficial to me, as well as all his valuable comments on the work presented.

Nicolas Le Bihan's support during this Master of Philosophy has been tremendous, and his dedication in the final writing process helped a lot to improve the readability of this manuscript. I look forward to continue working together during my PhD thesis.

Coffee breaks (and more!) with Vincent Crocher and Nicolas were a great source of inspiration; I am still thinking about the long black - americano paradox...

Life in the lab would not be the same without fellow PhD and MPhil students. I wish good luck to those who just started, and those who are about to finish. Thumbs up especially to Adel, Ahvand, Christopher, Daniel, Hasan, Majid, Roghieh and Yasmeen, as well as Michael.

Finally, I am grateful to my parents for their constant support during this year abroad. They have always encouraged me during my studies, and I owe them a lot for all they gave me. This work is dedicated to them. And because this work could not be here today without her understanding, my deepest thoughts are for Laura. Although it is nothing compared to all you already gave to me, Laura merci ...

À mes parents,
À Laura

Contents

List of Figures

[12] David M Paganin. *Coherent X-ray optics*. Oxford University Press, 2006.

CHAPTER 1

Introduction

1.1 Deciphering the structure of biomolecules with single-particle imaging

1.1.1 Motivation

Biological components, such as proteins or viruses, are driven by processes operating at atomic scale; therefore the knowledge of the precise three-dimensional structure of these biological components would provide a crucial understanding of the interaction and the role of each sub-component. The potential applications are numerous, from more accurate simulations of the biochemical machinery to the design of new materials with optimized properties.

Determination of high-resolution structures resolved at spatial atomic resolution requires the use of probes with a sensitivity comparable to the atomic scale.[1] Several candidates fulfill this requirement, from the Atomic Force Microscope (AFM) to the short wavelength offered by neutrons, electrons or X-rays.

One of the most popular tools used in structure determination is X-ray crystallography. This technique has successfully led to the determination of atomically-resolved protein structures in the last few decades, and is one of the key contribution of physical sciences to life sciences.[2] X-ray crystallography relies on the ability to bind biomolecules in a repetiting pattern, thus creating a crystal. The crystal is then used to amplify the incoming X-ray radiation, leading to an ensemble diffraction picture which can be eventually inverted to obtain the individual protein structure.

This method suffers from several drawbacks, the most critical step being the ability to grow a crystal. Unfortunately growing a crystal from an arbitrary molecule is far from trivial, and it is believed that it may be impossible in many cases, especially for membrane proteins. It was proposed to overcome this limitation using microscopic approaches similar to those used in electron microscopy,[1,3] however designing efficient X-rays lenses is a challenging problem.

Coherent X-ray diffraction imaging, also known as diffraction microscopy has been introduced at the end of the last century in order to overcome the limitation of X-ray crystallography.[4,5] This method relies upon the measurement of the far-field scattered intensity of a non-crystalline and isolated object.[6] The achievable resolution only depends on the wavelength and the maximum scattering angle available on the detector. This lensless imaging technique however requires intense and bright X-ray sources to obtain high-resolution images of biomolecule structures.

X-ray Free Electron Lasers (XFELs) carry the hope of making atomic resolution accessible. These new X-ray sources are more than 10^9 times brighter in peak power than the best synchrotron sources available today[7] and provide more than 10^{12} photons in pulses lasting less than few femtoseconds[8] (fs) (1 fs = 10^{-15} s). As of today, numerous XFELs facilities have been built; SACLA in Japan, FLASH in Germany, FERMI in Italy, and the LCLS in Stanford. The most powerful XFEL facility is expected to be the European XFEL, which is still in construction in Hamburg, Germany, with a operational date planned to be 2017.

The new techniques of coherent X-ray diffraction imaging, alongside the exceptional peak power of XFELs have opened a totally new area of research, at the edge of the physical, life and computer

[1] Anton Barty, Jochen Küpper, and Henry N Chapman. *Annual review of physical chemistry*, **64**: 415–435, 2013.
[2] VL Shneerson, A Ourmazd, and DK Saldin. *Acta Crystallographica A*, **64**: 303–315, 2008.
[3] Weilun Chao et al. *Nature*, **435**: 1210–1213, 2005.
[4] D. Sayre and H. N. Chapman. *Acta Crystallographica Section A*, **51**: 237–252, 1995.
[5] D. Sayre, H. N. Chapman, and J. Miao. *Acta Crystallographica Section A*, **54**: 232–239, 1998.
[6] Henry N Chapman et al. *JOSA A*, **23**: 1179–1200, 2006.
[7] Andrew V Martin and Ne-Te Duane Loh. *Synchrotron Radiation News*, **26**: 11–19, 2013.
[8] KJ Gaffney and HN Chapman. *Science*, **316**: 1444–1448, 2007.

sciences. In the following, we describe the single-particle experiment proposed to achieve high-resolution reconstruction of biomolecules.

Remark In this work, we use the words *biomolecule*, *protein* and *molecule* interchangeably.

1.1.2 The single-particle experiment

The single-particle experiment was originally proposed by Neutze *et al.* [9] as a method to overcome the limitations of X-ray crystallography. We briefly describe here the main ideas behind the single-particle experiment.

The principle of the experiment is simple: a pulsed train of X-ray photons illuminate a synchronized train of identical single proteins. Ideally only one copy of the considered protein is injected in front of the beam. The photons scattered by the protein are recorded on a detector, located in the far-field. Only one diffraction pattern per protein can be recorded since the intensity of the beam is so high that the molecule is destroyed by a Coulomb explosion within a few tens of femtoseconds. Moreover each diffraction pattern corresponds to an unknown random orientation of the molecule.

Using a pulsed train of photons with a faster dynamic than the radiation-damage process allows to obtain almost damage-free diffraction patterns.[9] Typically the pulses last about 5-15 fs, whereas the radiation damage effects start to occur significantly at 20-30 fs. However recent research suggests that imaging of single molecules is possible with 30-50 fs pulses.[10]

The mathematical relation between the protein structure, *i.e.* its electron density function, and the intensity measured on the detector is well known. The Fourier transform of the electron density function gives the molecular transform, which is related to the three-dimensional intensity function by its square magnitude and up to a scaling factor. Each diffraction pattern corresponds to a two-dimensional slice trough the three-dimensional intensity function, which is defined in reciprocal space. This is a consequence of the Fourier projection-slice theorem, which states that the 2D - Fourier transform of a projection in real space is equivalent to a 2D slice of the 3D - Fourier transform in reciprocal space. Thus provided that one is able to recover the relative orientation of each molecule, it is possible to reconstruct the three-dimensional intensity function in reciprocal space by associating each diffraction pattern with the corresponding orientation.

In practice, it is impossible to measure the actual orientation of the molecule, and computing tools have to be developed instead. Furthermore the radiation-damage curse limits the number of photons recorded on the detector, and up to millions of diffraction patterns may have to be acquired to reconstruct the molecule structure. This has lead to the development of numerous intensity reconstruction algorithms, which we briefly describe in section 1.3.1.

In order to determine the molecule structure, we need both the intensity and the phase of the Fourier transform of the electron density; however in the single-particle experiment only the intensity is measured. The phase has to be retrieved, so that the reconstructed molecule structure is unique. The so-called phase retrieval procedures are quickly discussed in section 1.3.2.

Getting the single-particle experiment to work is a tremendous challenge. The several issues raised by the experimental complexity will probably take a few years to be solved. Also since beamtime is sparsely allocated, theoretical work has to mainly rely upon simulated data, as it is the case for the work presented in this manuscript. The next section introduces the physical model for the single-particle experiment, as well as the simulation methods.

1.2 Single-particle experiment physics

We introduce the physical model of the single-particle experiment, and discuss the geometric properties of the three-dimensional intensity function. We give also practical expressions for the simulation of diffraction patterns, and discuss the different assumptions made throughout our approach.

[9] Richard Neutze et al. *Nature*, **406**: 752–757, 2000.
[10] Andrew V Martin et al. *arXiv preprint arXiv:1502.00737*, , 2015.

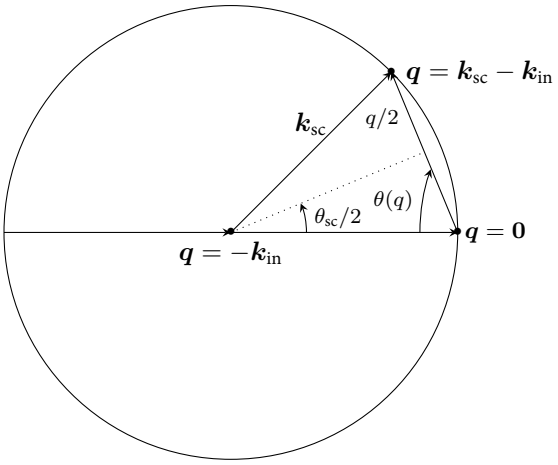

Figure 1.1 : Scattering geometry and Ewald sphere construction.

1.2.1 X-ray scattering and intensity model

X-ray interaction with matter

When X-rays photons are in the vicinity of an atom, several processes may occur. At typical energies available at XFEL facilities, $E = 1.2$ keV to $E = 12$ keV which correspond to wavelengths $\lambda = 10$ Å and $\lambda = 1$ Å, the predominant physical process is *absorption*. That is, an incoming photon has a non-zero probability to disappear from the system by interaction with the atom electronic structure. Another process is *photon scattering*, where the photon can change its direction and energy. In that case, the photon does not disappear from the system.
Absorption primary occurs by *photo-ionization*. When a photon falls upon an electron, this electron may be ejected outside the atom while the photon disappears. This electron can then hit other electrons and lead to new ionizations, until the energy of the ejected electron becomes sufficiently small to avoid the emission of secondary electrons or until the photoelectron escapes the sample, which is more likely for a small molecule. Since X-rays principally interact with inner shell electrons, several processes may arise after the photo-ionization. One electron of an upper-shell can relax into an inner-shell with fluorescence. Another process is auto-ionization: when the upper-shell electron relax into the inner-shell vacancy, another electron from the upper-shell can be ejected: this phenomenon is known as *Auger decay*.
Scattering can be either elastic or inelastic. In elastic scattering, the photon does not lose energy, and therefore incoming photon wavelength and scattered photon wavelength are identical. We will describe elastic scattering in detail in the sections below. Inelastic scattering occurs when a part of the incoming photon energy is absorbed, and then the scattered photon has a larger wavelength. We shall note here that in the context of XFELs, the coherence can not be conserved in the case of inelastic scattering, as the wavelength changes. Elastic scattering however conserves optical coherence, and therefore we will concentrate our efforts on the study of elastic scattering, as it represents the *signal* we shall consider to obtain the 3D structure of the molecule. The other phenomenons – fluorescence, Auger Decay, inelastic scattering – will be considered as a global noise.

The intensity model

We are now interested in modeling the (elastic) scattered intensity of the incoming X-ray beam by a biomolecule. Two complementary approaches exist; the full quantum derivation, which uses the second quantization framework and Fermi golden rule to find an expression of the scattered intensity I, and a semi-classical perspective which derivates the intensity model step by step, from the free electron to the complete biomolecule. The quantum calculations have been presented by Santra in a PhD tutorial,[11] and will not be reproduced here. However, we choose to introduce a perhaps more intuitive calculation, which works step-by-step and emphasizes the link between the scattered intensity and Fourier analysis. The incoming beam has wavevector $\boldsymbol{k}_{\mathrm{in}}$, which is assumed to remain constant. The

[11] ROBIN SANTRA. *Journal of Physics B: Atomic, Molecular and Optical Physics*, **42**: 023001, 2009.

direction of the scattered wave is given by the wavevector $\boldsymbol{k}_{\text{sc}}$, and we denote by θ_{sc} the angle of scattering. We introduce the scattering momentum $\boldsymbol{q} = \boldsymbol{k}_{\text{sc}} - \boldsymbol{k}_{\text{in}}$, and therefore parametrize reciprocal space in terms of this vector. Since we only consider the elastic scattering case, no energy is lost during the scattering process so that $\|\boldsymbol{k}_{\text{sc}}\| = \|\boldsymbol{k}_{\text{in}}\|$. Geometrically, this means that the scattering wavevector $\boldsymbol{k}_{\text{sc}}$ draws a sphere in reciprocal space, centered at $\boldsymbol{q} = -\boldsymbol{k}_{\text{in}}$ and with radius $\boldsymbol{k}_{\text{in}} = \boldsymbol{k}_{\text{sc}} = 2\pi/\lambda$, known as the Ewald sphere.[12–14] The notations and the constructions are drawn on figure 1.1.

The Ewald sphere has a particular importance. For a given orientation of the molecule, that is for a given value of incident beam wavevector $\boldsymbol{k}_{\text{in}}$ only particular values of the intensity $I(\boldsymbol{q})$ can be obtained, *i.e.* those such that the scattering momentum $\boldsymbol{q}$ lies on the Ewald sphere. Therefore, we say that the *Ewald sphere samples the three-dimensional reciprocal space*. Rotating the molecule about its own frame, or equivalently rotating the incoming beam wavevector about the origin of the reciprocal space leads to rotated Ewald sphere, and thus to a different sampling of the reciprocal space. One may eventually reconstruct the whole reciprocal space by taking *enough* rotated views of the biomolecule. This question is addressed later on, in section 1.2.3.

Before moving to the expression of the intensity $I(\boldsymbol{q})$, we give the relation between the angle of scattering θ_{sc} and the norm of the scattering momentum $q = \|\boldsymbol{q}\|$. Simple geometry from figure 1.1 yields to the relation

$$q = \frac{4\pi}{\lambda} \sin \frac{\theta_{\text{sc}}}{2} = q_{\text{max}} \cdot \sin \frac{\theta_{\text{sc}}}{2}, \tag{1.1}$$

where we have introduced the quantity q_{max} for convenience. The above equation is valid for the whole interval of definition of θ_{sc}, that is $[0, \pi]$. The scattering momentum is equal to 0 when there is no scattering ($\theta_{\text{sc}} = 0$) whereas the norm of the scattering momentum reaches its maximum q_{max} for $\theta_{\text{sc}} = \pi$ which corresponds to the backscattering case. We eventually note that q is usually given in Å^{-1}, since it is common in X-ray physics to give the wavelength λ in angströms, where 1 Å$= 10^{-10}$ m.

The scattered intensity as a function of the scattering momentum $\boldsymbol{q}$ can now be derived. First, it is common in X-ray physics to express all the intensities in terms of *Thomson* units I_T, which corresponds to the intensity scattered by a free electron under the same incoming beam conditions:

$$I_T = \pi r_e^2 \mathcal{P}(\theta_{\text{sc}}) I_0, \tag{1.2}$$

where $r_e = 2.82\ 10^{-15}$ m is the classical radius of the electron, $\mathcal{P}(\theta_{\text{sc}})$ is a function depending on the polarization of the incident beam, and I_0 is the incident beam intensity, supposed constant. The polarization factor $\mathcal{P}(\theta_{\text{sc}})$, although depending on the scattering angle θ_{sc}, does not play an important role in the forthcoming study of scattering by a biomolecule, since it is independent of the particle itself.

In the case of atoms, the scattered intensity can be expressed by introducing a function of the scattering momentum, the *scattering factor* $f(\boldsymbol{q})$ which modulates the amplitude of the scattered wave for a given scattering momentum $\boldsymbol{q}$. Each atom scatters X-rays differently, and hence the scattering factor is a signature of the electron density of the atom $\rho^{(\text{at})}$. The scattering factor can be defined in mathematical terms as the Fourier transform of the electron density of the atom:

$$f(\boldsymbol{q}) = \int \rho^{(\text{at})}(\boldsymbol{r}) \exp(i\boldsymbol{q} \cdot \boldsymbol{r}) \mathrm{d}^3\boldsymbol{r}, \tag{1.3}$$

where $\boldsymbol{r}$ designates the position vector in the frame of reference of the atom. The scattering factors can be either computed theoretically or determined experimentally.[15] However practical expressions are tabulated mixing both methods.[16] In a first approximation, the scattering factors only depend on the norm q of the scattering momentum, leading to the definition of the isotropic scattering factor f^0. The scattered intensity from a single atom is then, in Thomson units:

$$I^{(\text{at})}(q) = |f^0(q)|^2 I_T. \tag{1.4}$$

[12] DAVID M PAGANIN. *Coherent X-ray optics*. Oxford University Press, 2006.
[13] M. H. PIRENNE. *The diffraction of X-Rays and electrons by free molecules*. Cambridge University Press, 1946.
[14] BERTRAM EUGENE WARREN. *X-ray Diffraction*. Courier Dover Publications, 1969.
[15] THEO HAHN et al. *International tables for crystallography*. D. Reidel Publishing Company, 2005.
[16] D WAASMAIER and A KIRFEL. *Acta Crystallographica Section A: Foundations of Crystallography*, **51**: 416–431, 1995.

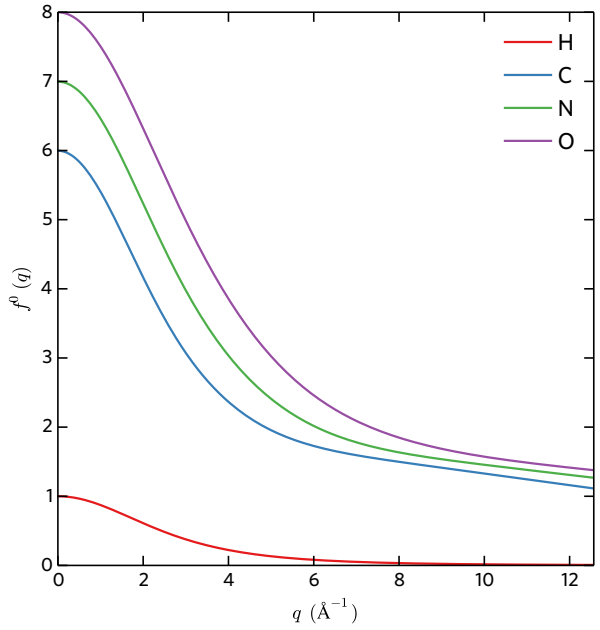

Figure 1.2 : Isotropic scattering factors f^0 for the most common atoms in biomolecules hydrogen (H), carbon (C), nitrogen (N) and oxygen (O). Scattering momentum norm ranges from 0 to 4π, the upper bound corresponding to the backscattering case with wavelength $\lambda = 1$ Å.

The isotropic scattering factors f^0 (henceforth denoted as scattering factors) are often computed from their Cromer-Mann coefficients[17] which give f^0 as a weighted sum of exponential functions. We have presented on figure 1.2 scattering factors for the most common elements in biomolecules: hydrogen, carbon, nitrogen and oxygen. A first remark is that the value of f^0 at the origin is equal to the atomic number of the element: this is a direct consequence of the definition of the scattering factor, as seen in (1.3). As q increases, the value of f^0 decreases, showing that the amplitude of the scattered wave decreases as the scattering angle increases. In quantum mechanics, we say that the probability that a photon is scattered decreases as the scattering angle gets larger.

Finally, our interest focuses on the scattered intensity from a given biomolecule. Just like the definition of the scattering factor for an atom, it is possible to define the *molecular scattering factor* or *molecular transform* $F(\boldsymbol{q})$ as the Fourier transform of the electron density of the biomolecule $\rho^{(\text{mol})}$:

$$F(\boldsymbol{q}) = \int \rho^{(\text{mol})}(\boldsymbol{r}) \exp(i\boldsymbol{q}\cdot\boldsymbol{r}) \mathrm{d}^3\boldsymbol{r}. \tag{1.5}$$

The question is, how does this expression link with the scattering factor of each atom in the molecule ? Several ways exist to deal with this issue. The simplest is to consider that all chemical bond effects on the electron density can be neglected, and to view each atom as isolated from its neighbors. With this approximation, the electron density $\rho^{(\text{mol})}$ is transformed into a sum over the electron density of each atom in the molecule:

$$F(\boldsymbol{q}) \simeq \int \sum_j \rho_j^{(\text{at})}(\boldsymbol{r}-\boldsymbol{r}_j) \exp(i\boldsymbol{q}\cdot\boldsymbol{r}) \mathrm{d}^3\boldsymbol{r} = \sum_j f_j^0(q) \exp(i\boldsymbol{q}\cdot\boldsymbol{r}_j), \tag{1.6}$$

with j an index over the atoms in the biomolecule, and $\boldsymbol{r}_j$ the position vector of the j-th atom in the frame of reference of the molecule. Note that in this expression, even if the scattering factors f_j are supposed to depend only on the value of q, the whole molecular scattering factor depends on every vector $\boldsymbol{q}$ due to the phase term $\exp(i\boldsymbol{q}\cdot\boldsymbol{r}_j)$ which summarizes the contribution of each atom with respect to its position in the molecule. It is now straightforward to define the intensity scattered by

[17] DON T CROMER and JOSEPH B MANN. *Acta Crystallographica A*, **24**: 321–324, 1968.

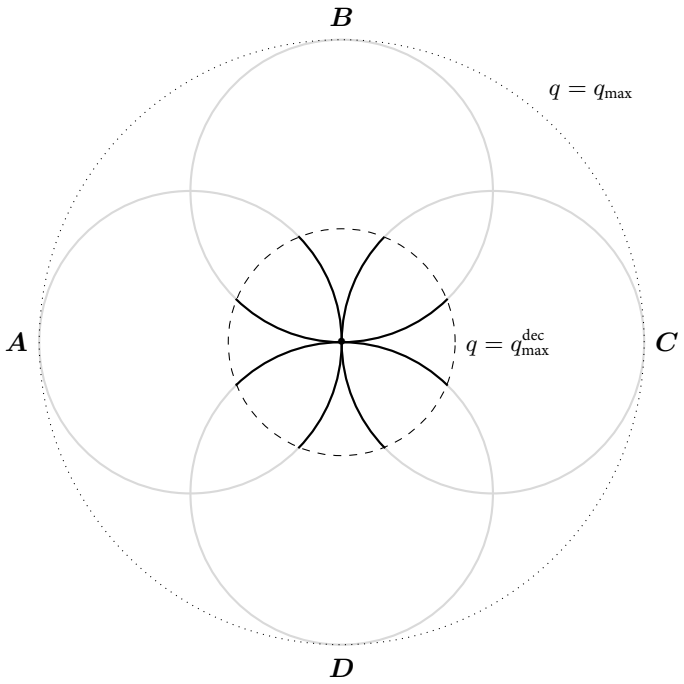

Figure 1.3 : Reconstructing the intensity function from multiple orientations. The Ewald spheres $\boldsymbol{A}$, $\boldsymbol{B}$, $\boldsymbol{C}$ and $\boldsymbol{D}$, corresponding to four different orientations of the molecule span a ball of radius $q_{\max}$. If the measurements are made on symmetric portions of the respective Ewald spheres, the ball spanned has a radius equal to $q_{\max}^{\text{dec}}$, where $q_{\max}^{\text{dec}}$ is the norm of the maximum scattering momentum on one of these Ewald sphere portions. Adapted fron Paganin.[12]

the molecule by mimicking the equation for a single atom:

$$I(\boldsymbol{q}) = |F(\boldsymbol{q})|^2 I_T = \left| \sum_j f_j^0(q) \exp(i\boldsymbol{q} \cdot \boldsymbol{r}_j) \right|^2 I_T. \tag{1.7}$$

In other words, the intensity is simply the square magnitude of the Fourier transform of the electron density $\rho^{(\text{mol})}$ according to a proportionality factor I_T. This Fourier transform relation has a fortunate symmetry property, called the Friedel symmetry. The electron density $\rho^{(\text{mol})}$ of the molecule is real; therefore its Fourier transform $F(\boldsymbol{q})$ satisfies the Hermitian symmetry $F(-\boldsymbol{q}) = \overline{F(\boldsymbol{q})}$. As a consequence, the intensity $I(\boldsymbol{q})$ satisfies the parity property, known as the Friedel symmetry property[18]

$$I(\boldsymbol{q}) = I(-\boldsymbol{q}). \tag{1.8}$$

We will show in chapter 2 that sparse representations of I can be conveniently obtained from this property.

1.2.2 Reconstructing the intensity function from multiple orientations and geometric properties of the intensity

Even though the formula (1.7) is quite general and is valid for all $\boldsymbol{q}$, one has to remember that in a given experiment, *i.e.* a particular orientation of the molecule, the only values of $\boldsymbol{q}$ available are those sampled by the Ewald sphere. Therefore a single measurement corresponds to a *slice* through the three-dimensional intensity. The acquisition of an increasing number of measurements, each corresponding to a different orientation of the molecule, eventually fills the three dimensional space so the intensity is fully determined.
The accumulation of spherical slices has a fortunate consequence on the geometry of the intensity function $I(\boldsymbol{q})$. In figure 1.3 are depicted four Ewald spheres $\boldsymbol{A}$, $\boldsymbol{B}$, $\boldsymbol{C}$ and $\boldsymbol{D}$, each corresponding to

[18] ARTHUR JAMES COCHRAN WILSON. *Elements of X-ray Crystallography*. Addison-Wesley Reading, Massachusetts, 1970.

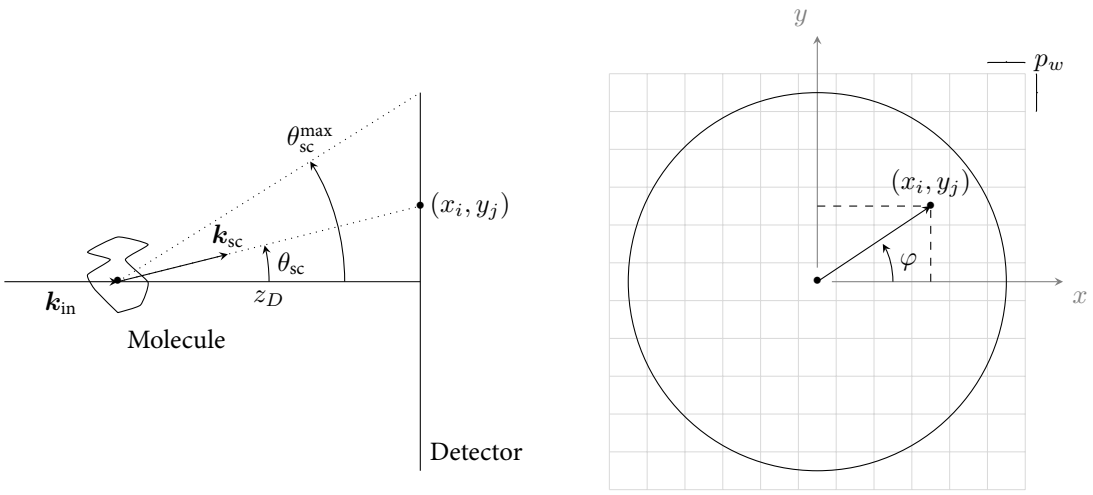

Figure 1.4 : Geometry of the experiment.

experiments where the orientation of the molecule is different from the others. The figure is drawn in two-dimensions for convenience, but the same discussion is valid for the three-dimensional case. The Ewald sphere corresponding to a new orientation of the molecule is obtained by rotation around the origin $\boldsymbol{q} = 0$ of the Ewald sphere of reference (*e.g.* $\boldsymbol{A}$). This rotation is not arbitrary, it corresponds exactly to the rotation we have applied to the molecule such that the original orientation gave the Ewald sphere $\boldsymbol{A}$. Since each Ewald sphere has diameter $4\pi/\lambda$, the accumulation of different orientations spans a ball of radius $q_{\max} = 4\pi/\lambda$. It is worth noticing that the intensity is here defined within a ball of radius $q_{\max}$ *with respect to* a certain wavelength λ; changing λ adjusts accordingly the support of the intensity function, trough the radius $q_{\max}$.
The previous discussion implicitly assumed that we were able to measure the totality of the Ewald sphere: that is one would have in practice to build a complete spherical detector ! This is obviously not possible, and experimental data is consequently collected on a portion of the Ewald sphere. The dark lines on figure 1.3 represent symmetrical portions on the Ewald spheres $\boldsymbol{A}$, $\boldsymbol{B}$, $\boldsymbol{C}$ and $\boldsymbol{D}$ respectively. The maximum norm of the scattering momentum is given by $q_{\max}^{\text{dec}}$: using the same construction as before, the accumulation of measurements spans a ball of radius $q_{\max}^{\text{dec}} < q_{\max}$.
This construction of the three-dimensional intensity $I(\boldsymbol{q})$ through a particular *tomographic* procedure, *i.e.* the acquisition of two-dimensional measurements in various orientations, has emphasized the geometrical structure of the intensity. The intensity is defined within the ball of radius $q_{\max}^{\text{dec}}$, centered at the origin of reciprocal space $\boldsymbol{q} = 0$. This motivates this work, where we believe that one could take advantage of the spherical geometry of the intensity. This work makes use of spherical coordinates as much as possible, and the remaining of this work develops tools for the analysis, representation and reconstruction of the intensity based on this motto.

Remark The reconstruction of the intensity provided here is specific to the single-particle imaging experiment, where we assume that the wavelength λ is fixed. Another way of reconstructing the intensity function is to vary the incident energy (through λ) while leaving the orientation of the object unchanged: we obtain therefore a collection of Ewald spheres, all attached to the origin $\boldsymbol{q} = 0$ but with different radii. We note that this method is irrelevant in the single-particle imaging since we are unable to control the orientation of the imaged object.

1.2.3 Intensity measured on the detector

Most experiments are performed with a planar detector, and therefore the measured intensity results from the projection of the Ewald sphere on the planar detector. Also, for simulation purposes, we need a formalism describing the intensity measured on a detector in a single particule experiment.
The first step is to obtain the expression of the scattering momentum $\boldsymbol{q}$ in terms of the pixel considered on the detector. The spherical coordinates are a natural choice for $\boldsymbol{q}$, from the discussion above. We denote by $q \in \mathbb{R}^+$ the radius, $\varphi \in [0, 2\pi]$ the azimuth angle, and $\theta \in [0, \pi]$ the colatitude angle, such that $\boldsymbol{q} = (q, \varphi, \theta)$. The detector is assumed to be planar, with square pixels of side p_w, and located at distance z_D of the molecule sample, see figure 1.4. We consider a pixel of center $(x_i, y_j) = p_w(i, j)$,

$(i,j) \in \mathbb{Z}^2$ where the reference is taken at the center of the detector. Simple geometry from figure 1.4 gives the expression of the scattering angle θ_{sc},

$$\theta_{\text{sc}} = \arctan\left(\frac{p_w\sqrt{i^2+j^2}}{z_D}\right). \tag{1.9}$$

A quick check of the domain of definition of θ_{sc} reveals that this expression is valid for any point on the detector, since the planar detector imposes $\theta_{\text{sc}} < \pi/2$. The maximum scattering angle $\theta_{\text{sc}}^{\text{max}}$ should normally be obtained on the edge of the detector; however with our spherical geometry it is more convenient to consider the angle subtended by the largest circle inscribed within the square detector. The outer regions are then simply discarded. Now, using equation (1.1) we obtain the expression of the radius q as a function of the pixel position

$$q = q_{\text{max}} \cdot \sin\left[\frac{1}{2}\arctan\left(\frac{p_w\sqrt{i^2+j^2}}{z_D}\right)\right]. \tag{1.10}$$

Whereas in general this relation is non-linear, for pixels near the center of the detector (*i.e.* small scattering angle) the relation becomes linear in the norm $\sqrt{i^2+j^2}$. The largest value of q is denoted by $q_{\text{max}}^{\text{dec}}$ and is obtained for the maximum scattering angle $\theta_{\text{sc}}^{\text{max}}$, as explained above. We now obtain the values of the azimuth angle φ an the colatitude angle θ. The angle φ is simply given by projection of the Ewald sphere on a *flattened* Ewald sphere: therefore the value of φ is obtained by

$$\varphi = \text{angle}(x_i, y_j). \tag{1.11}$$

The colatitude angle θ is determined thanks to figure 1.1. From the geometry, we have

$$\theta(q) = \frac{\pi}{2} - \theta_{\text{sc}} = \frac{\pi}{2} - \arcsin\left(\frac{q}{q_{\text{max}}}\right). \tag{1.12}$$

The notation $\theta(q)$ emphasizes the inter-dependence between θ and the norm q of the scattering momentum. This dependence is not surprising, since the measurement results from the projection of the Ewald sphere: the Ewald sphere is a two-dimensional surface, therefore only two independent parameters (here q and φ) are needed to describe it.

In the single-particle experiment each molecule is dropped in a random, unknown orientation. Equivalently it means that a random unknown rotation $\boldsymbol{R}_k$ has been applied to the original atom coordinates $\boldsymbol{r}_j$, leading to new coordinates $\boldsymbol{R}_k\boldsymbol{r}_j$. In this work we assumed that the random rotations $\boldsymbol{R}_k$ are drawn from a uniform distribution on the rotation group $SO(3)$, as it is common in the XFEL literature. More information on the generation of random uniform rotations is provided in section 3.2.2.

We give an expression for the intensity measured on the detector, for a rotation of the molecule $\boldsymbol{R}_k$. The expression below is derived from (1.7), where the measured intensity has to be proportional to the solid angle $\Delta\Omega$ subtended by the considered pixel on the detector,

$$I(\boldsymbol{q}, \boldsymbol{R}_k) = \left|\sum_j f_j(q)\exp\left(i\boldsymbol{q}\cdot(\boldsymbol{R}_k\boldsymbol{r}_j)\right)\right|^2 I_T\Delta\Omega, \quad \Delta\Omega = \frac{p_w^2}{z_D^2}\cos\theta_{\text{sc}}(q). \tag{1.13}$$

We recall that this expression is only valid for the values of $\boldsymbol{q} = (q, \varphi, \theta(q))$ as given above. The demonstration of the expression of the solid angle, alongside some technical details about the parameter values used in our simulations are given in appendix A.

There is no such thing as an ideal experimental setup, and the single particle imaging experiment makes no exception. We now discuss quickly the perturbations and sources of noise preventing from measuring $I(\boldsymbol{q}, \boldsymbol{R}_k)$ directly. In the single particle imaging experiment, the noise could have multiple origins: *e.g.* it can be due to inelastic scattering, scattering of water (water is needed such that the biomolecule is functionalized), presence of impurities or other molecules in the stream, etc. In the following of this work, we assume that these perturbations can be neglected. However in the single-particle imaging experiment one feature can not be omitted. Even with the intensities encountered at XFEL facilities, the scattering of the incident beam by the molecule is very weak; for a 500 kDa protein, one may expect only a few hundreds of photon to be recorded on the detector. Therefore a sensible model is to consider random realizations of a two-dimensional inhomogeneous Poisson

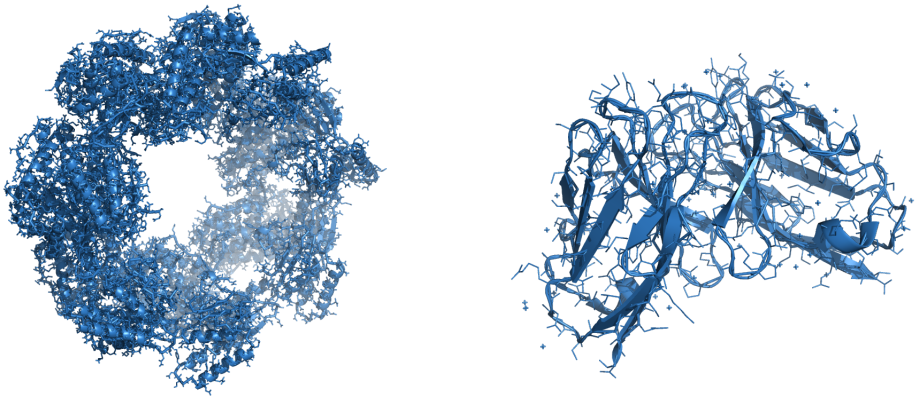

(a) GroEL molecule, 400 kDa (b) Bence-Jones protein, 24 kDa

Figure 1.5 : The two molecules used in the simulations presented in this manuscript.

process, that is each detector pixel of coordinates $\boldsymbol{q}$ in reciprocal space is a random realization of a Poisson process of parameter $I(\boldsymbol{q}, \boldsymbol{R}_k)$.
The simulations presented in this work concerns two particular biomolecules, the bacterial chaperonin GroEL and Bence-Jones protein respectively. Their molecular structure has been determined by previous measurements[19,20] and are available online in the *Protein Data Bank* (PDB), under the entries 1GRL and 1REI respectively. The GroEL is approximately 16 times larger than the Bence-Jones protein, with respective molecular masses of 400 kDa and 24 kDa. For completeness we have represented the molecular structure of these two biomolecules in figure 1.5.
Several diffraction patterns of both GroEL and the Bence-Jones protein are represented on figure 1.6 and 1.7. Each row correspond to a different orientation of the molecule. The first column depicts *continuous* diffraction patterns, that is they have been computed through equation (1.13). The second column corresponds to Poisson samples of each of these intensities; the values on the detector are integers, since they represent a photon count. The last column is also showing Poisson samples, but the underlying intensity has been rescaled to obtain a diffraction pattern with an average photon count per Shannon-Nyquist pixel close to those obtained in single-particle experiments. As expected, for the same experimental conditions the photon count is higher for the larger molecule (1GRL), and the rate of variation of the intensity with the angle of scattering is lower for the smaller molecule (1REI).
As a side note, it is interesting to point out that in the single-particle imaging experiment two sources of randomness are present. The first one is intrinsic to the measurement process, that is the Poisson realizations of the intensity, and the latter resides in the single-particle imaging procedure; since there is no possibility to control – or even measure – the orientation of the particle, we had to consider random rotations instead. The main challenges of intensity reconstruction algorithms are therefore to address the low-photon counts, as well as the lack of orientational information.

1.2.4 The oversampling requirement

Since we are only measuring intensities, that is the square modulus of the Fourier transform of the molecule, the phase information has to be recovered to obtain the electron density of the molecule. In the following, we show that the intensity has to be oversampled so that we are able to recover the phases of the electron density. We recall a discussion presented by Chapman *et al.* , in one of the original papers to demonstrate the feasibility of the single-particle experiment.[6] Similar results have been presented by Thibault *et al.* [21] for a simpler version of the actual experiment.
Let us consider a three-dimensional Cartesian grid in reciprocal space, with coordinates $\boldsymbol{u}_{i,j,k}$ and with N-equispaced samples on each axis, with step size Δu. The values of u – which are frequencies – , on a given axis, range from $(-N/2-1)\Delta u$ to $N/2\Delta u$, where N is supposed even. Let Δx represents the grid spacing in real-space, that is in the space of the molecule. From the discrete Fourier transform

[19] KERSTIN BRAIG et al. *Nature*, , 1994.
[20] OTTO EPP et al. *Biochemistry*, **14**: 4943–4952, 1975.
[21] PIERRE THIBAULT and IVAN C RANKENBURG. *American Journal of Physics*, **75**: 827–832, 2007.

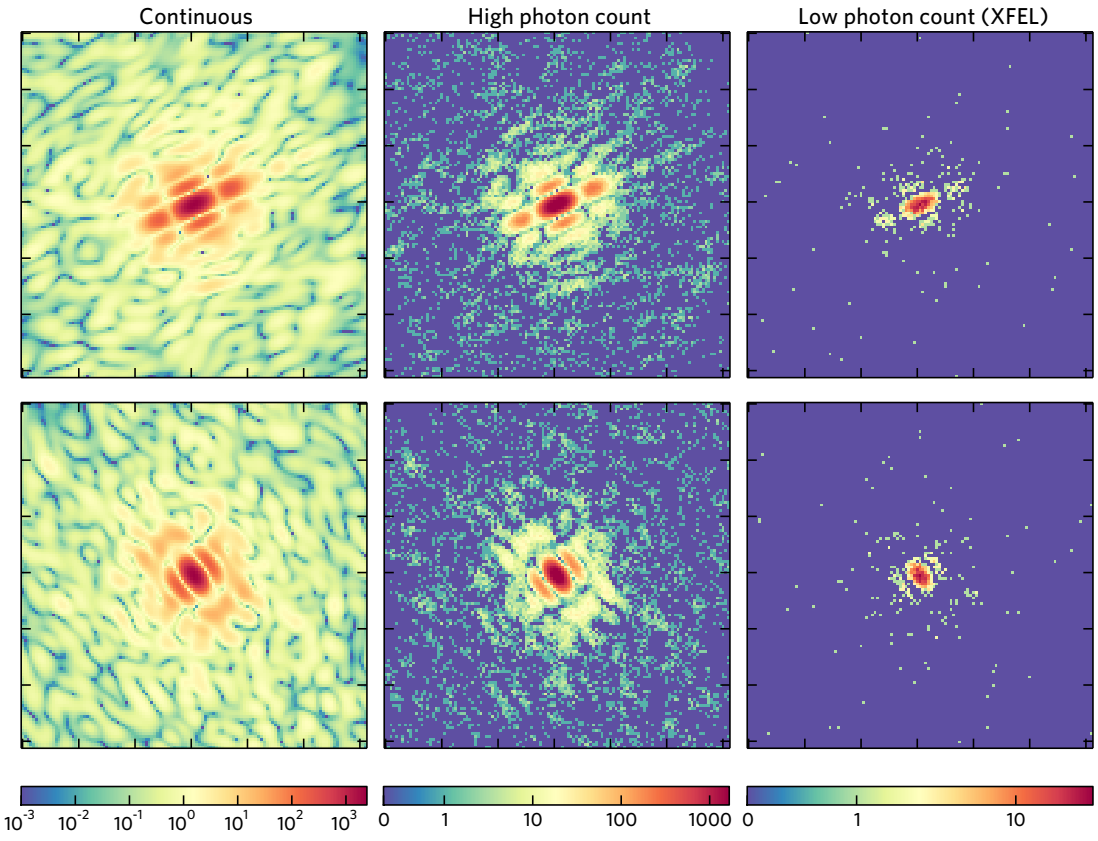

Figure 1.6 : Diffraction patterns for the 1GRL protein. Rowwise are represented two different orientations of the molecule. From left to right, the continuous intensity I, a corresponding Poisson sample with a high photon count, and a typical diffraction pattern with expected photon count at XFEL facilities. All diffraction patterns were computed on a 123× 123 pixel detector, for a wavelength $\lambda = 2$ Å. All remaining parameters are speficied in appendix A.

we have the relation

$$\Delta u \Delta x = \frac{2\pi}{N}. \tag{1.14}$$

The inverse Fourier transform of the intensity is proportional to the autocorrelation function of the electron density that would be recovered if ever the phases were known[6]

$$i(\boldsymbol{x}) = \mathcal{F}^{-1}\left[I(\boldsymbol{u})\right] \propto \rho^{(\mathrm{mol})}(\boldsymbol{x}) \otimes \rho^{(\mathrm{mol})}(\boldsymbol{x}). \tag{1.15}$$

If the molecule has a finite width D along one axis, the autocorrelation function $i(\boldsymbol{x})$ has then a finite extent of $2D$, and therefore the intensity function $I(\boldsymbol{u})$ is band-limited. Therefore, in virtue of the Shannon-Nyquist theorem, the minimum grid spacing in reciprocal space to recover all the information in $I(\boldsymbol{u})$ is given by

$$\Delta^{\mathrm{SN}} u = \frac{2\pi}{2D} = \frac{\pi}{D}, \tag{1.16}$$

where the subscript stands for Shannon-Nyquist. We introduce the oversampling ratio, σ such that $\Delta u = 2\pi/(\sigma D)$. For $\sigma = 2$, we obtain the critical Shannon-Nyquist spacing introduced above. The retrieval of the phase information is made possible through the oversampling condition.
In the first approximation of small scattering angles, the available sampling step on the detector is given by

$$\Delta q = \frac{2\pi}{\lambda} \frac{p_w}{z_D}, \tag{1.17}$$

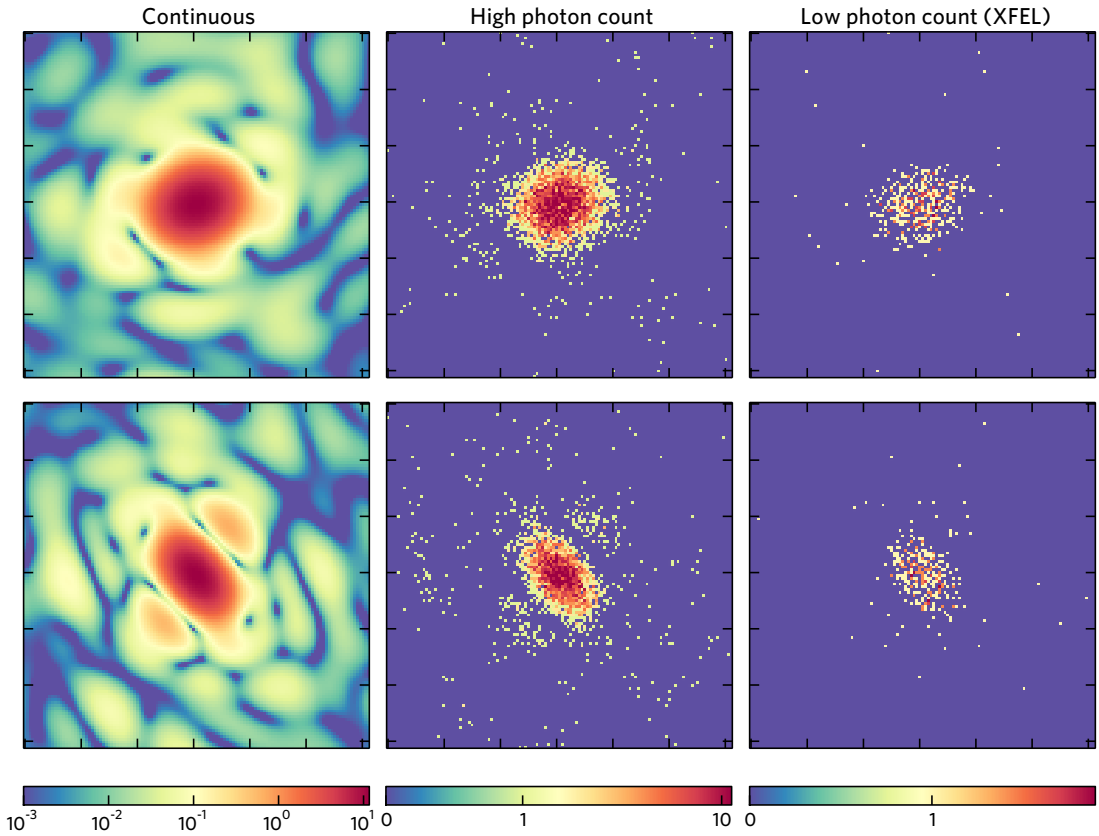

Figure 1.7 : Diffraction patterns for the Bence-Jones protein (1REI). Rowwise are represented two different orientations of the molecule. From left to right, the continuous intensity I, a corresponding Poisson sample with a high photon count, and a typical diffraction pattern with expected photon count at XFEL facilities. All diffraction patterns were computed on a 123×123 pixel detector, for a wavelength $\lambda = 2$ Å. All remaining parameters are speficied in appendix A

which is easily obtained by a Taylor series of expression (1.10). Equalizing (1.17) with the expression of Δu allows us to choose the pixel size p_w with respect to the oversampling ratio σ, the wavelength λ and the detector distance z_D and the object size D,

$$p_w = \frac{z_D \lambda}{\sigma D}. \tag{1.18}$$

Literature often refers to the Shannon-Nyquist pixel, the corresponding pixel size is given through equation (1.18) for the critical Shannon-Nyquist sampling case, that is for $\sigma = 2$.

We conclude this section by numerical examples. First, we consider the case of the molecule 1GRL, whose diffraction patterns are depicted in figure 1.6. Using the values of p_w, z_D, λ, and recalling that 1GRL has roughly a characteristic size of 150 Å[19], we obtain the following oversampling ratio

$$\sigma_{\text{1GRL}} \simeq 4. \tag{1.19}$$

In the second case, for the protein 1REI, the transverse size is approximately 54 Å, and therefore we obtain an oversampling ratio

$$\sigma_{\text{1REI}} \simeq 11. \tag{1.20}$$

The oversampling ratio is in the two cases over the critical case $\sigma = 2$, which is motivated it by the

fact that oversampling improves in practice the signal-to-noise ratio in the experiments.

Remark The principle of coherent X-ray imaging requires the detector to be placed in the far-field zone, where in that case the diffraction pattern does no longer depend on the propagation distance. For a given molecule size D, one has to check if the detector distance z_D from the sample is greater than the Fraunhofer distance z_F, given by $z_F = 2D^2/\lambda$.[6]

1.2.5 Discussion on the assumptions and XFEL case

Before stepping into reconstruction procedures, we highlight some implicit assumptions taken in this section. Precisely, we discuss the validity of our intensity model regarding the specific case of XFEL single-particle imaging.

Let us consider the scattering factor $f(\boldsymbol{q})$ defined by equation (1.3). We removed the angular dependence, and considered the isotropic scattering factor f^0 only. However, we forgot to mention that the energy $E = hc/\lambda$ of the incoming photons modifies the value of f^0. We introduce two terms, f' and f'' which only depend on the photons energy E, such that the *energy-corrected isotropic scattering factor* reads

$$f(q, E) = f^0(q) + f'(E) + if''(E). \tag{1.21}$$

XFELs provide very bright, short pulses. In our calculations, we assumed that the intensity of the incoming beam was constant and equal to I_0. This would be exact if the pulse was perfect, just like a rectangular window. However, this is hardly the case at XFEL facilities and refinement can be done using a time dependent incoming intensity $I_0(t)$. Therefore all the intensity-related quantities listed above would need to be integrated over the pulse duration.

The last remark concerns the geometry of the detector, as presented on the right side of figure 1.4. We used a rectangular detector with equal-area pixels, which is far from the real design of XFEL detectors. For reference, the design of the detector used at LCLS has a much more complex structure, showing multiple CCD detectors coupled in a spiral fashion. Pixels are of various size and shape, and gaps exist between pixel clusters. Also in XFEL experiments a few pixels in the center of the detector are removed, so that the huge amount of unscattered photons does not destroy the detector. For further information on this topic, one may want to check for instance Porro *et al.* [22] Assumptions are here made for simplicity, since the algorithm presented here is independent from the detector geometry. When needed, we will point out the small adjustments if relevant.

1.3 From diffraction patterns to molecular structure

A single-particle experiment is expected to produce up to millions of diffraction patterns, and the final goal is to obtain a high-resolution image of the structure of the biomolecule. The molecular structure determination contains two distinct procedures. First the diffraction patterns are assembled to give the three-dimensional intensity function $I(\boldsymbol{q})$, by solving the orientation problem. Second, the intensity phases are recovered trough a phase retrieval step, and the electron density (molecular structure) is obtained.

1.3.1 Intensity reconstruction strategies

Due to the low photon counts on the diffraction patterns – about 5×10^{-2} photons per Shannon-Nyquist pixel (in the high angular part) expected for a 500 kDa protein – and the subsequent poor signal-to-noise ratio, an important number of diffraction patterns have to be acquired to allow a reconstruction. Since each diffraction pattern is related to an unknown random orientation of the molecule, accurate orientation determination or compensation of the lack of orientational information is fundamental.

An intensity reconstruction algorithm needs to address the two issues above, and should ideally be computationally efficient to give intensity reconstructions in a reasonable time. Figure 1.8 shows the assembly of two-dimensional patterns to form the three-dimensional intensity function, as the number of patterns K increases. The situation depicted here corresponds to the ideal case where

[22] M Porro et al. *Nuclear Instruments and Methods in Physics Research Section A:*, **624**: 509–519, 2010.

the relative orientation of each diffraction pattern is known. The bottom row shows Poisson realization of the above diffraction patterns, and the low-photon count in the high-angular part makes the reconstruction much harder.

In order to assemble the two-dimen-sional noisy diffraction patterns into a consistent three-dimensional intensity function, numerous algorithms have been proposed to date. Early work from Huldt *et al.* [23] determined the relative orientation of two diffraction patterns by searching the *common line*, which is precisely the intersection between the associated Ewald spheres to each diffraction pattern. Locating the common could be efficiently done with continuous diffraction patterns, however due to the low number of photons in a actual diffraction pattern this is not possible. The diffraction patterns have to be classified first according to a similarity measure, which is done by cross-correlation. Averaging over the diffraction patterns in a same class increases the signal-to-noise ratio, and allows the use of the common-line algorithm. This classification step however limits unfortunately the applicability of the common line algorithm, such that this method fails with the photon counts expected in the single particle experiment.[2]

Fung *et al.* [24] proposed an algorithm based on a manifold embedding technique. This approach is based on a Generative Topographic Mapping (GTM), where each pattern is considered as a vector of the N-dimensional space of intensities, with N the number of pixels on the detector. The idea is that, since a continuous rotation of the sample implies a continuous variation of the diffraction intensities, the images obtained should span a three-dimensional manifold embedded in N-dimensional space. The manifold is generated from a large number of diffraction patterns, and averaging out the closest diffraction patterns leads to the expected smooth manifold. However, a large number of diffraction patterns may be required to obtain a sufficiently smooth manifold.[1]

The first attempt at a geometry constrained algorithm was taken by Saldin *et al.* ,[25] where the three-dimensional intensity function was expanded on the spherical harmonic basis. Their approach relies on the cross-correlation of the diffraction patterns and exploits the orthogonality of spherical harmonics to obtain a decomposition of the cross-correlation function with the spherical harmonic degree. It is interesting to note that this method has been tested experimentaly [26] on large dimers with known structure. However this method does not allow the recovery of the spherical harmonic expansion coefficients, and the correlation approach has to be coupled with a molecular replacement method to estimate the protein structure.

Loh and Elser[27] introduced the Expansion-Maximization-Compression (EMC) algorithm which relies on an Expectation-Maximization (EM) technique. The algorithm tries iteratively to maximize the likelihood of the reconstructed intensity given the set of diffraction patterns. The algorithm does not determine the actual orientation of the molecule in each pattern, it rather estimates the probability for a diffraction pattern to be associated with a certain orientation. Recently, this algorithm has proven its feasibility with the reconstruction of Mimivirus from experimental data collected at LCLS .[28] The EMC algorithm is studied in detail in this work, with the introduction of several improvements.

Recently, Walczak *et al.* [29], developed further the Bayesian approach providing two algorithms. The first one uses a seed structural model, which leads eventually to the determination of the molecular orientation for each diffraction image. The averaging of the oriented diffraction patterns lead to a reconstruction of the intensity. The second approach proposes to determine the probability that a given set of diffraction patterns fits the seed model of the molecular structure, which allows to discriminate between different structures.

Overall, it seems that Bayesian techniques have supplanted the cross-correlation methods, as they suffer from several drawbacks[30,31] given the low-number of photons expected in the single-particle experiments.

[23] G Huldt, A Szőke, and Janos Hajdu. *Journal of structural biology*, **144**: 219–227, 2003.
[24] Russell Fung et al. *Nature Physics*, **5**: 64–67, 2009.
[25] DK Saldin et al. *Journal of Physics: Condensed Matter*, **21**: 134014, 2009.
[26] Dmitri Starodub et al. *Nature communications*, **3**: 1276, 2012.
[27] Ne-Te Duane Loh and Veit Elser. *Physical Review E*, **80**: 026705, 2009.
[28] Tomas Ekeberg et al. *Physical review letters*, **114**: 098102, 2015.
[29] Michał Walczak and Helmut Grubmüller. *Physical Review E*, **90**: 022714, 2014.
[30] Veit Elser. *Ultramicroscopy*, **111**: 788–792, 2011.
[31] Veit Elser. *New Journal of Physics*, **13**: 123014, 2011.

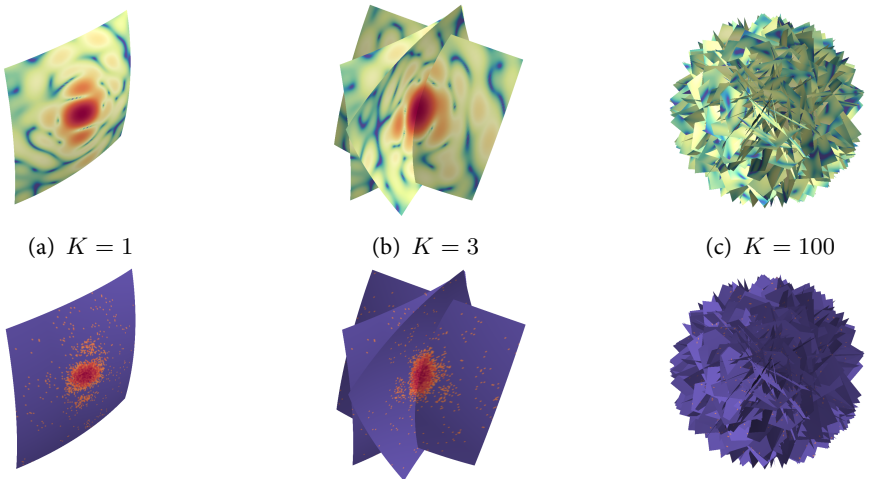

(a) $K = 1$ (b) $K = 3$ (c) $K = 100$

Figure 1.8 : 3D-intensity assembly procedure. Each diffraction pattern corresponds to a different 2D-slice (Ewald sphere) through the intensity. The accumulation of multiple diffraction patterns reconstructs the 3D intensity. Top row: continuous diffraction patterns. Bottom row: the random Poisson counterparts, with a very low-photon count in the high-angular part. Diffraction patterns were simulated from the Bence-Jones protein 1REI.

1.3.2 A brief overview of phase retrieval

As mentioned earlier, oversampling allows to recover the phase information from the recorded diffracted intensities. Phase retrieval techniques date back to the 1950s,[32] inspired by the new Shannon theorem, and have been adapted to coherent diffractive methods about a decade ago.[33–36] The study of the different phase retrieval methods is not the purpose of this work, where we concentrate on the intensity reconstruction problem. However to make this work self-contained we present the general idea behind phase retrieval techniques. The reader interested by an extensive review of the phase retrieval methods in coherent diffractive imaging may look at Marchesini[37] or more recently in the signal processing community.[38]
Quite generally, the phase problem is solved by considering that the imaged molecule is isolated, that is the electron density ρ is assumed to be equal to zero outside a so-called support constraint S,

$$\rho(\boldsymbol{r}) = 0, \quad \text{for } \boldsymbol{r} \notin S. \tag{1.22}$$

This support constraint has to be specified beforehand and is part of some *a priori* information we have about the molecule. We recall that the relationship between the three-dimensional intensity $I(\boldsymbol{q})$ and the electron density ρ is given by (1.7),

$$I(\boldsymbol{q}) \propto |\mathcal{F}\{\rho(\boldsymbol{r})\}|^2, \tag{1.23}$$

where $\mathcal{F}$ denotes the Fourier transform. Equations (1.22) and (1.23) define constraints that should fulfill the recovered electron density ρ. Phase retrieval algorithms are iterative procedures, and by re-constraining at each step the solution and an appropriate update rule, convergence to an unique solution is achieved.

1.4 Outline of this work

This work focuses on the development of an intensity reconstruction algorithm taking into account the geometry and the symmetry constraints the intensity function has to abide by.

[32] David Sayre. *Acta Crystallographica*, **5**: 843–843, 1952.
[33] J Miao, D Sayre, and HN Chapman. *JOSA A*, **15**: 1662–1669, 1998.
[34] Veit Elser. *JOSA A*, **20**: 40–55, 2003.
[35] Stefano Marchesini et al. *Physical Review B*, **68**: 140101, 2003.
[36] D Russell Luke. *Inverse Problems*, **21**: 37, 2005.
[37] Stefano Marchesini. *Review of Scientific Instruments*, **78**: 011301, 2007.
[38] Yoav Shechtman et al. *Signal Processing Magazine*, **32**: 87–109, 2015.

The geometric construction of the three-dimensional intensity function described in section 1.2 showed the importance of the spherical geometry, and suggests that it could be beneficial to propose an adequate parametrization of the intensity function.
The determination of the high-resolution intensity function of a protein is a complex problem, and algorithms require appropriate tuning of their parameters to be efficient. By estimating incrementally resolved versions of the three-dimensional intensity, we believe that some insight could be given on the choice of the different parameters. Obtaining low-resolution intensity functions has also a desirable property: to make the dream of on-demand imaging with XFELs come true, one has to develop computationally efficient algorithms. This would be beneficial since as of today computational issues are key in the development of single-particle imaging.
Our work focuses on the implementation of these constraints in the EMC algorithm developed by Loh and Elser[27].
We start by introducing in chapter 2 several mathematical tools concerning harmonic analysis on the ball, *i.e.* the solid sphere. The last section of this chapter applies these tools to the representation of three dimensional intensity functions, and we show how a sparse representation of the intensity is obtained.
The lack of orientational information in the single-particle experiment is compensated in the EMC algorithm by the introduction of deterministic sampling sets on the rotation group $SO(3)$. These sets of rotations are exploited in the heart of the algorithm to associate cross-probabilities between each diffraction pattern and each rotation of the sampling set. In chapter 1, we address the design of such sampling sets in connection with the sparse representation developed in chapter 2.
Chapter 4 presents the incorporation of the geometry and symmetry constraints in the EMC algorithm, as well as the parameter scaling regarding the requested resolution. We demonstrate trough our simulations that computational scaling is efficiently achieved, and the limits of our method.
The last chapter 5 finally concludes and draws the future work towards symmetry-constrained reconstruction algorithms.

CHAPTER 2

Harmonic analysis on the ball

2.1 Mathematical preliminaries

The previous chapter introduced the expression of the intensity scattered by a single molecule, and we saw how beneficial the use of spherical coordinates (q, φ, θ) could be. In this chapter we aim at developing harmonic analysis tools for functions defined in terms of spherical coordinates: to avoid the confusion that comes with the term "sphere", we will rather refer as harmonic analysis on the ball $\mathbb{B}^3$. We define the 3-dimensional ball $\mathbb{B}^3$ by the Cartesian product $\mathbb{B}^3 = \mathcal{R} \times \mathbb{S}^2$, where $\mathbb{S}^2$ denotes the 2-sphere. The radial interval $\mathcal{R}$ can either designate the radial line $\mathbb{R}^+$ or a finite interval $[0, Q]$, where Q is the ball radius. This distinction is needed since often orthonormal bases are build on the radial line before being restricted to a finite interval. We recall that the correspondence between spherical and Cartesian coordinates is given by $\boldsymbol{q} = (q \sin\theta\cos\varphi, q\sin\theta\sin\varphi, q\cos\theta)^T$, where $q \in \mathcal{R}$ is the radius, and where $(\varphi, \theta) \in [0, 2\pi) \times [0, \pi]$ are the angular coordinates, *i.e.* azimuth and colatitude respectively.
Following Kennedy and Sadeghi's approach,[39] we consider harmonic analysis as part of Hilbert space signal processing. To this end we introduce the space of square integrable complex-valued functions defined on $\mathcal{R}$, $\mathbb{S}^2$ and $\mathbb{B}^3$ denoted by $L^2(\mathcal{R})$, $L^2(\mathbb{S}^2)$ and $L^2(\mathbb{B}^3)$ respectively. These spaces, equipped with the following inner products

$$\langle f, g\rangle_{\mathcal{R}} = \int_{\mathcal{R}} f(q)\overline{g(q)}q^2 \mathrm{d}q, \tag{2.1}$$

$$\langle f, g\rangle_{\mathbb{S}^2} = \iint_{\mathbb{S}^2} f(\varphi,\theta)\overline{g(\varphi,\theta)}\sin\theta \mathrm{d}\theta\mathrm{d}\varphi, \tag{2.2}$$

$$\langle f, g\rangle_{\mathbb{B}^3} = \iiint_{\mathbb{B}^3} f(q,\varphi,\theta)\overline{g(q,\varphi,\theta)}q^2\sin\theta \mathrm{d}q\mathrm{d}\theta\mathrm{d}\varphi, \tag{2.3}$$

form Hilbert spaces provided that f, g are complex-valued functions on $\mathcal{R}$, $\mathbb{S}^2$ and $\mathbb{B}^3$, respectively. The previously defined inner products induce the norm $\|f\| = \langle f, f\rangle^{1/2}$ on each of these three spaces. By definition each element f of $L^2(\mathcal{R})$, $L^2(\mathbb{S}^2)$ or $L^2(\mathbb{B}^3)$ has a finite induced norm, $\|f\| < \infty$. We refer to elements of these Hilbert spaces as *signals*, following a common convention through the literature.[39,40]
This chapter is dedicated to harmonic analysis on the ball. The term "harmonic" is used as a synonym of Fourier, in that it concerns the definition of valid dual spaces, *i.e.* spatial and spectral domains. Classically the term "analysis" is put in opposition with "synthesis" in that they refer to forward and inverse Fourier transforms respectively. However we consider here the term "analysis" in a broader sense, that is it covers both forward and inverse transforms.

2.1.1 Harmonic analysis on the sphere

Orthonormal basis on $L^2(\mathbb{S}^2)$

We first focus on the space of square integrable functions defined on the sphere, that is $L^2(\mathbb{S}^2)$. The inner product on this space for two functions $f, g \in L^2(\mathbb{S}^2)$ is given by

$$\langle f, g\rangle_{\mathbb{S}^2} = \iint_{\mathbb{S}^2} f(\varphi,\theta)\overline{g(\varphi,\theta)}\ \sin\theta \mathrm{d}\theta\mathrm{d}\varphi. \tag{2.4}$$

[39] Rodney A Kennedy and Parastoo Sadeghi. *Hilbert Space Methods in Signal Processing*. Cambridge University Press, 2013.
[40] Zubair Khalid, Rodney A Kennedy, and Jason D McEwen. *Applied and Computational Harmonic Analysis*, , 2015.

The famous spherical harmonic functions, or spherical harmonics form a complete orthonormal basis of $L^2(\mathbb{S}^2)$. The spherical harmonic $Y_l^m(\varphi,\theta)$, of *degree* $l \in \{0,1,2,\ldots\}$ and *order* $m \in \{-l,-l+1,\ldots,l\}$ is defined by

$$Y_l^m(\varphi,\theta) \triangleq \sqrt{\frac{(2l+1)}{4\pi}\frac{(l-m)!}{(l+m)!}} P_l^m(\cos\theta) e^{im\varphi} = N_l^m P_l^m(\cos\theta) e^{im\varphi}, \tag{2.5}$$

where the first term N_l^m ensures that the spherical harmonics are normalized with respect to the inner product $\langle f,g\rangle_{\mathbb{S}^2}$. The second terms involve the associated Legendre polynomials P_l^m, which we now define. Let $x=\cos\theta$, so $x\in[-1,1]$. The associated Legendre polynomials for positive order $m\in\{0,1,\ldots,l\}$ are defined explicitly by

$$P_l^m(x) \triangleq \frac{(-1)^m}{2^l l!}(1-x^2)^{m/2}\frac{\mathrm{d}^{l+m}}{\mathrm{d}x^{l+m}}(x^2-1)^l, \quad m\in\{0,1,\ldots,l\}, \tag{2.6}$$

whereas the following equation defines the associated Legendre polynomials for negative values of $m\in\{-l,-l+1,\ldots,0\}$,

$$P_l^{-m}(x) = (-1)^m\frac{(l-m)!}{(l+m)!}P_l^m(x), \quad m\in\{0,1,\ldots,l\}. \tag{2.7}$$

The expressions for the associated Legendre polynomials (2.6) and (2.7) differ only by a scaling factor. The term $(-1)^m$ in (2.7) is called the *Condon-Shortley phase* factor. A particular interesting case is when $m=0$, where the associated Legendre polynomials P_l^0 reduces to Legendre polynomials P_l, thus (2.6) and (2.7) become the well-known Rodrigues' formula

$$P_l(x) \triangleq \frac{1}{2^l l!}\frac{\mathrm{d}^l}{\mathrm{d}x^l}(x^2-1)^l, \quad l\in\{0,1,\ldots\}. \tag{2.8}$$

These associated Legendre polynomials are, by the previous definitions, real-valued functions of the variable $x=\cos\theta$. Therefore the only complex valued term in the definition of spherical harmonics (2.5) is the complex exponential $e^{im\varphi}$.
The spherical harmonics form a complete orthonormal basis in $L^2(\mathbb{S}^2)$. The orthonormality property reads

$$\langle Y_l^m, Y_{l'}^{m'}\rangle_{\mathbb{S}^2} = \delta_{ll'}\delta_{mm'}, \tag{2.9}$$

where $\delta_{ll'}$ is the Kronecker delta, that is $\delta_{ll'}=1$ if $l=l'$ and $\delta_{ll'}=0$ otherwise. The completeness of spherical harmonics in $L^2(\mathbb{S}^2)$ states that any function $f\in L^2(\mathbb{S}^2)$ can be expanded in terms of spherical harmonics

$$f(\varphi,\theta) = \sum_{l=0}^{\infty}\sum_{m=-l}^{l} f_l^m Y_l^m(\varphi,\theta), \tag{2.10}$$

where the f_l^m are the coefficients obtained by projection on the corresponding spherical harmonic, *i.e.*

$$f_l^m \triangleq \langle f, Y_l^m\rangle_{\mathbb{S}^2} = \iint_{\mathbb{S}^2} f(\varphi,\theta)\overline{Y_l^m(\varphi,\theta)}\sin\theta\,\mathrm{d}\theta\mathrm{d}\varphi \tag{2.11}$$

Equations (2.10) and (2.11) define the inverse and forward spherical harmonic transforms, respectively.

Remark One can legitimately wonder where do the spherical harmonics come from. Spherical harmonics arise naturally when the eigendecomposition of the Laplacian operator ∇^2_Ω in spherical coordinates is performed, *i.e.* these are solution of the equation

$$\nabla^2_\Omega Y_l^m + l(l+1)Y_l^m = 0 \quad \text{where} \quad \nabla^2_\Omega = \frac{1}{\sin\theta}\frac{\partial}{\partial\theta}\left(\sin\theta\frac{\partial}{\partial\theta}\right) + \frac{1}{\sin^2\theta}\frac{\partial^2}{\partial\varphi^2}. \tag{2.12}$$

For a given degree l, the subspace associated with the eigenvalue $\lambda_l=-l(l+1)$ has dimension $2l+1$, with eigenvectors Y_l^m, $m\in\{-l,-l+1,\ldots,l\}$. Resolving the eigendecomposition problem leads to the analytic form (2.5) of orthonormalized spherical harmonics.

Figure 2.1 : Representation of the spherical harmonics functions for degrees $l = 0, \ldots, 6$ and corresponding positive orders m. The negative orders were ommited beacause of the symmetry property 2.13. Spherical harmonics are real-valued for $m = 0$, and complex-valued for $m \neq 0$, such that we represented in these cases the real part (top) and the imaginary part (bottom). All representations are Mollweide projections, a projection which preserves the areas and is commonly used in Physics.

Symmetries

Using the relationship (2.7) between associated Legendre polynomials of opposite order m we obtain the expression of Y_l^{-m} in terms of Y_l^m:

$$Y_l^{-m}(\varphi,\theta) = (-1)^m \overline{Y_l^m(\varphi,\theta)}, \quad l \in \{0,1,\dots\}\,,\ m \in \{0,1,\dots,l\}\,. \tag{2.13}$$

The specific application considered in this work, the single-particle experiment, leads us to consider another property: the parity property of spherical harmonics. This property reads

$$Y_l^m(\pi+\varphi,\pi-\theta) = (-1)^l Y_l^m(\varphi,\theta) \tag{2.14}$$

and will be very useful when applied to our specific application, notably when incorporating the Friedel symmetry (1.8) in our formulations.

Parseval relation and energy per degree

From a signal processing perspective, it is particularly interesting to evaluate the energy of a signal $f \in L^2(\mathbb{S}^2)$. By definition, the energy E of a signal is simply the inner product between f and itself, $E = \langle f, f\rangle_{\mathbb{S}^2} = \|f\|^2$. The Parseval relation for spherical harmonics states that the energy of f is equal to the sum of the square magnitude of each coefficient f_{lm}, that is

$$E = \int_{\mathbb{S}^2} |f(\varphi,\theta)|^2 \sin\theta \,\mathrm{d}\theta\mathrm{d}\varphi = \sum_{l=0}^{\infty}\sum_{m=-l}^{l} |f_l^m|^2. \tag{2.15}$$

The formula above is directly the result of the completeness property (2.10) and the orthonormality of the spherical harmonics (2.9). Similarly we can define the energy per degree E_l, which reads

$$E_l \triangleq \sum_{m=-l}^{l} |f_l^m|^2, \tag{2.16}$$

where $l \in \{0,1,\dots\}$. This quantity allows us to analyse the energy distribution among the degrees l, in a casual Fourier transform fashion. The degree l is indeed the frequency counterpart in spherical harmonics analysis. We shall note however that we summed in (2.16) over the values of the order m: the reason behind this definition lies in the effect of rotations on spherical harmonics coefficients. Let consider a rotation $\boldsymbol{R} \in SO(3)$ and rotates the sphere angles (φ,θ) by $\boldsymbol{R}$. We obtain a new system of coordinates, say $(\tilde{\varphi},\tilde{\theta})$ and proceed to the spherical harmonics decomposition of the same function f in this new system of coordinates. This change of frame has a well-known effect: the coefficients of this decomposition, $\tilde{f}_l^m$ are a linear composition of the previous coefficients f_l^m with the same degree l and therefore their energy $|\tilde{f}_l^m|^2$ is different. This is due to the strong connection between the spherical harmonics and the irreducible representation of the rotation group $SO(3)$, the Wigner-D matrices. Without dwelling any further in this topic, which will be addressed in chapter 4, the summation in (2.16) eliminates the rotation dependence in the energy, and one can safely obtain the same energy E_l for two different *rotated* versions of the same function f.

2.1.2 Radial harmonic analysis

We now study the case of radial square integrable functions $L^2(\mathcal{R})$, where $\mathcal{R}$ can either designate the radial line $\mathcal{R} = \mathbb{R}^+$ or the finite interval $\mathcal{R} = [0,Q]$. Quite generally, we recall that the inner product between two functions $f, g \in L^2(\mathcal{R})$ is defined by

$$\langle f, g\rangle_{\mathcal{R}} = \int_{\mathcal{R}} f(q)\overline{g(q)}q^2\mathrm{d}q. \tag{2.17}$$

In the following, we introduce two complete orthonormal bases on $L^2(\mathcal{R})$ and their subsequent forward and inverse transforms. Precisely, we start by introducing the well-known spherical Bessel functions, followed by the spherical Laguerre functions, a set of functions based on the orthogonality of exponentially weighted Laguerre polynomials on $\mathbb{R}^+$.

Spherical Bessel functions

The spherical Bessel functions of the first kind j_l and order l form a complete orthogonal basis for functions defined on the radial line $\mathcal{R} = \mathbb{R}^+$. They satisfy the orthogonality relation

$$\forall k, k' \in \mathbb{R}^+, \ \langle j_l(kq), j_l(k'q) \rangle_{\mathbb{R}^+} = \int_{\mathbb{R}^+} j_l(kq) j_l(k'q) q^2 \mathrm{d}q = \frac{\pi}{2k^2} \delta(k - k'), \tag{2.18}$$

where $\delta(k - k')$ is the Dirac delta. Note that we have omitted the conjugate operation since the spherical Bessel function j_l is real. It is important to understand that the orthogonality property holds over the values of k, rather than over the order l as one may think in the first place. The spherical Bessel function (of the first kind) of order l is given by[41]

$$j_l(kq) = \sqrt{\frac{\pi}{2q}} J_{l+1/2}(kq), \quad J_{l+1/2}(kq) = \left(\frac{kq}{2}\right)^{l+1/2} \sum_{j=0}^{\infty} \frac{\left(-\frac{1}{4}k^2q^2\right)^j}{j!\Gamma(l + 1/2 + j + 1)}, \tag{2.19}$$

where Γ denotes the Gamma function, and $J_{l+1/2}$ the Bessel function of first kind with (fractional) order $(l + 1/2)$. The orthogonality property (2.18) suggests that the basis functions should have the form $\sqrt{\pi/2} \cdot k j_l(kq)$, that is we have simply normalized the spherical Bessel function of order l. Therefore for every $l \in \{0, 1, \ldots\}$ we have the completeness property for $f \in L^2(\mathbb{R}^+)$

$$f(q) = \sqrt{\frac{2}{\pi}} \int_{\mathbb{R}^+} f_l(k) k j_l(kq) \mathrm{d}k \tag{2.20}$$

where the coefficients $f_l(k)$ are computed by projection of f on the radial basis functions, *i.e.*

$$f_l(k) = \left\langle f, \sqrt{\frac{2}{\pi}} k j_l(kq) \right\rangle_{\mathbb{R}^+} = \sqrt{\frac{2}{\pi}} \int_{\mathbb{R}^+} f(q) k j_l(kq) q^2 \mathrm{d}q. \tag{2.21}$$

Equations (2.20) and (2.21) define the inverse and forward l-th spherical Bessel transform on the radial line, respectively.[40]

Now we shall step back a little and recall the original goal. We are interested in signals defined within the ball $\mathbb{B}$ of radius Q; therefore instead of considering complete orthonormal bases on $L^2(\mathbb{R}^+)$, we shall consider orthonormal bases on $L^2([0, Q])$. Nevertheless using Stourm-Liouville theory it is possible to adapt the basis functions $\sqrt{2/\pi} k j_l(kq)$ such that they form a complete orthonormal basis on $L^2([0, Q])$. A prerequisite is to define a boundary condition at $q = Q$ such as Dirichlet or Neumann type. We think that the most sensible choice in our application is the Dirichlet boundary condition, *i.e.* $f(Q) = 0$. The equations (2.20) and (2.21) then become[42,43]

$$f(q) = \sum_{n=1}^{\infty} f_l(k_{ln}) \rho_{ln} j_l(k_{ln} q) \tag{2.22}$$

$$f_l(k_{ln}) = \int_0^Q f(q) \rho_{ln} j_l(k_{ln} q) q^2 \mathrm{d}q, \tag{2.23}$$

where $k_{ln} = z_{ln}/Q$ and z_{ln} is the n-th zero of spherical Bessel function of order l. The weights ρ_{ln} are defined by

$$\rho_{ln} = \frac{\sqrt{2} Q^{-3/2}}{|j_{l+1}(z_{ln})|}. \tag{2.24}$$

Imposing the Dirichlet boundary condition $f(Q) = 0$ leads to a fortunate consequence: now, frequency space is discretized – we replaced k by k_{ln} – and the integral in (2.20) is replaced by a discrete sum in (2.22).

[41] MILTON ABRAMOWITZ and IRENE A STEGUN. *Handbook of mathematical functions: with formulas, graphs, and mathematical tables*. 55 Courier Corporation, 1964.

[42] QING WANG, OLAF RONNEBERGER, and HANS BURKHARDT. *Pattern Analysis and Machine Intelligence, IEEE Transactions on*, **31**: 1715–1722, 2009.

[43] QING WANG, OLAF RONNEBERGER, and HANS BURKHARDT *Fourier analysis in polar and spherical coordinates* tech. rep. 2008

We finally note that the spherical Bessel functions provide a redundant description of radial functions. Indeed, let l and l', $l \neq l'$, we are able to write the decomposition of a radial function f in the bases corresponding to l and l', respectively

$$f(q) = \sum_{n=0}^{\infty} f_l(k_{ln})\rho_{ln} j_l(k_{ln} q) = \sum_{n=0}^{\infty} f_{l'}(k_{l'n})\rho_{l'n} j_{l'}(k_{l'n} q). \tag{2.25}$$

This property can be described as the *multi-completeness* of the spherical Bessel functions on the radial interval $[0, Q]$. Without loss of generality we have only considered the case $\mathcal{R} = [0, Q]$, but the same results are valid for the $\mathcal{R} = \mathbb{R}^+$ case.

Remark The connection between the order l of the spherical Bessel function j_l and the corresponding degree l of the spherical harmonics Y_l^m is a direct consequence of the relationship with the Laplacian in spherical coordinates. Indeed, the Laplacian ∇^2 is given by

$$\nabla^2 = \nabla_q^2 + \frac{1}{q^2}\nabla_\Omega^2 \quad \text{where} \quad \nabla_q^2 = \frac{1}{q^2}\frac{\partial}{\partial q}\left(q^2 \frac{\partial}{\partial q}\right), \tag{2.26}$$

and ∇_Ω^2 is defined in (2.12). The spherical Bessel functions j_l verifies

$$\nabla_q^2 \, j_l(kq) + \left(k^2 - \frac{l(l+1)}{q^2}\right) j_l(kq) = 0, \tag{2.27}$$

which is the eigenfunction problem for the Laplacian in spherical coordinates. This expression is not independent from the spherical part of the Laplacian, since the degree l of the spherical harmonics appears. As as consequence the radial part can not be fully decoupled from its angular counterpart.

Spherical Laguerre functions

The spherical Laguerre basis functions were first introduced by Leisdedt and McEwen[44] as an answer to the practical limitations of the spherical Bessel functions, which we describe later on in section 2.1.3. This basis relies on the orthogonality of Laguerre polynomials on $\mathbb{R}^+$ with exponential weight function. Reproducing some material from the original paper, we define the p-th spherical Laguerre basis function $K_p(q)$ by

$$K_p(q) \triangleq \sqrt{\frac{p!}{(p+2)!}} \frac{e^{-q/(2\tau)}}{\sqrt{\tau^3}} L_p^{(2)}\left(\frac{q}{\tau}\right), \tag{2.28}$$

where $L_p^{(2)}$ is the p-th generalized Laguerre polynomial of order two, defined as

$$L_p^{(2)}(q) \triangleq \sum_{j=0}^{p} \binom{p+2}{p-j} \frac{(-q)^j}{j!}, \tag{2.29}$$

and $\tau \in \mathbb{R}^+$ is a scale factor that allows to rescale the spherical Laguerre basis functions to any region of interest $[0, Q]$, see equation (2.54). It can be shown using the properties of the generalized Laguerre polynomials that the so-defined basis functions are indeed orthonormal under the radial inner product, such that

$$\langle K_p, K_{p'} \rangle_{\mathbb{R}^+} = \int_{\mathbb{R}^+} K_p(q) K_{p'}(q) q^2 \mathrm{d}q = \delta_{pp'} \tag{2.30}$$

where again the complex conjugation was omitted because the basis functions are real-valued. The basis functions K_p form a complete basis for functions $f \in L^2(\mathbb{R}^+)$

$$f(q) = \sum_{p=0}^{\infty} f_p K_p(q), \tag{2.31}$$

where the definition of the coefficients f_p is

$$f_p = \langle f, K_p \rangle_{\mathbb{R}^+} = \int_{\mathbb{R}^+} f(q) K_p(q) q^2 \mathrm{d}q. \tag{2.32}$$

[44] BORIS LEISTEDT and JASON D MCEWEN. *IEEE Transactions on Signal Processing*, **60**: 6257–6269, 2012.

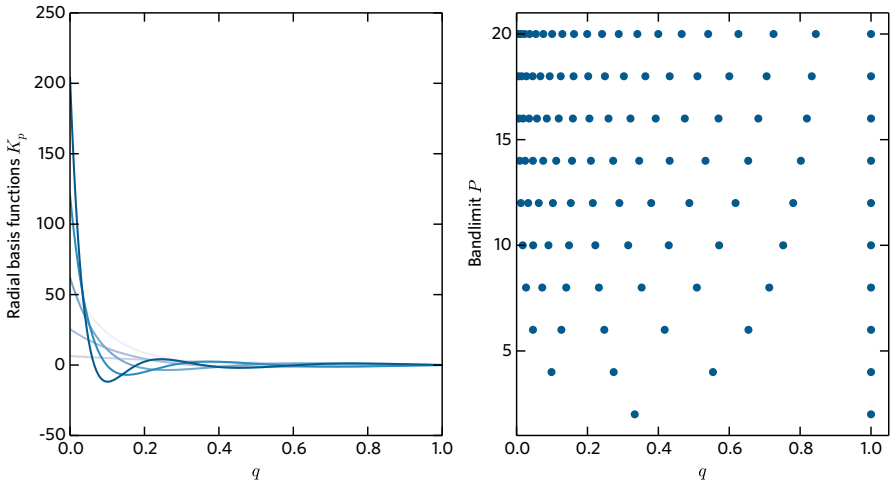

Figure 2.2 : (left) Representation of the first six spherical Laguerre functions $K_p(q)$, $p = 0, 1, \ldots, 5$ for $P = 6$ and rescaled in $[0, 1]$. (right) Radial sampling schemes on $[0, 1]$ for different values of bandlimit $P = 2, 4, \ldots 20$. Odd values of P were omitted for clarity. Sampling schemes are non-uniform, and become more concentrated towards the origin as P increases.

Equations (2.31) and (2.32) define the inverse and forward spherical Laguerre transform on the radial line, respectively.
We end this section by representing the spherical Laguerre functions in the left part of figure 2.2. We have depicted the first six spherical Laguerre functions, for a particular value of bandlimit $P = 6$ and a scaling factor τ such that the interval of interest is $[0, 1]$. The bandlimit definition is developed further on in section 2.2.1.

2.1.3 Spherical Fourier-Bessel Transform on the ball

We first consider the case $\mathcal{R} = \mathbb{R}^+$. Combining the spherical Bessel functions $j_l(kq)$ and the spherical harmonics Y_l^m, we obtain the spherical Fourier-Bessel functions $\Upsilon_l^m(k, \cdot)$

$$\Upsilon_l^m(k, \boldsymbol{q}) = \sqrt{\frac{2}{\pi}} k j_l(kq) Y_l^m(\varphi, \theta), \quad k \in \mathbb{R}^+, \tag{2.33}$$

where the order l of the spherical Bessel function matches the respective degree of the spherical harmonic Y_l^m. This basis of functions forms a complete orthonormal basis in $L^2(\mathbb{B}^3)$, by completeness and orthonormality of the spherical Bessel and spherical harmonic functions on $L^2(\mathbb{R}^+)$ and $L^2(\mathbb{S}^2)$, respectively. The orthonormality property is obtained directly

$$\left\langle \Upsilon_l^m(k, \boldsymbol{q}), \Upsilon_{l'}^{m'}(k', \boldsymbol{q}) \right\rangle_{\mathbb{B}^3} = \delta(k - k')\delta_{ll'}\delta_{mm'} \tag{2.34}$$

whereas the completeness property defines the inverse and forward Spherical Fourier-Bessel Transform (SFBT), respectively

$$f(q, \varphi, \theta) = \int_{\mathbb{R}^+} \sum_{l=0}^{\infty} \sum_{m=-l}^{l} f_l^m(k) \Upsilon_l^m(k, \boldsymbol{q}) \mathrm{d}k, \tag{2.35}$$

$$f_l^m(k) \triangleq \iiint_{\mathbb{B}^3} f(q, \varphi, \theta) \overline{\Upsilon_l^m(k, \boldsymbol{q})} q^2 \sin\theta \mathrm{d}q \mathrm{d}\varphi \mathrm{d}\theta. \tag{2.36}$$

We consider now the case $\mathcal{R} = [0, Q]$ which is directly linked with the application discussed in this work. We saw earlier that using a boundary condition at $q = Q$ we obtained a complete orthonormal basis on the radial interval $[0, Q]$. This is stated in equations (2.22) and (2.23). Proceeding exactly as above, the spherical Bessel functions $\Upsilon_l^m(k_{ln}, \cdot)$ form a complete orthonormal basis on the ball $\mathbb{B}^3 = [0, Q] \times \mathbb{S}^2$ such that

$$\Upsilon_l^m(k_{ln}, \boldsymbol{q}) = \rho_{ln} j_l(k_{ln} q) Y_l^m(\varphi, \theta), \tag{2.37}$$

where we used the notation introduced earlier. Again since the basis $\Upsilon_l^m(k_{ln}, \cdot)$ is a complete orthonormal basis on $L^2(\mathbb{B}^3)$ we are able to define the inverse and forward SFBT

$$f(q,\varphi,\theta) = \sum_{n=1}^{\infty}\sum_{l=0}^{\infty}\sum_{m=-l}^{l} f_l^m(k_{ln})\Upsilon_l^m(k_{ln},\boldsymbol{q}), \tag{2.38}$$

$$f_l^m(k_{ln}) \triangleq \iiint_{\mathbb{B}^3} f(q,\varphi,\theta)\overline{\Upsilon_l^m(k_{ln},\boldsymbol{q})}q^2\sin\theta \mathrm{d}q\mathrm{d}\varphi\mathrm{d}\theta. \tag{2.39}$$

The SFBT is a full harmonic transform, since the spherical Fourier-Bessel functions are eigenfunctions of the Laplacian in spherical coordinates. However the SFBT suffers from several implementation limitations. First, the radial and angular part are not fully decoupled, since the spherical Bessel functions have the same order l as the degree l of the corresponding spherical harmonic. This leads in practice to a redundant description of the radial part of the function f, due to the multi-completeness of the spherical Bessel functions. One shall circumvent this first drawback in order to build a discrete SFBT. This issue has been addressed recently by Lanusse *et al.*,[45] by building a discrete SFBT based on a slightly different expression of the Spherical Bessel functions. The authors make use of multiple tricks to obtain the inverse and forward discrete SFBT which will not be reproduced here.
Another drawback relies on the Dirichlet boundary condition. In regard of the intensity reconstruction problem addressed in this work, this condition might be too restrictive since it imposes the reconstruction to have $f(Q) = 0$, occurring a loss of information. Finally, the strong oscillatory nature of the spherical Bessel functions is not desirable in a estimation setting, as already pointed out in the literature.[44]
The several practical limitations of the SFBT motivate the introduction of the spherical Fourier-Laguerre transform, which circumvent the drawbacks of the SFBT mentioned above.

2.1.4 Spherical Fourier-Laguerre Transform on the ball

Replacing the spherical Bessel functions by the spherical Laguerre functions in the spherical Fourier-Bessel functions leads to the definition of a new basis on the ball, the spherical Fourier-Laguerre functions $\Psi_{p,l}^m$ which read

$$\Psi_{p,l}^m(q,\varphi,\theta) = K_p(q)Y_l^m(\varphi,\theta). \tag{2.40}$$

These functions form a complete orthonormal basis on $L^2(\mathbb{B}^3)$, from completeness and orthonormality of both spherical Laguerre functions and spherical harmonics on their respective spaces. We define the inverse spherical Fourier-Laguerre transform as

$$f(q,\theta,\varphi) = \sum_{p=0}^{\infty}\sum_{l=0}^{\infty}\sum_{m=-l}^{l} f_{p,l}^m\Psi_{p,l}^m(q,\varphi,\theta), \tag{2.41}$$

where the coefficients $f_{p,l}^m$ are obtained by the forward spherical Fourier-Laguerre transforms.

$$f_{p,l}^m = \int_{\mathbb{B}^3} f(q,\theta,\varphi)\overline{\Psi_{p,l}^m(q,\varphi,\theta)}\, q^2\sin\theta \mathrm{d}q\mathrm{d}\theta\mathrm{d}\varphi. \tag{2.42}$$

We have the Parseval relation from the orthonormality of the Spherical Fourier-Laguerre functions in $L^2(\mathbb{B}^3)$

$$E = \iiint_{\mathbb{B}^3} |f(q,\varphi,\theta)|^2 q^2\sin\theta \mathrm{d}q\mathrm{d}\theta\mathrm{d}\varphi = \sum_{p=0}^{\infty}\sum_{l=0}^{\infty}\sum_{m=-l}^{l}|f_{p,l}^m|^2 \triangleq \sum_{p=0}^{\infty}\sum_{l=0}^{\infty} E_{p,l}, \tag{2.43}$$

where we have introduced the rotation-invariant energy per order, $E_{p,l} = \sum_{m=-l}^{l}|f_{p,l}^m|^2$. This quantity allows us to analyse the energy distribution among both radial and angular coefficients.

[45] FRANÇOIS LANUSSE, ANAIS RASSAT, and J-L STARCK. *Astronomy & Astrophysics*, **540**: A92, 2012.

2.2 Numerical considerations

The definition of the Spherical Fourier-Laguerre Transform (SFLT) has been given, however the expression of the forward SFLT requires the evaluation of multiple integrals, which is numerically not desirable. This section therefore focuses on the numerical implementation of the discrete SFLT.
A first assumption is key in the following. We consider bandlimited signals on the ball. First, we define $\mathcal{H}_L^P$ as the space of (P, L)-band-limited functions on the ball,

$$\mathcal{H}_L^P \triangleq \left\{ f \in L^2(\mathbb{B}^2) \mid f_{p,l}^m = 0,\ \forall p \geq P \text{ or } \forall l \geq L \right\}. \tag{2.44}$$

It is somewhat interesting to introduce two other subspaces, the space $\mathcal{H}_L$ of L-bandlimited signals on the sphere,

$$\mathcal{H}_L \triangleq \left\{ f \in L^2(\mathbb{S}^2) \mid f_l^m = 0,\ \forall l \geq L \right\}, \tag{2.45}$$

and $\mathcal{H}^P$ the space of P-bandlimited signals on the radial line,

$$\mathcal{H}^P \triangleq \left\{ f \in L^2(\mathbb{R}^+) \mid f_p = 0,\ \forall p \geq P \right\}. \tag{2.46}$$

2.2.1 Implementation of discrete transforms

In this section we focus on the numerical implementation of the forward and inverse SFLT. Let us recall that for $f \in \mathcal{H}_L^P$, the forward and inverse SFLT are given by

$$f_{p,l}^m = \int_{\mathbb{B}^3} f(q,\varphi,\theta)\overline{\Psi_{p,l}^m(q,\theta,\varphi)}\, q^2 \sin\theta \mathrm{d}q\mathrm{d}\theta\mathrm{d}\varphi \qquad \text{(forward SFLT)}, \tag{2.47}$$

$$f(q,\varphi,\theta) = \sum_{p=0}^{P-1}\sum_{l=0}^{L-1}\sum_{m=-l}^{l} f_{p,l}^m \Psi_{p,l}^m(q,\varphi,\theta) \qquad \text{(inverse SFLT)}, \tag{2.48}$$

where the sum in (2.48) has been restricted to $P-1$ and $L-1$ since f is a (P, L)-bandlimited function on the ball. We recall that the basis functions are given by the product $\Psi_{p,l}^m(q,\varphi,\theta) = K_p(q)Y_l^m(\varphi,\theta)$ and therefore it is possible to rewrite the expression of the forward SFLT (2.47) as

$$f_{p,l}^m = \int_{\mathbb{R}^+}\left[\iint_{\mathbb{S}^2} f(q,\theta,\varphi)\overline{Y_l^m(\varphi,\theta)}\, \sin\theta \mathrm{d}\theta\mathrm{d}\varphi\right] K_p(q)\, q^2 \mathrm{d}q, \tag{2.49}$$

which illustrates that the forward SFLT can be obtained by applying successively the forward Spherical Harmonic Transform (SHT) followed by the forward Spherical Laguerre Transform (SLT). The inverse SFLT is obtained in the reverse order, applying first the inverse SLT and then the inverse SHT. We note that one can also do the reverse operations, that is starting by the forward SLT and then the forward SHT, since these transforms commute. However a choice has to be made, and in this work we adopt the first structure proposed, which is depicted in figure 2.4. In the next sections we construct an efficient forward and inverse SFLT by building efficient forward and inverse SHT and SLT.

Discrete spherical Laguerre transform

Let us consider a P bandlimited radial function, namely $f \in \mathcal{H}^P$. The coefficients f_p of its decomposition in the spherical Laguerre basis, *i.e.* the forward SLT, are given by

$$f_p = \int_{\mathbb{R}^+} f(q)K_p(q)q^2\mathrm{d}q, \tag{2.50}$$

whereas the inverse SLT is given by the reconstruction formula

$$f(q) = \sum_{p=0}^{P-1} f_p K_p(q). \tag{2.51}$$

From a numerical perspective, the integral expression (2.50) is not practical. However, as shown in Leistedt and McEwen[44] the Laguerre-Gauss quadrature can be applied and therefore the coefficients f_p can be evaluated by

$$f_p = \sum_{i=0}^{P-1} w_i f(q_i)K_p(q_i) \tag{2.52}$$

where $q_i = \tau q_i^*$ and q_i^* is the i-th root of $L_P^{(2)}$, and the weights w_i are such that

$$w_i = \tau^3 \frac{(P+2) q_i^* \exp(q_i^*)}{(P+1)[L_{P+1}^{(2)}(q_i^*)]^2} \tag{2.53}$$

This quadrature formula is fortunate since it allows us to give an expression for the scale factor τ. Since we want to rescale the sampling roots q_i^* so that we can capture all the information available in a given interval of interest $[0, Q]$, a natural choice for τ is

$$\tau = \frac{Q}{q_{P-1}^*}. \tag{2.54}$$

Putting all things together, to perform the forward SLT one only needs to evaluate the function f at P points, namely $q_0, q_1, \dots q_{P-1}$ defined in terms of the roots of the Laguerre polynomial $L_P^{(2)}$. This radial sampling scheme is depicted on the right side of the figure 2.2 for different values of the bandlimit P and a scaling factor τ such that all the roots are in the interval $[0, 1]$. As P increases, the roots tend to concentrate more around 0. The forward and inverse SLT can be conveniently performed through matrix manipulation, as suggested by equations (2.52) and (2.51). The forward SLT reads

$$\begin{pmatrix} f_0 \\ f_1 \\ \vdots \\ f_{P-1} \end{pmatrix} = \boldsymbol{T}^D \begin{pmatrix} f(q_0) \\ f(q_1) \\ \vdots \\ f(q_{P-1}) \end{pmatrix}, \quad \left(\boldsymbol{T}^D\right)_{ij} = w_j K_i(q_j). \tag{2.55}$$

Similarly we get the following matrix form for the inverse SLT:

$$\begin{pmatrix} f(q_0) \\ f(q_1) \\ \vdots \\ f(q_{P-1}) \end{pmatrix} = \boldsymbol{T}^I \begin{pmatrix} f_0 \\ f_1 \\ \vdots \\ f_{P-1} \end{pmatrix}, \quad \left(\boldsymbol{T}^I\right)_{ij} = K_j(q_i). \tag{2.56}$$

Discrete spherical Harmonic transform

Let us consider $f \in \mathcal{H}_L$. The forward and inverse SHT are given by

$$f_l^m = \int_{\mathbb{S}^2} f(\theta, \varphi) \overline{Y_l^m(\theta, \varphi)} \sin\theta \mathrm{d}\theta \mathrm{d}\varphi \qquad \text{(forward SHT)}, \tag{2.57}$$

$$f(\varphi, \theta) = \sum_{l=0}^{L-1} \sum_{m=-l}^{l} f_l^m Y_l^m(\varphi, \theta) \qquad \text{(inverse SHT)}. \tag{2.58}$$

The computation of the forward SHT requires the evaluation of an integral over the 2-sphere $\mathbb{S}^2$. The evaluation of such integrals can be done by conveniently sampling the 2-sphere, *i.e.* distributing nodes on the surface on the sphere in order to obtain a quadrature formula.

The development of sampling schemes on the sphere has been strongly motivated by the analysis of the Cosmic Microwave Background (CMB) sky maps where the dataset lies on the celestial sphere. Since CMB measurements lead to potentially multimillion pixels maps,[46–50] these pixelization schemes shall exhibit efficiency, exactness and speed qualities. However today these are slightly conflicting requirements.[51] Numerous pixelizations have been already proposed, each with different properties. Healy *et al.* [52] proposed a angular rectangular grid which allows an exact quadrature, but the distribution of pixels favors the poles and is far from efficient. Recent results from

[46] JACQUES DELABROUILLE et al. , **493**: 835–857, 2009.
[47] A KOGUT et al. *The Astrophysical Journal Supplement Series*, **148**: 161, 2003.
[48] PAR ADE et al. *Astronomy & Astrophysics*, **571**: A16, 2014.
[49] JM LAMARRE et al. *New Astronomy Reviews*, **47**: 1017–1024, 2003.
[50] DAVID N SPERGEL et al. *The Astrophysical Journal Supplement Series*, **148**: 175, 2003.
[51] J.-F. CARDOSO. *IEEE Signal Processing Magazine*, **27**: 55–66, 2010.
[52] JAMES R DRISCOLL and DENNIS M HEALY. *Advances in applied mathematics*, **15**: 202–250, 1994.

McEwen and Wiaux[53] seem promising, but have not been widely used yet. Other sampling schemes include GLESP[54] and IGLOO[55], based respectively on Gauss-Legendre quadrature and the icosahedron. However none of these sampling schemes has become the standard for CMB studies whereas the Hierarchical Equal Area isoLatitude Pixelization (HEALPix) scheme[56] has been widely used since its introduction. It is worth noticing that an extensive package of HEALPix routines is available in C and Python, allowing easier algorithmic integration.

The HEALPix scheme has been designed for high performance, fast and accurate computation of spherical harmonics on the sphere. The sphere is tessellated into curvilinear equal-area pixels, where the pixel centers are distributed on lines of constant latitude allowing faster computation of spherical harmonic functions due to the separation of angular variables in the spherical harmonics. The HEALPix sampling scheme is hierarchical and provides different levels of resolution trough a parameter called n_{side}. The number of pixels n_{pix} at resolution n_{side} is given by

$$n_{\text{pix}} = 12 \times n_{\text{side}}^2, \tag{2.59}$$

where the parameter n_{side} is a power of 2. The explanation is the following. The base grid of the HEALPix sampling scheme is constituted of 12 pixels, and the next resolution sampling scheme is obtained by dividing each pixel into four equal area pixels on the sphere, and so forth.

The main drawback with HEALPix is that it lacks exact weights for an exact quadrature formula. However since the sphere is tessellated into equal-area pixels, one may obtain a very accurate quadrature formula with equal weights $4\pi/n_{\text{pix}}$. Given the set of HEALPix pixels $\{(\varphi_i, \theta_i)\}_{i=0,\dots,n_{\text{pix}}-1}$, the forward SHT is obtained by the quadrature formula

$$f_l^m = \frac{4\pi}{n_{\text{pix}}} \sum_{i=0}^{n_{\text{pix}}-1} f(\varphi_i, \theta_i) \overline{Y_l^m(\varphi_i, \theta_i)}. \tag{2.60}$$

We have not yet explained the choice of the resolution parameter n_{side} with respect to the bandlimit L, this will be done in section 2.2.2 where we introduce a sampling theorem.

Discrete spherical Fourier-Laguerre Transform

Let us consider a function $f \in \mathcal{H}_L^P$, and such that all the information of interest is concentrated in the ball of radius Q. First given P and a scaling parameter τ, we define a radial sampling scheme $q_0, q_1, \dots, q_{P-1} \in [0, Q]$. At each radial value we associate a spherical shell containing n_{pix} pixels. We finally obtain a grid $\mathcal{G}$ in $\mathbb{R}^3$ defined by

$$\mathcal{G} \triangleq \left\{ (q_s, \varphi_i, \theta_i) \mid s = 0, 1, \dots, P-1, i = 0, 1, \dots, n_{\text{pix}} - 1 \right\}, \tag{2.61}$$

which consists in $P \cdot n_{\text{pix}}$ points. With the discrete SLT and the discrete SHT formalism at hand, we are now able to build the discrete SFLT on this grid according to the implementation depicted on figure 2.4. In order to perfom the forward SFLT, the SHT is first performed on each concentric shell of radius q_s. This operation is conveniently performed thanks to the comprehensive set of routines available in the HEALPix package. We obtain the set of coefficients $f_l^m(q_s)$. Therefore for every l, m we can compute P coefficients, namely $f_{p,l}^m$ where $p = 0, \cdots P-1$. The forward SLT can be easily implemented in matrix form by a simple modification of (2.55)

$$\begin{pmatrix} f_{0,l}^m \\ f_{1,l}^m \\ \vdots \\ f_{P-1,l}^m \end{pmatrix} = \boldsymbol{T}^D \begin{pmatrix} f_l^m(q_0) \\ f_l^m(q_1) \\ \vdots \\ f_l^m(q_{P-1}) \end{pmatrix}, \quad \left(\boldsymbol{T}^D\right)_{ij} = w_j K_i(q_j). \tag{2.62}$$

[53] JASON D MCEWEN and YVES WIAUX. *Signal Processing, IEEE Transactions on*, **59**: 5876–5887, 2011.
[54] AG DOROSHKEVICH et al. *International Journal of Modern Physics D*, **14**: 275–290, 2005.
[55] ROBERT G CRITTENDEN and NEIL G TUROK. *arXiv preprint astro-ph/9806374*, , 1998.
[56] KRZYSZTOF M GORSKI et al. *The Astrophysical Journal*, **622**: 759, 2005.

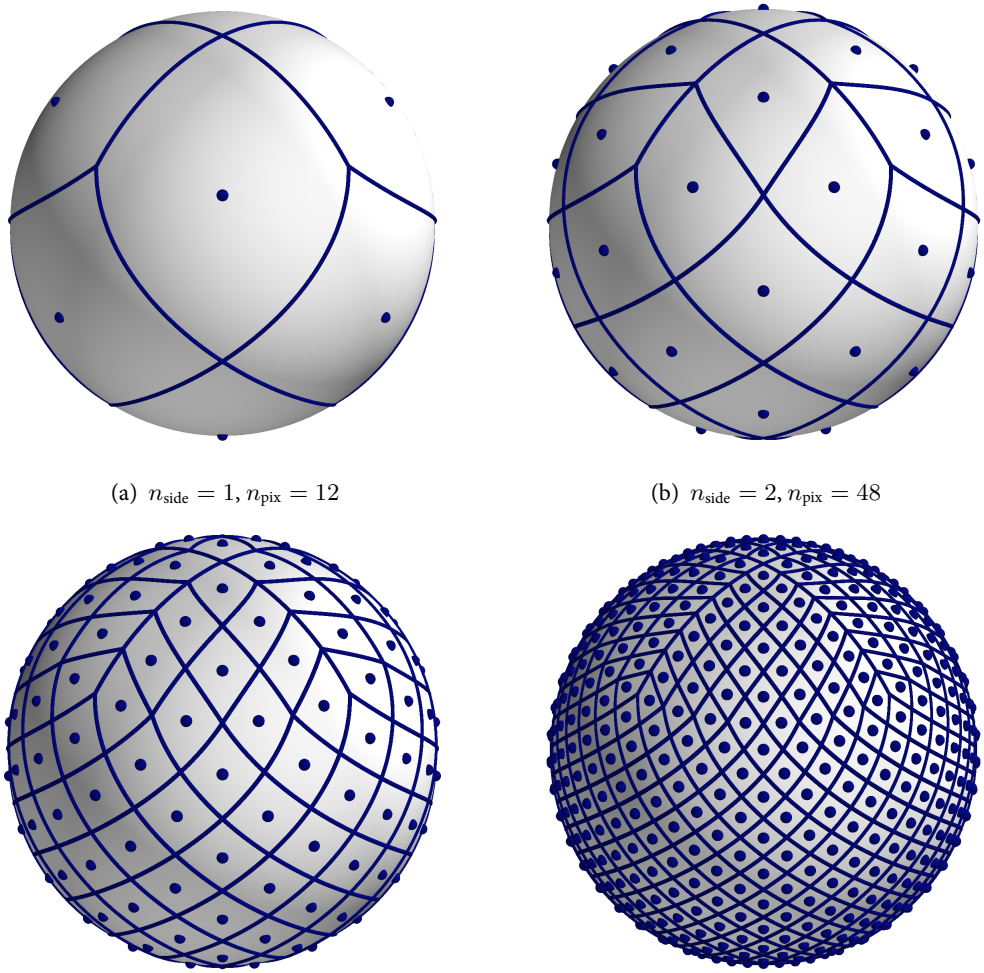

(a) $n_{\text{side}} = 1, n_{\text{pix}} = 12$ (b) $n_{\text{side}} = 2, n_{\text{pix}} = 48$

(c) $n_{\text{side}} = 4, n_{\text{pix}} = 192$ (d) $n_{\text{side}} = 8, n_{\text{pix}} = 768$

Figure 2.3 : HEALPix grids for the four first resolution parameters $n_{\text{side}} = 1, 2, 4, 8$, leading to number of pixels $n_{\text{pix}} = 12, 48, 192, 768$.

$$f(\boldsymbol{q}) \xrightarrow{\text{SHT}} f_l^m(\boldsymbol{q}_s) \xrightarrow{\text{SLT}} f_{p,l}^m \qquad \text{(forward)}$$

$$f_{p,l}^m \xrightarrow[\text{inv. SLT}]{} f_l^m(\boldsymbol{q}_s) \xrightarrow[\text{inv. SHT}]{} f(\boldsymbol{q}) \qquad \text{(inverse)}$$

Figure 2.4 : Implementation of the Spherical Fourier-Laguerre Transform (SFLT). The forward transform is computed by performing succesively the Spherical Harmonic Transform (SHT) and the Spherical Laguerre Tranform (SLT). The inverse transform is similarly computed in the reverse order.

Similarly, for the inverse SFLT, we get the following matrix form for the inverse SLT:

$$\begin{pmatrix} f_l^m(q_0) \\ f_l^m(q_1) \\ \vdots \\ f_l^m(q_{P-1}) \end{pmatrix} = \boldsymbol{T}^I \begin{pmatrix} f_{0,l}^m \\ f_{1,l}^m \\ \vdots \\ f_{P-1,l}^m \end{pmatrix}, \quad \left(\boldsymbol{T}^I\right)_{ij} = K_j(q_i), \tag{2.63}$$

whereas the inverse SHT is again conveniently performed trough HEALPix package routines.

2.2.2 A sampling theorem on the ball

We omitted in the last section a key point: given $f \in \mathcal{H}_L^P$, how do we have to choose the number of points of the grid $\mathcal{G}$ so that all of the information content is captured? First, it is clear that if the radial

part of f is P-bandlimited, then according to the quadrature rule for the discrete SLT, only P points suffice. However for the angular part, since the HEALPix scheme lacks an exact quadrature rule, no theoretical result is available to the best of our knowledge.
This question is addressed heuristically in the HEALPix reference manual.[57] In the uncorrected quadrature mode, that is the weights are uniform and equal to $4\pi/n_{\text{pix}}$, a very good accuracy is obtained if the condition

$$L \leq 2n_{\text{side}} + 1, \tag{2.64}$$

is satisfied. It is nevertheless possible to go beyond this condition for $2n_{\text{side}} + 1 < L \leq 3n_{\text{side}}$ if the SHT routines are performed in iterative mode, which reduces efficiently the quadrature errors. Another approach has been taken by Gräf *et al.* [58] where they compute numerically by an optimization procedure the weights for the HEALPix scheme. Their numerical results suggest that the number of pixels n_{pix} on a spherical shell has to obey $n_{\text{pix}} \geq 4/3 \cdot L^2$ so that integrals of spherical harmonics up to degree $L-1$ are obtained with a very good accuracy. Some straightforward calculation leads to the the following HEALPix sampling theorem on the sphere

$$3n_{\text{side}} \geq L, \tag{2.65}$$

which is the same as the heuristic condition given by the HEALPix manual for the iterative mode.
In this work we will only consider the uncorrected quadrature mode, that is our sampling theorem on the sphere takes the form (2.64). This choice is motivated by simplifying motivations, however it is straightforward to adapt the rest of this work to other sampling theorems on the sphere. From the SLT quadrature and the sampling theorem on the sphere (2.64), we obtain the following sampling theorem on the ball

$$P \cdot n_{\text{pix}} \geq P \cdot 3(L-1)^2. \tag{2.66}$$

2.2.3 Radial and angular resolutions

We briefly give the expression of the radial and angular resolutions provided by the spherical Fourier-Laguerre functions. Let us consider $f \in \mathcal{H}_L^P$. The radial and angular resolutions are fixed independently from each other, because of the decoupling of the radial and angular part in the basis functions $\Psi_{p,l}^m$. The angular resolution $\Delta\Omega$ of f is given by the resolution of the spherical harmonic of highest degree, that is Y_{L-1}^m, where the order has been left arbitrary since it does not intervene in the resolution. The angular resolution of f is given by

$$\Delta\Omega = \frac{\pi}{L-1}, \tag{2.67}$$

which is well-defined for $L > 1$. In the case $L = 1$, the notion of angular resolution is meaningless since the function f has a constant angular part and therefore is independent from the angular coordinates.
The radial resolution Δq is more complicated to obtain, since the spherical Laguerre functions are not strictly speaking harmonic (they are not solution of the radial Laplacian). We propose our own resolution criterion by considering the sampling scheme associated with the SLT for P-bandlimited radial functions. We estimate that the radial resolution is given by the smallest distance between two nodes of this sampling $q_0, q_1, \ldots, q_{P-1}$,

$$\Delta q = \min_{0 \leq i < j < P} |q_i - q_j|, \tag{2.68}$$

where again the expression is well-defined for $P > 1$, the case $P = 1$ being meaningless. One may conjecture that the radial resolution is equal to the distance between the two first nodes, as suggests the behavior of the sampling nodes as P increases.
Equations (2.67) and (2.68) will be useful in the next section, when we will link the upper-bound on the resolution parameters P and L with the intrinsic resolution provided by the experimental measurements.

[57] NASA *anafast reference and documentation* June 2010 URL: http://healpix.jpl.nasa.gov/html/facilitiesnode7.htm

[58] MANUEL GRÄF, STEFAN KUNIS, and DANIEL POTTS. *Applied and Computational Harmonic Analysis*, **27**: 124–132, 2009.

2.3 Spherical Fourier-Laguerre decomposition of the scattered intensity

This work is dedicated to the reconstruction of the three-dimensional intensity scattered by a single molecule in a XFEL experiment. We have seen in the previous chapter that this intensity function is conveniently described in spherical coordinates $\boldsymbol{q} = (q, \varphi, \theta)$ and therefore we have introduced a tool to perform harmonic analysis on the ball, the SFLT. The remaining of this chapter shows that a sparse representation of the scattered intensity is obtained thanks to the SFLT formalism, and we provide several numerical results supporting our approach.
As seen in section 1.2.1, the scattered intensity I is equal to the square-magnitude of the scattering factor F :

$$I(\boldsymbol{q}) = |F(\boldsymbol{q})|^2 I_0 \qquad \text{where } F(\boldsymbol{q}) = \sum_{j \text{ atoms}} f_j(q) \exp\left(i \boldsymbol{R}_j \cdot \boldsymbol{q}\right), \tag{2.69}$$

where f_j is the scattering factor of the atom j and $\boldsymbol{R}_j$ is the position vector of this atom in the frame of reference of the molecule. As a direct consequence, the intensity function is a real-valued, non-negative function on the ball $\mathbb{B}^3$. Another fundamental feature property of the scattering intensity function is the Friedel-symmetry as introduced in 1.8, which reads

$$I(-\boldsymbol{q}) = I(\boldsymbol{q}), \tag{2.70}$$

and will lead to a fortunate consequence on the Fourier-Laguerre coefficients, as discussed in the next section.

2.3.1 The scattered intensity as a bandlimited function

The first key property of the scattered intensity function is its bandlimited aspect. We have seen in section 1.2.1 the Fourier-type connection between the electron density of the molecule $\rho^{(\text{mol})}$ and the scattered intensity function I. The fact that the imaged molecule has a finite extent D, yields to an bandlimited intensity function.
Using some approximations, it is possible to give a qualitative estimation of the radial and angular bandlimits, namely, namely P^{lim} and L^{lim}, in terms of the size of the biomolecule. More precisely, we assume that the molecule is roughly spherical, with a diameter equal to the extent D.
The angular bandlimit L^{lim} is easily obtained using the resolution of the spherical harmonics given by (2.67) and the definition of the Shannon-Nyquist spacing (1.16). Considering that we are measuring intensities on a detector, the angular resolution $\Delta\Omega$ is the most critical in the last shell available, which has radius $q_{\text{max}}^{\text{dec}}$. Thus the Shannon-Nyquist angular resolution $\Delta^{\text{SN}}\Omega$ is given by

$$\Delta^{\text{SN}}\Omega = \frac{\Delta^{\text{SN}} q}{q_{\text{max}}^{\text{dec}}} = \frac{\pi}{L^{\text{lim}} - 1}, \tag{2.71}$$

which yields to the expression of the bandlimit L^{lim},

$$L^{\text{lim}} = q_{\text{max}}^{\text{dec}} D - 1. \tag{2.72}$$

However this bandlimit is far too high for the other shells, and it is more interesting to introduce a bandlimit per shell L_s^{lim} such that

$$L_s^{\text{lim}} = q_s D - 1, \tag{2.73}$$

where q_s is the radius of the shell considered.
The radial case is a bit more complex, since the radial transform is not harmonic in the Fourier sense, and because the radial nodes are not equispaced. As a consequence it is not straightforward to establish a criterion based on the Shannon-Nyquist sampling rate, and further investigation is needed. A first guess would lead to the following definition of P^{lim}

$$\Delta^{\text{SN}} q = \min_{0 \le i < j < P^{\text{lim}}} |q_i - q_j|, \tag{2.74}$$

but because the nodes q_i of the radial sampling go quickly to the origin, the condition (2.74) seems rather unrealistic. The lack of direct definition of the radial bandlimit P^{lim} will be however partially compensated by the definition of another criterion, based on the geometry of the detector, as explained in the remark of section 4.3.1.

2.3.2 Properties of the spherical Fourier-Laguerre coefficients

The SFLT formalism was developed in the broader setting of complex-valued functions: therefore the spherical Fourier-Laguerre coefficients should reasonably reflect the different properties of the intensity scattering function. The decomposition of the intensity function I onto the spherical Fourier-Laguerre basis, *i.e.* the inverse SFLT, writes

$$I(q,\varphi,\theta) = \sum_{m=-l}^{l} I_{p,l}^{m} K_p(q) Y_l^m(\varphi,\theta), \tag{2.75}$$

where $I_{p,l}^m$ are the spherical Fourier-Laguerre coefficients as defined by (2.32). Note that the sums in (2.75) are not truncated even though the scattered intensity is in practice bandlimited due either to the finite size of the molecule or the bandlimited measurements on the detector.

The intensity is real-valued, therefore its complex conjugate and itself are equal. Using the symmetry property (2.13) of spherical harmonics, we obtain after some simple manipulations of (2.75)

$$I_{p,l}^{-m} = (-1)^m \overline{I_{p,l}^m}, \quad l \in \{0,1,\ldots\}\,,\ m \in \{0,1,\ldots,l\}\,, \tag{2.76}$$

that is the coefficients $I_{p,l}^{-m}$ are the complex conjugate of the coefficients $I_{p,l}^m$ for m positive. By formula (2.76) the spherical Fourier-Laguerre coefficients $I_{p,l}^0$ are strictly real-valued.

We consider now the Friedel rule (2.70). Again, some tedious manipulations of (2.75) lead to another feature in the coefficient domain. We write

$$\begin{aligned} I(-\boldsymbol{q}) &= \sum_{p=0}^{P^{\lim}-1} \sum_{l=0}^{L^{\lim}-1} \sum_{m=-l}^{l} I_{p,l}^m K_p(q) Y_l^m(\pi-\theta,\pi+\varphi) && (2.77)\\ &= \sum_{p=0}^{P^{\lim}-1} \sum_{l=0}^{L^{\lim}-1} \sum_{m=-l}^{l} I_{p,l}^m K_p(q) (-1)^l Y_l^m(\theta,\varphi) && (2.78)\\ &= \sum_{p=0}^{P^{\lim}-1} \sum_{l=0}^{L^{\lim}-1} \sum_{m=-l}^{l} I_{p,l}^m K_p(q) Y_l^m(\theta,\varphi) && (2.79)\\ &= I(\boldsymbol{q}) && (2.80) \end{aligned}$$

where we took advantage from the parity property of spherical harmonics (2.14). The Friedel symmetry is then satisfied if and only if the spherical harmonics coefficients $I_{p,l}^m(q)$ are equal to zero for every odd degree l, that is

$$I(\boldsymbol{q}) = I(-\boldsymbol{q}) \iff \forall l \in \{1,3,\ldots\}\,, \quad I_{p,l}^m = 0. \tag{2.81}$$

In the general case of an arbitrary complex-valued function $f \in \mathcal{H}_L^P$, the number of independent, non-zero spherical Fourier-Laguerre coefficients is equal to PL^2. The angular part gives indeed $\sum_{l=0}^{L-1}(2l+1) = L^2$ coefficients, leading to the result. The intensity function I however is not arbitrary and exhibits several properties as seen above. The number of independent, non-zero coefficients is now $P^{\lim}(L^{\lim}+1)^2/4$. Moreover the angular bandwidth $L^{\lim}$ has to be an odd number in virtue of the Friedel symmetry (2.81).

We mention eventually another property which relies on a reformulation of the decomposition (2.75). Using the the radial and angular part separation, (2.75) reads

$$I(q,\varphi,\theta) = \sum_{l=0}^{L^{\lim}-1} \sum_{m=-l}^{l} I_l^m(q) Y_l^m(\varphi,\theta), \quad I_l^m(q) \triangleq \sum_{p=0}^{P^{\lim}-1} I_{p,l}^m K_p(q), \tag{2.82}$$

where we have introduced the *radial spherical harmonic coefficients* $I_l^m(q)$. This intensity decomposition was proposed by Starodub *et al.*,[26] but the radial spherical harmonic coefficients were left arbitrary and no radial basis was introduced. In the following, we determine the value of the radial spherical harmonics coefficients at the origin $q = 0$, that is $I_l^m(0)$. We start by expanding the

Property	Consequence
Real-valued	$I_{p,l}^{-m} = (-1)^m \overline{I_{p,l}^m}$
Friedel symmetry	$I_{p,l}^m = 0$ for l odd
Value at $q = 0$	$I_0^0(0) \neq 0,\ I_l^m(0) = 0\ \forall m,\ \forall l > 0$

Table 2.1 : Summary of the properties of the spherical Fourier-Laguerre coefficients for an intensity function.

scattering factor $F(\boldsymbol{q})$ into spherical harmonics thanks to the *plane-wave expansion* formula[59]

$$e^{i\boldsymbol{q}\cdot\boldsymbol{R}} = 4\pi \sum_{l=0}^{\infty} \sum_{m=-l}^{l} i^l j_l(qR) Y_l^m(\theta,\varphi) \overline{Y_l^m(\theta_R,\varphi_R)} \tag{2.83}$$

where (R, θ_R, φ_R) denotes the spherical coordinates of the vector $\boldsymbol{R}$. We obtain finally the spherical harmonic expansion of the scattering factor $F(\boldsymbol{q})$

$$F(\boldsymbol{q}) = \sum_{l=0}^{\infty} \sum_{m=-l}^{l} F_l^m(q) Y_l^m(\theta,\varphi), \quad F_l^m(q) = 4\pi i^l \sum_{j \text{ atoms}} f_j(q) j_l(qR_j) Y_l^m(\theta_{R_j},\varphi_{R_j}). \tag{2.84}$$

It is now possible to give an expression of the corresponding $I_l^m(q)$ coefficients in terms of $F_l^m(q)$ coefficients, by using the result[60]:

$$\begin{aligned} I_l^m(q) = & \sum_{l_1,l_2,m_1,m_2} (-1)^{m_1-m} \sqrt{\frac{(2l_1+1)(2l_2+1)(2l+1)}{4\pi}} \\ & \times \begin{pmatrix} l_1 & l_2 & l \\ 0 & 0 & 0 \end{pmatrix} \begin{pmatrix} l_1 & l_2 & l \\ m_1 & -m_2 & -m \end{pmatrix} F_{l_1}^{m_1}(q) \overline{F_{l_2}^{m_2}(q)} \end{aligned} \tag{2.85}$$

where the matrices denotes the Wigner-3j coefficients, widely used in quantum mechanics in the description of the interaction between two angular momenta.[61] Let us recall an important property of the spherical Bessel functions j_l. For all degrees $l > 0$, the value at the origin is zero, whereas for $l = 0$ the value at the origin is equal to 1. As a consequence, the values of $F_l^m(0)$ are equal to zero, except for the first coefficient F_0^0. Moreover, this result can be extended to the values at the origin of the spherical harmonics coefficients $I_l^m(q)$ by looking at the expression (2.85) and using the non-zeros properties of the Wigner-3j coefficients.[61] It is interesting also to note that the first property outlined in this section is a straightforward consequence of equation (2.85).

2.3.3 Sub-resolved versions of the intensity

One of the goals of the work presented in this manuscript is the estimation of sub-resolved versions of the true scattering intensity, that is (P, L)-bandlimited intensity functions such that $L \leq L^{\text{lim}}$ and $P \leq P^{\text{lim}}$. We have considered the Bence-Jones protein 1REI for our simulations, and a detector such that the maximum scattering vector is $q_{\text{max}}^{\text{dec}} = 0.63$ Å^{-1}, that is in the SFLT formalism the radius of the ball is $Q = q_{\text{max}}^{\text{dec}}$. We recall that this protein has an approximate size of $D = 54$ Å, and therefore the angular bandlimit L^{lim} is given by

$$L^{\text{lim}} = q_{\text{max}}^{\text{dec}} D - 1 \simeq 33. \tag{2.86}$$

According to the sampling theorem on the sphere (2.64), the bandlimit L^{lim} fixes the resolution parameter of the regular grid to $n_{\text{side}} = 16$.
We computed then the theoretical scattered intensity by this protein on two different grids $\mathcal{G}$, for $P = 7$ and $P = 21$ and $n_{\text{side}} = 16$. For the two cases $P = 7$ and $P = 21$, we computed the spherical Fourier-Laguerre coefficients $I_{p,l}^m$ by the forward SFLT, and investigated the accuracy of the reconstruction obtained by the inverse SFLT. This reconstruction is a filtered – sub-resolved –

[59] Roger G Newton. *Scattering theory of waves and particles*. Springer Science & Business Media, 2013.
[60] Heinrich B. Stuhrmann. *Acta Crystallographica A*, **26**: 297–306, 1970.
[61] Michael Tinkham. *Group theory and quantum mechanics*. Courier Corporation, 2003.

version of the true scattering intensity. These results are depicted in figure 2.5, where the angular bandwidth L takes the values $L = 1, 5, 17, 33$. The case $L = 1$ can be seen as the *spherical average* of the function I since only the terms $I^0_{p,0}$ are non-zero. As one would expect, the accuracy of the reconstruction increases as L grows, until becoming almost indistinguishable from the computed theoretical intensity in the case $L = 33 = L^{\text{lim}}$, which validates our estimation of the maximum bandlimit L^{lim}. Also we note that the case $P = 21$ provides a better radial resolution than the case $P = 7$, as expected.

2.3.4 Parseval decomposition of the intensity

We conclude this section by the analysis of the energy decomposition of the intensity. The Parseval relation (2.43) allows the separation of the total energy of the intensity into the energy per coefficients, that is

$$E = \sum_{p=0}^{\infty} \sum_{l=0}^{\infty} E_{p,l}, \tag{2.87}$$

where the order m has been simplified through the rotation invariant quantity $E_{p,l} = \sum_{m=-l}^{l} E^m_{p,l}$. The analysis of the energy distribution among the coefficients is of great importance, since it gives some insight about which coefficients contribute effectively to the total energy. In X-ray imaging, angular details increase as the scattering magnitude q, as the radius grows. A natural question then is, how does the energy distribution behaves as q increases? This can be also investigated through the SFLT formalism. The grid $\mathcal{G}$ which is used to perform the SFLT is made of concentric spherical shells of radius $q_0, q_1, \ldots, q_P$. Given an intensity function I, the forward SFLT gives $I^m_{p,l}$, but we have access to the radial spherical coefficients at $q_0, q_1, \ldots, q_P$ through the inverse SLT:

$$f^m_l(q_s) = \sum_{p=0}^{P-1} f^m_{p,l} K_p(q_s). \tag{2.88}$$

We then introduce another quantity $E_l(q_s)$, the energy per degree l and spherical shell s which is defined formally by

$$E_l(q_s) \triangleq \sum_{m=-l}^{l} |f^m_l(q_s)|^2. \tag{2.89}$$

In the following we illustrate the two approaches with two molecules of different size and mass, 1REI which is a relatively small protein of mass 24 kDa, and GroEL (pdb entry: 1GRL) which has a mass of 400 kDa. The results are summarized on figure (2.6).
We computed the scattered intensity for the two molecules with the same parameters as above in the case $P = 21$. The spherical Fourier-Laguerre coefficients were computed through the forward SFLT with $L = 33$ and energies are obtained as mentioned above. The left side of figure (2.6) corresponds to the energy distribution $E_{p,l}$, whereas the right side depicts the energy distribution per shell $E_l(q_p)$. Each distribution is represented in relative energy contribution scale, where the total energy was approximated by the sum of all energies.
We start to describe the energy distribution per shell, which is perhaps the more intuitive. In both 1REI and 1GRL cases, most of the energy is concentrated in the inner shells, and only few l degrees are relevant. As we move to the outer shells, the distribution becomes more widespread, as expected. Also we notice that the energy distribution of the bigger molecule, 1GRL, vanishes faster as the shell radius increases. This is a consequence of the fact that our computations were done for the same detector, that is $q^{\text{dec}}_{\text{max}}$ is fixed. However, the significant shells have a slightly larger spherical harmonic distribution in the 1GRL case, exactly as predicted by the expression of L^{lim}_s.
The analysis of the energy distribution of the spherical Fourier-Laguerre is less convenient, since there is *a priori* no intuition that can be developed. Nevertheless, it gives us some information about how the energy distribution in the radial spherical Laguerre behaves.

(a) $P = 7, L = 1$ (b) $P = 7, L = 5$ (c) $P = 7, L = 17$ (d) $P = 7, L = 33$ (e) $P = 7$, computed

(f) $P = 21, L = 1$ (g) $P = 21, L = 5$ (h) $P = 21, L = 17$ (i) $P = 21, L = 33$ (j) $P = 21$, computed

Figure 2.5 : Sub-resolved versions of the computed scattered intensity of protein 1REI. Intensity functions I defined within the ball of radius $Q = q_{\text{max}}^{\text{dec}}$ are represented trough three cut planes $x, y, z = 0$ and a spherical shell in the center, where this spherical shell belongs to the grid $\mathcal{G}$. The values on the cut planes are obtained by linear interpolation of the values available on the grid $\mathcal{G}$. The spherical shells depicted are: the shell $p = 3$ for $P = 7$, corresponding to a scattering vector of magnitude $q = 0.19$ Å^{-1} whereas for $P = 21$ the shell is $p = 10$ such that $q = 0.14$ Å^{-1}. (a)–(d) $P = 7$ is fixed, and sub-resolved versions are depicted for $L = 1, 5, 17, 33$. The case $L = 33$ corresponds to the maximum angular bandwidth for parameter $n_{\text{side}} = 16$. (e) Computed intensity for $n_{\text{side}} = 16$ and $P = 7$. (f)–(i) same as above with $P = 21$. (g) Computed intensity for $n_{\text{side}} = 16$ and $P = 21$.

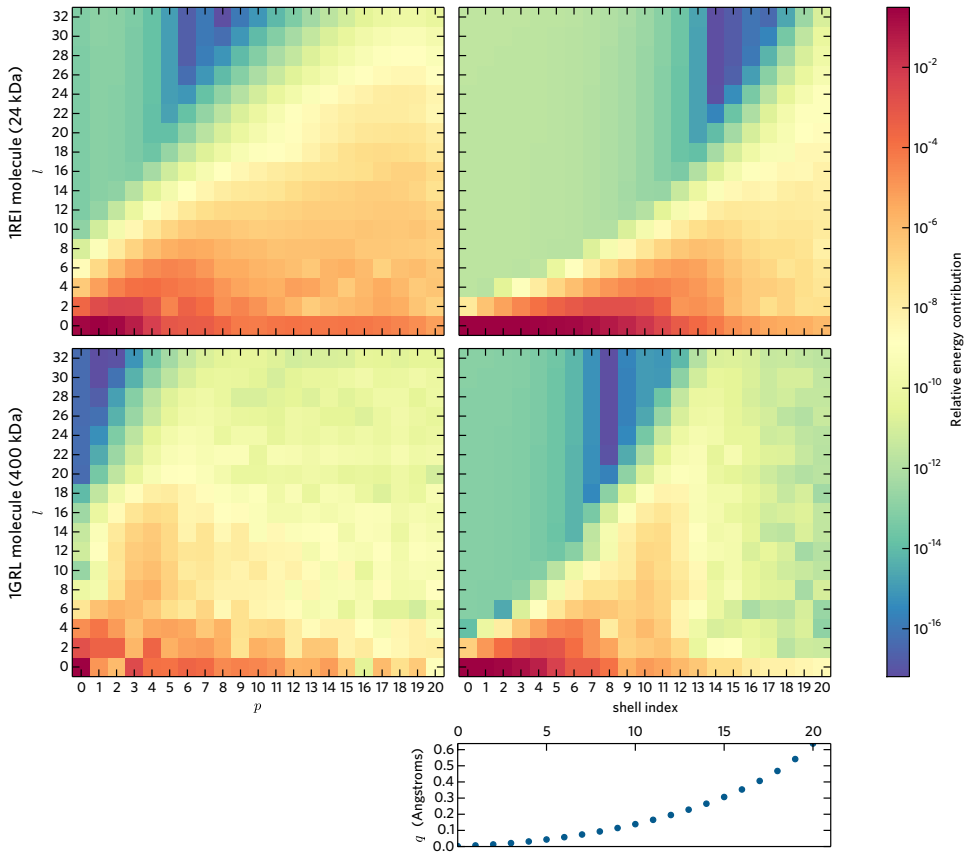

Figure 2.6 : Energy distributions of 1REI and 1GRL. Intensities were computed on a grid with parameters $P = 21$ and $n_{\text{side}} = 16$. The SFLT decomposition was computed up to $L = 33$, in accordance with the sampling theorem on the ball. The left column represents the energy distribution of the spherical Fourier-Laguerre coefficients for 1REI and 1GRL. The right column depicts the energy per degree and shell index for the two molecules. The correspondence between the shell index and the shell radius q has been added for convenience.

CHAPTER 3

Sampling schemes and quadrature formulae on $SO(3)$

This chapter is dedicated to the study of uniform sampling schemes on the rotation group $SO(3)$, as well as the construction of quadrature rules on $SO(3)$. Main results presented here are extracted from the literature, with some extensions developed in regard of the single-particle imaging reconstruction problem. We start by recalling in section3.1 different properties of the rotation group, and move to the construction of uniform sampling schemes in section 3.2. The final section 3.3 addresses the problem of quadrature rules on $SO(3)$ which will motivate some part of our approach in the upcoming chapters.

3.1 Special orthogonal group $SO(3)$

3.1.1 Definition

The special orthogonal group in three dimensions $SO(3)$ denotes the set of all the 3×3 real matrices $\boldsymbol{R}$ which satisfy

$$\boldsymbol{R}\boldsymbol{R}^T = \boldsymbol{I}_3 \quad \text{and} \quad \det \boldsymbol{R} = 1, \tag{3.1}$$

where $\boldsymbol{R}^T$ is the transpose of the matrix $\boldsymbol{R}$, $\det \boldsymbol{R}$ its determinant and $\boldsymbol{I}_3$ the 3×3 identity matrix.[62] The set $SO(3)$ is a group under the matrix product: first, it is straightforward that $\boldsymbol{I}_3$ belongs to $SO(3)$. Then for $\boldsymbol{R}_1, \boldsymbol{R}_2 \in SO(3)$ we have $\boldsymbol{R}_1\boldsymbol{R}_2 \in SO(3)$ and $\boldsymbol{R}^{-1} = \boldsymbol{R}^T \in SO(3)$ for every matrix $\boldsymbol{R} \in SO(3)$.
The first condition in (3.1) states that the columns of $\boldsymbol{R}$ form an orthonormal basis in $\mathbb{R}^3$. The second condition states that this orthonormal basis is direct, or in other words positively oriented. The Riemannian (or angular) distance between two rotations $\boldsymbol{R}_1, \boldsymbol{R}_2 \in SO(3)$ is given by

$$d_{SO(3)}(\boldsymbol{R}_1, \boldsymbol{R}_2) = \arccos\left\{\frac{1}{2}\left[\mathrm{Tr}\left(\boldsymbol{R}_2\boldsymbol{R}_1^T\right) - 1\right]\right\}. \tag{3.2}$$

This metric is invariant by left and right translation, that is $d_{SO(3)}(\boldsymbol{R}_1, \boldsymbol{R}_2) = d_{SO(3)}(\boldsymbol{R}_2, \boldsymbol{R}_1)$.

3.1.2 Parametrizations of $SO(3)$

Every rotation $\boldsymbol{R} \in SO(3)$ can be represented as an orthonormal basis made of its columns $(\boldsymbol{r}_0, \boldsymbol{r}_1, \boldsymbol{r}_2)$. Besides this representation there exists numerous ways of describing, *i.e.* parametrizing, rotations in $\mathbb{R}^3$. In this section we give a few parametric representations that we shall use in this work.

Axis-angle and quaternion parametrization

A parametrization of great importance is the axis-angle parametrization. Any rotation $\boldsymbol{R}$ can be uniquely specified by its axis $\boldsymbol{n} = (n_x, n_y, n_z)^T$ and the angle of rotation θ around its axis $\boldsymbol{n}$, that is we write $\boldsymbol{R} = \boldsymbol{R}(\boldsymbol{n}, \theta)$. Since $\boldsymbol{n}$ is chosen to be of unit length, there are only three independent parameters describing the rotation as one would expect. The matrix $\boldsymbol{R}(\boldsymbol{n}, \theta)$ is written explicitly as[62]

[62] Simon L Altmann. *Rotations, quaternions, and double groups*. Courier Corporation, 2005.

$$\boldsymbol{R}(\boldsymbol{n},\theta) = \exp(\theta \boldsymbol{Z}) \quad \text{where} \quad \boldsymbol{Z} = \begin{pmatrix} 0 & -n_z & n_y \\ n_z & 0 & -n_x \\ -n_y & n_x & 0 \end{pmatrix}, \tag{3.3}$$

where $\exp(\cdot)$ denotes the matrix exponential.
The axis-angle parametrization of $SO(3)$ is intimately related to the quaternion representation of the rotation group. Each rotation $\boldsymbol{R}$ corresponds to two unit quaternions q and $-q$ which are diametrically opposed on the surface of the 3-sphere $\mathbb{S}^3$. The unit quaternion q relates to the axis-angle parametrization via the equation

$$q = \cos\theta + \sin\theta\,(n_x \mathtt{i} + n_y \mathtt{j} + n_z \mathtt{k}), \quad \boldsymbol{n} = (n_x, n_y, n_z)^T. \tag{3.4}$$

Here, $\mathtt{i}, \mathtt{j}, \mathtt{k}$ denote the usual pure quaternions, see for instance Conway.[63] The correspondence between the quaternion representation and the matrix form of a rotation $\boldsymbol{R}$ is given by the Euler-Rodrigues formula

$$\boldsymbol{R} = \begin{pmatrix} q_0^2+q_1^2-q_2^2-q_3^2 & 2(q_1q_2-q_0q_3) & 2(q_1q_3-q_0q_2) \\ 2(q_1q_2+q_0q_3) & q_0^2+q_2^2-q_1^2-q_3^2 & 2(q_2q_3-q_0q_1) \\ 2(q_1q_3+q_0q_2) & (q_2q_3+q_0q_1) & q_0^2+q_3^2-q_1^2-q_2^2 \end{pmatrix}, \quad q = (q_0,q_1,q_2,q_3) \tag{3.5}$$

where it is indeed clear that the quaternions q and $-q$ give the same rotation matrix $\boldsymbol{R}$.

Euler angles

Euler angles have been used widely as a parametrization of $SO(3)$. Each element $\boldsymbol{R} \in SO(3)$ is parametrized by a set of three angles, namely $(\varphi,\theta,\psi) \in [0,2\pi)\times[0,\pi]\times[0,2\pi)$ where each element corresponds to the angle of rotation around the canonical axes x, y or z. Let $\boldsymbol{e}_x = (1,0,0)^T$, $\boldsymbol{e}_y = (0,1,0)^T$, $\boldsymbol{e}_z = (0,0,1)^T$ the corresponding unit vectors. Rotations $\boldsymbol{R}(\boldsymbol{e}_x,\theta)$, $\boldsymbol{R}(\boldsymbol{e}_y,\theta)$, $\boldsymbol{R}(\boldsymbol{e}_z,\theta)$ read explicitly

$$\boldsymbol{R}(\boldsymbol{e}_x,\theta) = \begin{pmatrix} 1 & 0 & 0 \\ 0 & \cos\theta & -\sin\theta \\ 0 & \sin\theta & \cos\theta \end{pmatrix} \tag{3.6}$$

$$\boldsymbol{R}(\boldsymbol{e}_y,\theta) = \begin{pmatrix} \cos\theta & 0 & \sin\theta \\ 0 & 1 & 0 \\ -\sin\theta & 0 & \cos\theta \end{pmatrix} \tag{3.7}$$

$$\boldsymbol{R}(\boldsymbol{e}_z,\theta) = \begin{pmatrix} \cos\theta & -\sin\theta & 0 \\ \sin\theta & \cos\theta & 0 \\ 0 & 0 & 1 \end{pmatrix} \tag{3.8}$$

Twelve different conventions exist to represent a rotation, each convention corresponding to a different ordering of rotation around the canonical axes, *e.g.* xyz or xyx. In this work we will only use the zyz convention, as it is of standard use in quantum mechanics.[61] Following this convention, any rotation $\boldsymbol{R}_{\text{Euler}}(\varphi,\theta,\psi) \in SO(3)$ can be written as the product $\boldsymbol{R}(\boldsymbol{e}_z,\varphi)\boldsymbol{R}(\boldsymbol{e}_y,\theta)\boldsymbol{R}(\boldsymbol{e}_z,\psi)$. We remark that even φ is written first, it is actually the third angle applied while ψ is the first one applied. Using the matrix forms (3.7) and (3.8), we obtain the matrix $\boldsymbol{R}_{\text{Euler}}(\varphi,\theta,\psi)$

$$\boldsymbol{R}_{\text{Euler}}(\varphi,\theta,\psi) = \begin{pmatrix} \cos\varphi\cos\theta\cos\psi - \sin\varphi\sin\psi & -\cos\varphi\cos\theta\sin\psi - \sin\varphi\cos\psi & \cos\varphi\sin\theta \\ \sin\varphi\cos\theta\cos\psi + \cos\varphi\sin\psi & -\sin\varphi\cos\theta\sin\psi + \cos\varphi\cos\psi & \sin\varphi\sin\theta \\ -\sin\theta\cos\psi & \sin\theta\sin\psi & \cos\theta \end{pmatrix}. \tag{3.9}$$

The relative simplicity of use of the Euler angles shall not hide the several issues that may arise with its usage. For instance, one shall note that this parametrization does not lead to a continuous mapping in the parameter space, which may lead to a phenomena known as *gimbal lock*, where the normally 3-dimensional parameter space becomes 2-dimensional.

[63] JOHN H CONWAY and DEREK A SMITH. *AMC*, **10**: 12, 2003.

Orthogonal axes parametrization

We now introduce another parametrization, which is based on recent work from Mitchell[64] and Gräf and Potts.[65] We start by recalling that a rotation $\boldsymbol{R} \in SO(3)$ is represented by the set of its orthonormal columns $\boldsymbol{R} = (\boldsymbol{r}_0, \boldsymbol{r}_1, \boldsymbol{r}_2)$. The idea of the orthogonal axes parametrization relies in the decomposition of a rotation $\boldsymbol{R}$ in two successive rotations $\boldsymbol{R}_1$ and $\boldsymbol{R}_2$, such that their respective axes are orthogonal. Before moving to the definition of theses two rotations, we proceed to an heuristic construction of a rotation matrix $\boldsymbol{R} = (\boldsymbol{r}_0, \boldsymbol{r}_1, \boldsymbol{r}_2)$. First we start by choosing $\boldsymbol{r}_2 \in \mathbb{S}^2$. Then we can choose $\boldsymbol{r}_0$ in the tangent circle at vector $\boldsymbol{r}_2$, *i.e.* $\boldsymbol{r}_0 \in \mathbb{S}^2_{\perp \boldsymbol{r}_2} \cong \mathbb{S}^1$. The last element $\boldsymbol{r}_1$ is obtained by orthogonality constraints,

$$\boldsymbol{r}_1 = \boldsymbol{r}_2 \times \boldsymbol{r}_0 \tag{3.10}$$

This parametrization leads to the decomposition of the rotation $\boldsymbol{R}$ in two successive rotations $\boldsymbol{R}_1$ and $\boldsymbol{R}_2$. The first rotation moves the north pole $\boldsymbol{e}_z$ to $\boldsymbol{r}_2$ along the shortest geodesic: posing $\boldsymbol{r}_2 = (\sin\theta\cos\varphi, \sin\theta\sin\varphi, \cos\theta)^T$, *i.e.* $\boldsymbol{r}_2$ is given by its spherical coordinates (θ, φ), the rotation $\boldsymbol{R}_1$ writes

$$\boldsymbol{R}_1 = \boldsymbol{R}(\boldsymbol{r}_2^{\perp}, \theta), \quad \boldsymbol{r}_2^{\perp} = (-\sin\varphi, \cos\varphi, 0)^T. \tag{3.11}$$

Indeed in order to rotate $\boldsymbol{e}_z$ to $\boldsymbol{r}_2$ along the shortest geodesic, we perform a rotation of angle θ with the axis perpendicular to $\boldsymbol{r}_2$, *i.e.* $\boldsymbol{r}_2^{\perp} = (-\sin\varphi, \cos\varphi, 0)^T$. The second rotation $\boldsymbol{R}_2$ determines the vector $\boldsymbol{r}_0 \in \mathbb{S}^2_{\perp \boldsymbol{r}_2}$. The rotation $\boldsymbol{R}_2$ should leave $\boldsymbol{r}_2$ unchanged, so we can choose $\boldsymbol{r}_2$ as the axis, and we shall denote by $\omega \in [0, 2\pi)$ the angle. The total rotation $\boldsymbol{R}_{\text{ortho}}$ reads

$$\boldsymbol{R}_{\text{ortho}} = \boldsymbol{R}_2(\boldsymbol{r}_2, \omega)\boldsymbol{R}_1(\boldsymbol{r}_2^{\perp}, \theta) \triangleq \boldsymbol{R}_{\text{ortho}}(\theta, \varphi, \omega). \tag{3.12}$$

We note that the angle ω is uniquely determined by the choice of $\boldsymbol{r}_0$, since $\boldsymbol{r}_0 = \boldsymbol{R}_2\boldsymbol{R}_1\boldsymbol{e}_x$. We eventually make the connection with the zyz-Euler angle parametrization, since this will be needed in the subsequent sections. It is possible to show that[65]

$$\boldsymbol{R}_{\text{Euler}}(\varphi, \theta, \psi) = \boldsymbol{R}_{\text{ortho}}(\varphi, \theta, \omega - \varphi). \tag{3.13}$$

The change of parametrization is then only the application of an offset to the last angle. This last parametrization highlights the connection between $SO(3)$ and the tensor product $\mathbb{S}^2 \times \mathbb{S}^1$, from which we will take advantage later on, in order to build uniform sampling schemes and quadrature results.

3.1.3 Harmonic analysis on $SO(3)$

Let $f : SO(3) \to \mathbb{C}, \quad f \in L^2(SO(3))$ *i.e.* f is a square integrable function with respect to the normalized Haar measure on $SO(3)$:

$$\int_{SO(3)} |f(\boldsymbol{R})|^2 \mathrm{d}\mu(\boldsymbol{R}) < \infty, \tag{3.14}$$

where $\mu(\boldsymbol{R})$ is the normalized Haar measure which reads in Euler angle coordinates

$$\mathrm{d}\mu(\boldsymbol{R}) = \frac{1}{8\pi^2} \sin\theta \, \mathrm{d}\varphi \, \mathrm{d}\theta \, \mathrm{d}\psi. \tag{3.15}$$

The Peter-Weyl theorem[66,67] in the $SO(3)$ setting gives the harmonic basis for $L^2(SO(3))$. These functions are the Wigner-D functions $\{D_l^{m,n} | l \in \mathbb{N}, |m| \leq l, |n| \leq l\}$, which read in zyz-Euler angles parametrization $(\varphi, \theta, \psi) \in [0, 2\pi) \times [0, \pi] \times [0, 2\pi)$

$$D_l^{m,n}(\varphi, \theta, \psi) = \exp(-im\varphi) d_l^{m,n}(\theta) \exp(-in\psi), \tag{3.16}$$

[64] JULIE C MITCHELL. *SIAM Journal on Scientific Computing*, **30**: 525–547, 2008.

[65] MANUEL GRÄF and DANIEL POTTS. *Numerical Functional Analysis and Optimization*, **30**: 665–688, 2009.

[66] ASIM ORHAN BARUT and RYSZARD RACZKA. *Theory of group representations and applications*. vol. 2 World Scientific, 1986.

[67] SALEM SAID et al. *arXiv preprint arXiv:0907.2601*, , 2009.

where the $d_l^{m,n}(\theta)$ functions are called the Wigner-d functions which are defined by the following expression[61]

$$d_l^{m,n}(\theta) = \sum_k \left[\frac{(-1)^k \left[(j+m)!(j-m)!(j+n)!(j-n)!\right]^{1/2}}{k!(l+n-k)!(j-m-k)!(k+m-n)!} \times \left(\cos\frac{\theta}{2}\right)^{2l-2k-m+n} \left(-\sin\frac{\theta}{2}\right)^{2k+m-n} \right]. \tag{3.17}$$

As a side note, we shall remark that the $d_l^{m,n}$ functions defined here are real-valued. This is a special feature of the zyz convention for the Euler angles, which may explain its popularity among physicists. As in classical Fourier series analysis – where the basis function are complex exponentials rather than Wigner-D functions – we can write any function $f \in L^2[SO(3)]$ as an infinite sum of increasing frequency Wigner-D functions. The frequency here is controlled by the value of the degree $l \in \mathbb{N}$ in the $D_l^{m,n}$ functions. The decomposition of an arbitrary function $f \in L^2[SO(3)]$ is given by

$$f(\boldsymbol{R}) = f(\varphi,\theta,\psi) = \sum_{l=0}^{\infty} \sum_{|m|,|n|\leq l} f_l^{m,n} D_l^{m,n}(\varphi,\theta,\psi), \tag{3.18}$$

where the $f_l^{m,n}$ are the coefficients obtained by the projection of f onto the corresponding Wigner-D function

$$f_l^{m,n} \triangleq \frac{1}{8\pi^2} \int_{SO(3)} \overline{f(\varphi,\theta,\psi)} D_l^{m,n}(\varphi,\theta,\psi) \sin\theta \,\mathrm{d}\varphi \,\mathrm{d}\theta \,\mathrm{d}\psi. \tag{3.19}$$

We define bandlimited functions on the rotation group in the same way we have defined bandlimited functions on the ball. Precisely, we say that f is L-bandlimited if there exists an integer L such that, for all $l \geq L$, we have $f_l^{m,n} = 0$.

3.2 Uniform sampling on $SO(3)$

In this section we focus on the design of uniform deterministic sampling sets on $SO(3)$. One shall note that, since we are no longer working in Euclidean space, we have to define tools to evaluate the *uniformity* and the *resolution* of such sampling sets. This is done in section 3.2.1. We then introduce different sampling methods on $SO(3)$ in section 3.2.2 and compare their respective performance at different resolutions in section 3.2.3.

3.2.1 Measuring sampling uniformity

Let $\mathcal{X}(SO(3))$ be a sampling set over the rotation group $SO(3)$. The target angular step, or equivalently the separation distance $\alpha(\mathcal{X}(SO(3)))$ is defined by

$$\alpha(\mathcal{X}(SO(3))) = \min_{\substack{\boldsymbol{R}_i \neq \boldsymbol{R}_j \\ \boldsymbol{R}_i, \boldsymbol{R}_j \in \mathcal{X}(SO(3))}} d_{SO(3)}(\boldsymbol{R}_i, \boldsymbol{R}_j). \tag{3.20}$$

There are several ways of defining the uniformity of a sampling scheme on a Riemannian manifold. On $SO(3)$, a few were introduced such as global coverage, local separation, dispersion or discrepancy to name all but a few.[65,68,69] Each of these criteria have a rigorous definition which is beyond this work. A simpler criterion however can be formulated to perform a quick analysis of the quality of a given sampling set. This criterion consists in the minimization of a repulsive potential energy, as it would be done for a set of charged particles in electrostatics for instance. This repulsive potential reads

$$E = \sum_{i=0}^{M-1} \sum_{j=i+1}^{M-1} d_{SO(3)}^{-p}(\boldsymbol{R}_i, \boldsymbol{R}_j) \quad (p > 0) \tag{3.21}$$

where M is the size of the sample and p is the repulsive order allowing tuning of the criteria. For all our comparisons we will solely use the case $p = 1$, although a wide range of other values has already been investigated in the literature.[64]

[68] ANNA YERSHOVA et al. *The International journal of robotics research*, , 2009.

[69] ANNA YERSHOVA and STEVEN M LAVALLE. "Deterministic sampling methods for spheres and SO (3)" in: *Robotics and Automation, 2004. Proceedings. ICRA'04. 2004 IEEE International Conference on*. vol. 4 IEEE 2004. 3974–3980

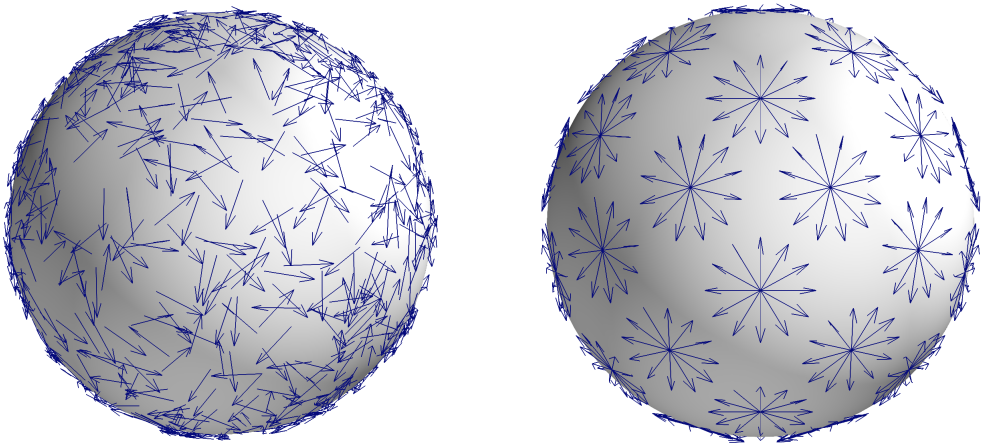

(a) (b)

Figure 3.1 : Comparison between uniform random sampling and uniform deterministic sampling on $SO(3)$. Each sample $\boldsymbol{R} = (\boldsymbol{r}_0, \boldsymbol{r}_1, \boldsymbol{r}_2)$ is represented by an oriented arrow on the 2-sphere. Each sample corresponds to the doublet $(\boldsymbol{r}_2, \boldsymbol{r}_0)$, where $\boldsymbol{r}_2$ is the base point on $\mathbb{S}^2$ and $\boldsymbol{r}_0$ lies in the tangent plane $\mathbb{S}^2_{\perp \boldsymbol{r}_2} \cong \mathbb{S}^1$. (a) Uniform random sampling on $SO(3)$ with $N = 1000$ samples. (b) Uniform deterministic sampling using the Healpix-based method, for resolution parameter $n_{\text{side}} = 2$, which give 576 samples on $SO(3)$.

3.2.2 Sampling schemes

We start by considering the specific case of uniform random sampling on $SO(3)$, and we then introduce several deterministic sampling schemes. Precisely the uniform random sampling scheme is needed to simulate the random orientation taken by the biomolecule in the single-particle experiment, that is in our formalism the rotation $\boldsymbol{R}_k$ defined in section 1.2.3. The deterministic sampling sets are at the heart of the Expectation-Maximization-Compression (EMC) algorithm, and these deterministic rotations are used to assemble the two-dimensional diffraction pattern into a consistent three-dimensional intensity.

Random uniform sampling

Using the quaternion representation of rotations, it is quite straightforward to obtain uniform random samples from random uniform quaternion of unit length, that is each sample belongs to the 3-sphere.[70,71] The method relies on three intermediate random variables,

$$s \sim \mathcal{U}([0,1]), \quad \theta_1 \sim \mathcal{U}([0,2\pi]), \quad \theta_2 \sim \mathcal{U}([0,2\pi]). \tag{3.22}$$

The corresponding unit quaternion $\boldsymbol{q}$, drawn according to the uniform distribution on $\mathbb{S}^3$ is then given by

$$q_0 = \sqrt{1-s}\cos\theta_2, \quad q_1 = s\sin\theta_1, \quad q_2 = s\cos\theta_1, \quad \sqrt{1-s}\sin\theta_2, \quad \boldsymbol{q} = (q_0, q_1, q_2, q_3). \tag{3.23}$$

One should note that this method may be close to optimal in terms of robustness and speed. There exists others methods described in the literature such as random uniform sampling of Euler angles,[29,70] which is very similar to its deterministic counterpart, the variable stepping method which is described in the next section.

Variable stepping

The variable stepping method, *i.e.* the deterministic discretization of the Euler angles triplet $(\varphi, \theta, \psi) \in [0, 2\pi] \times [0, \pi] \times [0, 2\pi]$ is now discussed. In this method, the angles θ and ψ are sampled uniformly

[70] JAMES J KUFFNER. "Effective sampling and distance metrics for 3D rigid body path planning" in: *Robotics and Automation, 2004. Proceedings. ICRA'04. 2004 IEEE International Conference on*. vol. 4 IEEE 2004. 3993–3998

[71] KEN SHOEMAKE. "Uniform random rotations" in: *Graphics Gems III*. Academic Press Professional, Inc. 1992. 124–132

at the target angular step α, whereas the angle φ is sampled uniformly according to $\alpha' = g(\alpha, \theta)$, where

$$g(\alpha, \theta) = \frac{\alpha}{\sin\theta}. \tag{3.24}$$

Since for certain values of θ near $\theta = 0$ or $\theta = \pi$ it can occur that the induced step α' exceeds 2π, only $\varphi = 0$ is sampled. As suggested by the notation, the first two angles (φ, θ) uniquely determine $\boldsymbol{r}_2$ on the 2-sphere, as shown by equation (3.9). To obtain an uniform coverage of the 2-sphere with the vectors $\boldsymbol{r}_2$, we remark that for a given colatitude angle θ the circumference of the circle obtained by varying the azimuth φ all over the interval $[0, 2\pi]$ is equal to $2\pi \sin\theta$. Equation (3.24) simply states that ratio of number of points sampled on each circle should be equal to the ratio of each circle length,

$$\frac{\alpha'}{\alpha} = \frac{2\pi}{2\pi \sin\theta} = \frac{1}{\sin\theta}. \tag{3.25}$$

From a numerical perspective however, this method has to be slightly modified so it is tractable. Indeed it is not possible to sample the Euler angles uniformly for an arbitrary value of α: for instance, sampling uniformly $\psi \in [0, 2\pi]$ at α is only feasible when the ratio $2\pi/\alpha$ is a integer, which in practice is never the case. Instead, we compute $\lceil 2\pi/\alpha \rceil$ and obtain a new target angular angle, $\tilde{\alpha}_\psi$, such that

$$\tilde{\alpha}_\psi = \frac{2\pi}{\lceil \frac{2\pi}{\alpha} \rceil}, \tag{3.26}$$

where $\lceil \cdot \rceil$ stands for the ceiling function. The same approach applies to the angle θ, leading to $\tilde{\alpha}_\theta = \pi / \lceil \frac{\pi}{\alpha} \rceil$. Now remains the case of the angle $\varphi \in [0, 2\pi]$. The same type of argument leads to a similar result,

$$\tilde{\alpha}'_\varphi = \frac{2\pi}{\lceil \frac{2\pi}{\alpha'} \rceil} = \frac{2\pi}{\lceil \frac{2\pi \sin\theta}{\alpha} \rceil}, \tag{3.27}$$

where $\tilde{\alpha}'_\varphi$ is the new uniform sampling rate for the angle φ. We remark however that these corrections barely affect the angular resolution of the sampling, since $\tilde{\alpha}_\psi \simeq \tilde{\alpha}_\theta \simeq \alpha$ and $\tilde{\alpha}'_\varphi \simeq \alpha'$ as the target angular distance diminishes.

Healpix-based sampling

This sampling scheme is based on the orthogonal axes parametrization. This parametrization highlights the connection between $SO(3)$ and the tensor product $\mathbb{S}^2 \times \mathbb{S}^1$. As a consequence we can think of a uniform sampling scheme $\mathcal{X}(SO(3))$ as being constructed from uniform sampling schemes $\mathcal{X}(\mathbb{S}^2)$ and $\mathcal{X}(\mathbb{S}^1)$ respectively. This is stated in Theorem 1. We introduce metrics on $\mathbb{S}^2$ and $\mathbb{S}^1$,

$$d_{\mathbb{S}^2}(\boldsymbol{x}_1, \boldsymbol{x}_2) \triangleq \arccos \boldsymbol{x}_1^T \boldsymbol{x}_2, \quad \boldsymbol{x}_1, \boldsymbol{x}_2 \in \mathbb{S}^2, \tag{3.28}$$

$$d_{\mathbb{S}^1}(\omega_1, \omega_2) \triangleq \arccos\cos(\omega_1 - \omega_2), \quad \omega_1, \omega_2 \in [0, 2\pi). \tag{3.29}$$

The corresponding target angular steps on $\mathbb{S}^2$ and $\mathbb{S}^1$ are then given by

$$\alpha(\mathcal{X}(\mathbb{S}^2)) = \min_{\substack{\boldsymbol{x}_i \neq \boldsymbol{x}_j \\ \boldsymbol{x}_i, \boldsymbol{x}_j \in \mathcal{X}(\mathbb{S}^2)}} d_{\mathbb{S}^2}(\boldsymbol{x}_i, \boldsymbol{x}_j) \tag{3.30}$$

$$\alpha(\mathcal{X}(\mathbb{S}^1)) = \min_{\substack{\omega_i \neq \omega_j \\ \omega_i, \omega_j \in \mathcal{X}(\mathbb{S}^1)}} d_{\mathbb{S}^1}(\omega_i, \omega_j). \tag{3.31}$$

Theorem 1 (Gräf and Potts). *Let the sampling sets*

$$\mathcal{X}(\mathbb{S}^2) \triangleq \left\{(\varphi_i, \theta_i) \in \mathbb{S}^2, i = 0, \ldots, M_1 - 1\right\} \tag{3.32}$$

$$\mathcal{X}(\mathbb{S}^1) \triangleq \left\{w_j \in \mathbb{S}^2, j = 0, \ldots, M_2 - 1\right\} \tag{3.33}$$

with target angular step $\alpha = \alpha(\mathcal{X}(\mathbb{S}^2)) = \alpha(\mathcal{X}(\mathbb{S}^1))$. *Then for arbitrary offsets* $c_i \in \mathbb{S}^1$, $i = 0 \ldots, M_1 - 1$, *the sampling set*

$$\mathcal{X}_{ortho}(SO(3)) \triangleq \{\boldsymbol{R}_{ortho}(\varphi_i, \theta_i, \omega_j + c_i) | i = 0, \ldots, M_1 - 1, j = 0, \ldots, M_2 - 1\} \tag{3.34}$$

has a target angular step $\alpha(\mathcal{X}_{ortho}(SO(3))) = \alpha$.

The uniformity of the sampling scheme $\mathcal{X}_{\text{ortho}}(SO(3))$ is thus obtained by balancing the sampling rates in each subspace accordingly. This theorem somewhat formalizes the balancing property between $\mathbb{S}^2$ and $\mathbb{S}^1$ sampling rates estimated by Mitchell,[64] which we recall here. Given a target angular step α, the number of elements in each subspace have to satisfy

$$|\mathcal{X}(\mathbb{S}^2)| = \left\lceil \frac{4\pi}{\alpha^2} \right\rceil, \qquad |\mathcal{X}(\mathbb{S}^1)| = \left\lceil \frac{2\pi}{\alpha} \right\rceil \tag{3.35}$$

where $|\cdot|$ denotes the cardinality of each set. With this condition at hand, we are able to discretize each subspace accordingly. The simplest way to obtain a set $\mathcal{X}(\mathbb{S}^1)$ verifying the condition (3.35) is to sample the circle $\mathbb{S}^1$ at the target angular step $\tilde{\alpha} = \lceil 2\pi/(\frac{2\pi}{\alpha}) \rceil$ according to the same arguments as for the variable stepping method. For $\mathcal{X}(\mathbb{S}^2)$ however the task is not trivial. Since the equation (3.35) suggests that we have to divide the 2-sphere $\mathbb{S}^2$ in pixel of equal area α^2, we choose to use the HEALPix discretization scheme,[56] which exhibits an equal area partition of the 2-sphere. We refer the reader to section 2.2.1 where the HEALPix discretization scheme is studied in detail. We recall that HEALPix is a hierarchical sampling controled by a refinement parameter n_{side}, and the number of samples (pixels) n_{pix} is given by

$$n_{\text{pix}} = 12\, n_{\text{side}}^2. \tag{3.36}$$

Therefore the set of values available for α will be discrete, as a function of n_{side}. The resulting value of α is approximated by

$$\alpha = \sqrt{\frac{\pi}{3}}\, (n_{\text{side}})^{-1}. \tag{3.37}$$

The HEALPix-based sampling scheme, for a resolution n_{side}, is explicitly given by

$$\mathcal{X}_{\text{ortho}}(SO(3)) = \left\{ R_{\text{ortho}}(\varphi_i, \theta_i, \omega_j) | i = 0, \ldots, n_{\text{pix}} - 1,\ \omega_j = \frac{\tilde{\alpha}}{2\pi} j,\ j = 0, \ldots, \frac{2\pi}{\tilde{\alpha}} - 1 \right\} \tag{3.38}$$

The number of elements M in the sampling set $\mathcal{X}_{\text{ortho}}(SO(3))$ as a function of the resolution parameter n_{side} is given by

$$M(n_{\text{side}}) = 12 n_{\text{side}}^2 \cdot \left\lceil 2\pi \sqrt{\frac{3}{\pi}} n_{\text{side}} - 1 \right\rceil. \tag{3.39}$$

Platonic solids and sampling schemes

It is also possible to take advantage of the tensor product structure $\mathbb{S}^2 \times \mathbb{S}^1$ of the rotation group in a different way. In virtue of the parametrization in orthogonal axes and Theorem 1, a few number of sampling schemes can be obtained based on Platonic solids: the tetrahedron, octahedron and icosahedron. Indeed each vertex of a Platonic solid will define a base point in $\mathbb{S}^2$, as required in the orthogonal axes parametrization. Then the uniformity constraint of Theorem 1 is given by the inherent regularity of Platonic solids, and by discretizing at the correct angular step the subspace $\mathbb{S}^1$. The usage of Platonic solids was suggested earlier[69] but the present method was introduced recently.[65] The vertices of the three Platonic solids considered are given by

$$\mathcal{T} \triangleq \left\{ \boldsymbol{x}_0 = \boldsymbol{e}_z,\ \boldsymbol{x}_i = \left(\frac{2}{3} i\pi, \arccos -\frac{1}{3} \right) \middle| i = 1, 2, 3 \right\} \tag{3.40}$$

$$\mathcal{O} \triangleq \left\{ \boldsymbol{x}_0 = \boldsymbol{e}_z,\ \boldsymbol{x}_5 = -\boldsymbol{e}_z,\ \boldsymbol{x}_i = \left(\frac{1}{2} i\pi, \frac{\pi}{2} \right) \middle| i = 1, \ldots, 4 \right\} \tag{3.41}$$

$$\mathcal{I} \triangleq \left\{ \boldsymbol{x}_0 = \boldsymbol{e}_z,\ \boldsymbol{x}_{11} = -\boldsymbol{e}_z,\ \boldsymbol{x}_i = \left(\frac{2}{5} i\pi, \arctan 2 \right),\ \boldsymbol{x}_{i+5} = \left(\frac{2}{5}\pi + \frac{1}{5}\pi, \pi - \arctan 2 \right) \middle| i = 1, \ldots, 5 \right\} \tag{3.42}$$

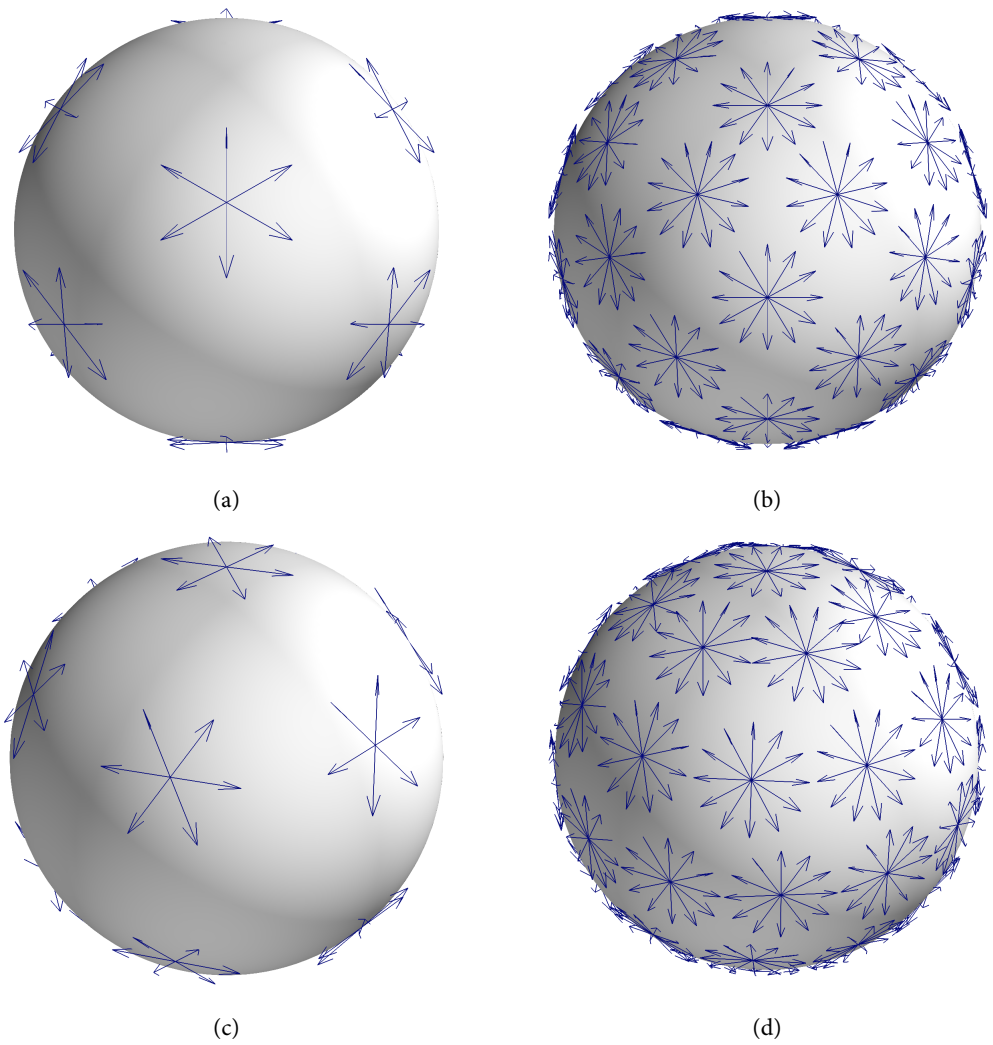

(a) (b)

(c) (d)

Figure 3.2 : Comparison between the variable stepping method and HEALPix based sampling. (a) and (b) HEALPix sampling with $n_{\text{side}} = 1, 2$, which gives 72 and 576 samples on $SO(3)$ respectively. (c) and (d) Variable stepping method with corresponding values of α as a function of n_{side}. We obtain 84 and 612 samples respectively.

where we have used the short-hand notation $\boldsymbol{x}_i = (\varphi_i, \theta_i)$ for better readability. The corresponding rotation group sampling schemes are then obtained

$$\mathcal{X}_T \triangleq \left\{ \boldsymbol{R}_{\text{ortho}} \left(\boldsymbol{x}_i, \frac{2}{3}k\pi + c_i \right) \middle| \boldsymbol{x}_i \in \mathcal{T},\ c_i = (1 - \delta_{0,i})\frac{\pi}{3};\ i = 0, \dots, 3,\ k = 0, 1, 2 \right\} \tag{3.43}$$

$$\mathcal{X}_0 \triangleq \left\{ \boldsymbol{R}_{\text{ortho}} \left(\boldsymbol{x}_i, \frac{1}{2}k\pi + c_i \right) \middle| \boldsymbol{x}_i \in \mathcal{O},\ c_i = 0;\ i = 0, \dots, 5,\ k = 0, \dots, 3 \right\} \tag{3.44}$$

$$\mathcal{X}_I \triangleq \left\{ \boldsymbol{R}_{\text{ortho}} \left(\boldsymbol{x}_i, \frac{2}{5}k\pi + c_i \right) \middle| \boldsymbol{x}_i \in \mathcal{I},\ c_i = (1 - \delta_{0,i})(1 - \delta_{11,i})\frac{\pi}{5};\ i = 0, \dots, 11,\ k = 0, \dots, 4 \right\}. \tag{3.45}$$

These sampling schemes have respective sizes, $|\mathcal{X}_T| = 12$, $|\mathcal{X}_O| = 24$ and $|\mathcal{X}_I| = 60$. One shall note that other sampling schemes can be obtained with the same approach using different Platonic solids, such as the hexahedron or the dodecahedron. As we will see in section 3.3, these sampling schemes will be of particular importance when evaluating integrals of low-frequency functions, due to the small sample size compared to the other sampling schemes already introduced.

3.2.3 Comparison

We have introduced a variety of uniform sampling schemes on the rotation group $SO(3)$. We may visualize a sampling set $\mathcal{X} \subset SO(3)$ at a set of oriented arrows on the surface on the 2-sphere. The

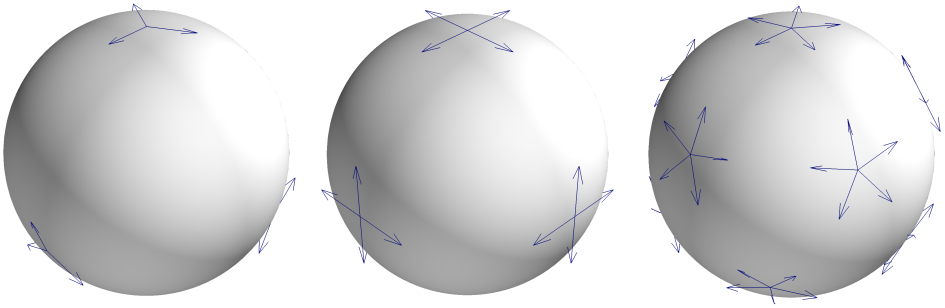

(a) (b) (c)

Figure 3.3 : The three Platonic-based sampling schemes of $SO(3)$. (a) Tetrahedron-based $\mathcal{X}_T$ (b) Octahedron-based $\mathcal{X}_O$ (c) Icosahedron-based $\mathcal{X}_I$.

reason is the following: based on the tensor product $\mathbb{S}^2 \times \mathbb{S}^1$ parametrization of the rotation group, one may think of a element $\boldsymbol{R} = (\boldsymbol{r}_0, \boldsymbol{r}_1, \boldsymbol{r}_2) \in \mathcal{X}$ as a doublet $(\boldsymbol{r}_2, \boldsymbol{r}_0)$ where $\boldsymbol{r}_2$ is the base point on $\mathbb{S}^2$ to which the vector $\boldsymbol{r}_0$ is attached. Moreover, since $\boldsymbol{r}_0$ lies in the tangent plane at $\boldsymbol{r}_2$ by construction, we have $\boldsymbol{r}_0 \in \mathbb{S}^2_{\perp \boldsymbol{r}_2}$. This representation is also quite interesting since it allows the representation of a 3-dimensional manifold ($SO(3)$) in the three-dimensional Euclidean space $\mathbb{R}^3$.

On figure 3.1a we have represented a random sampling set of size $N = 1000$ built using the method presented in 3.2.2 along with an HEALPix based sampling set for $n_{\text{side}} = 2$ on figure 3.1b. These two figures illustrate the difference between random and deterministic uniform sampling in terms of angular resolution α, which is guaranteed in the deterministic approach whereas absent in the random case due to the finite number of samples. HEALPix based sampling sets for resolutions $n_{\text{side}} = 1$ and $n_{\text{side}} = 2$ are depicted on figure 3.2a and 3.2b, respectively. The corresponding sets for the variable stepping method at target angle $\alpha(n_{\text{side}})$ are plotted on figure 3.2c and 3.2d. The HEALPix approach seems qualitatively to lead to better results in terms of uniformity: this will be confirmed by the energy criteria (3.21).

We are now interested in the performance of each sampling method, *i.e.* determining how *uniform* the sampling is for a given angular resolution α. Leaving random uniform sampling as a special case we only consider uniform deterministic sampling schemes. We also exclude the Platonic solids based schemes, since they do not provide incremental covering of $SO(3)$ – however as mentioned they will be of much importance in section 3.3. We assess the relative performance of the variable stepping method and the HEALPix based sampling using the energy repulsion criteria (3.21). To maintain our comparison sensible, we compare HEALPix sampling schemes for different values of the resolution parameter n_{side} and compute the corresponding variable stepping scheme with parameter $\alpha(n_{\text{side}})$ (3.37). These results are summarized in Table 3.1. For the different resolutions n_{side} investigated, the set size obtained becomes more and more similar as the resolution increases: the relative difference between the variable stepping method and the HEALPix based method is about 16% for $n_{\text{side}} = 1$, whereas approaches 1% for $n_{\text{side}} = 8$. The repulsive energy E is higher with the variable stepping method than with the HEALPix based method for $n_{\text{side}} = 1, 2, 4$, with relative differences 52%, 12% and 3.2% respectively. For $n_{\text{side}} = 8$, the variable stepping method performs slightly better with a relative difference of 2.1%. We note that the variable stepping method performs better as far as n_{side} increases, and is better than the HEALPix based method. However in our application we will mainly consider low resolution sampling schemes, *i.e.* small values of n_{side}. In this case, the better coverage uniformity obtained in the HEALPix method, along with its simpler construction validates the choice of HEALPix based methods over the variable stepping method. This method also has the advantage of being self-contained with the rest of our work, since we also use the HEALPix grid to describe the intensity scattered by a protein in chapter 2.

3.3 Quadrature formulæ

Quadrature formulæ, or in short quadratures, are useful tools for the numerical evaluation of integrals. Let us consider a real-valued function $f : U \to \mathbb{R}$, where $U \subset \mathbb{R}$ is an arbitrary connected set.

n_{side}	α (°)	HEALPix		Variable stepping	
		E	Size	E	Size
1	58.6	$1.13e^3$	72	$1.72e^3$	84
2	29.3	$8.54e^4$	576	$9.65e^4$	612
4	14.7	$5.54e^6$	4608	$5.72e^6$	4680
8	7.33	$3.71e^8$	37632	$3.63e^8$	37240

Table 3.1 : Comparison between the different sampling schemes and their respective size and repulsive energies, for several values of refinement parameter n_{side}.

Then if we are able to write

$$\int_U f(x)\mathrm{d}x = \sum_{i=0}^{M-1} w_i f(x_i), \quad w_i \in \mathbb{R},\ x_i \in U,\ i = 0, \dots, M-1, \tag{3.46}$$

then such an equation is called a *quadrature formula*. It replaces the calculation of an integral by a weighted sum of the function f evaluated at M arbitrary *nodes* x_i, with *weights* w_i. Quadrature rules can be either exact or approximate: in the latter case the equal sign $(=)$ in (3.46) is replaced by an approximate sign $(\simeq)$. Quadrature rules range from simple, *e.g.* rectangle rule or trapezoidal rule, to more complex ones as Gauss-Legendre or Gauss-Laguerre rules. An extensive range of quadrature rules on Euclidean space can be found in the literature, see *e.g.* [72] for a complete overview.
Quadrature rules on Riemannian manifolds and groups are less common, but have attracted attention recently.[65,73] However quadrature rules on the 2-sphere holds a long history, due to its importance in many others fields such as geology or astrophysics.[74–78]

3.3.1 Quadrature rule on $SO(3)$

As we will see further on in the next chapter, the EMC algorithm involves computations of orientation probabilities. These probabilities are defined as integrals on $SO(3)$, and since we are interested in bandlimited reconstructions, the integrand is also bandlimited. In this section we thus develop quadrature formulæfor bandlimited functions on the rotation group $SO(3)$.
As we have seen in the previous section, exploiting the tensor product $\mathbb{S}^2 \times \mathbb{S}^1$ allows to translate results on $\mathbb{S}^2$ and $\mathbb{S}^1$ to the rotation group $SO(3)$. The same idea applies to obtain quadrature results on $SO(3)$. Theorem 2,[65] proves that quadrature on $SO(3)$ can be obtained from quadrature formulæ on $\mathbb{S}^2$ and $\mathbb{S}^1$, respectively.

Theorem 2 (Gräf and Potts). *For $L \geq 1$, let a quadrature rule $Q(\mathbb{S}^2)$ on the sphere $\mathbb{S}^2$ with degree of exactness $L-1$ by the sampling set $\mathcal{X}(\mathbb{S}^2) \triangleq \left\{(\varphi_i, \theta_i) \in \mathbb{S}^2, i = 0, \dots, M_1 - 1\right\}$ with weights $w_i(\mathbb{S}^2)$, be given,* i.e.

$$\frac{1}{4\pi}\int_0^{2\pi}\int_0^{\pi} Y_l^m(\varphi,\theta)\sin\theta \mathrm{d}\theta\mathrm{d}\varphi = \sum_{i=0}^{M_1-1} w_i(\mathbb{S}^2) Y_l^m(\varphi_i,\theta_i), \quad 0 \leq l \leq L-1, |m| \leq l. \tag{3.47}$$

Furthermore let a quadrature rule $Q(\mathbb{S}^1)$ with degree of exactness $L-1$ by the sampling set $\mathcal{X}(\mathbb{S}^1) \triangleq \{\psi_j, j = 0, \dots, M_2 - 1\}$ with weights $w_i(\mathbb{S}^2)$, be given, i.e.

$$\frac{1}{2\pi}\int_0^{2\pi} e^{in\psi}\mathrm{d}\psi = \sum_{j=0}^{M_2-1} w_j(\mathbb{S}^1) e^{in\psi_j}, \quad |n| \leq L-1. \tag{3.48}$$

[72] PHILIP J DAVIS and PHILIP RABINOWITZ. *Methods of numerical integration*. Courier Corporation, 2007.
[73] LUCA BRANDOLINI et al. *Annali della Scuola Normale Superiore di Pisa Classe di Scienze*, **13**: 889–923, 2014.
[74] KENDALL ATKINSON. *The Journal of the Australian Mathematical Society. Series B. Applied Mathematics*, **23**: 332–347, 1982.
[75] OSCAR L COLOMBO *Numerical methods for harmonic analysis on the sphere* tech. rep. DTIC Document, 1981
[76] MANUEL GRÄF. *Efficient algorithms for the computation of optimal quadrature points on riemannian manifolds*. 2013.
[77] VYACHESLAV IVANOVICH LEBEDEV. *USSR Computational Mathematics and Mathematical Physics*, **16**: 10–24, 1976.
[78] VI LEBEDEV and DN LAIKOV. "A quadrature formula for the sphere of the 131st algebraic order of accuracy" in: *Doklady. Mathematics.* vol. 59 3 MAIK Nauka/Interperiodica 1999. 477–481

Sampling scheme	Quadrature	Bandlimit	Size
$\mathcal{X}_T$	Exact	3	12
$\mathcal{X}_O$	Exact	4	24
$\mathcal{X}_I$	Exact	6	60
HEALPix	Approx.	$2n_{\text{side}}+1$	M

Table 3.2 : The different sampling schemes and their respective properties: exact or approximate, order of quadrature rules and size.

Then we obtain for arbitrary offsets $c_i \in \mathbb{R}$, $i = 0, \dots M_1 - 1$, a quadrature rule Q on the rotation group

$$\mathcal{X}(SO(3)) \triangleq \{\boldsymbol{R}_{Euler}(\varphi_i, \theta_i, \psi_j + c_i), \quad i = 0, \dots, M_1 - 1,\ j = 0, \dots, M_2 - 1\} \tag{3.49}$$

with corresponding weights

$$w_{i,j}(SO(3)) \triangleq w_i(\mathbb{S}^2) w_j(\mathbb{S}^1), \quad i = 0, \dots, M_1 - 1,\ j = 0, \dots, M_2 - 1 \tag{3.50}$$

That is, we integrate exactly all L-band-limited functions f by the formula

$$\int_{SO(3)} f(\boldsymbol{R}) \mathrm{d}\mu(\boldsymbol{R}) = \sum_{i=0}^{M_1-1} \sum_{j=0}^{M_2-1} w_{i,j}(SO(3)) f\left(\boldsymbol{R}_{Euler}(\varphi_i, \theta_i, \psi_j + c_i)\right) \tag{3.51}$$

Proof. The proof can be found in the original paper[65] and will not be reproduced here. ■

The same theorem can be extended to approximate quadrature rules, that is replacing at least one exact quadrature on $\mathbb{S}^1$ or $\mathbb{S}^2$ by an approximate quadrature will lead to an approximate quadrature on $SO(3)$. This would be useful in Corollary 2. A key consequence of this theorem is that it is indeed possible to build efficient quadrature rules on $SO(3)$ by considering efficient quadrature rules on $\mathbb{S}^2$ and $\mathbb{S}^1$. In the following section, we investigate the quadrature rules available with the sampling sets introduced in section 3.2.2.

3.3.2 Uniform sampling sets and associated bandlimit

Earlier in this chapter we introduced three uniform sampling sets based on Platonic solids: the tetrahedron, octahedron and icosahedron. These sets were denoted by $\mathcal{X}_T$, $\mathcal{X}_O$ and $\mathcal{X}_I$ respectively. The following corollary of theorem 2 associates an exact quadrature rule to each of these sets.

Corollary 1 (Exact quadrature rules). *The sampling sets $\mathcal{X}_T$, $\mathcal{X}_O$ and $\mathcal{X}_I$ respectively integrate exactly all 3, 4 and 6-band-limited functions $f \in L^2[SO(3)]$ by the formula*

$$\int_{SO(3)} f(\boldsymbol{R}) \mathrm{d}\mu(\boldsymbol{R}) = \frac{1}{|\mathcal{X}|} \sum_{R_i \in \mathcal{X}} f(\boldsymbol{R}_i), \tag{3.52}$$

where $\mathcal{X} = \mathcal{X}_T,\ \mathcal{X}_0,\ \mathcal{X}_I$.

Proof. For $\mathcal{X}_T$ and $\mathcal{X}_I$ the proof is straightforward quadrature rule with equal weights on $\mathbb{S}^2$ and $\mathbb{S}^1$, see for instance.[65,79] The case $\mathcal{X}_I$ is a bit more complicated, since application of theorem 2 would only give an exact quadrature for 5-band-limited functions. However a direct calculation shows that this quadrature formula is also exact for 6-band-limited functions.[65] ■

This result is very interesting in practice, since it may be that the sets $\mathcal{X}_T$, $\mathcal{X}_O$ and $\mathcal{X}_I$ are the smallest sets leading to exact quadrature rules with equal weights for 3, 4 and 6-band-limited functions. This is a very desirable property when computation time is critical as in the single-particle image reconstruction.

[79] YIMING HONG. *European Journal of Combinatorics*, **3**: 255–258, 1982.

However it is not clear whether these sampling sets can be generalized to higher band-limited functions, and exact quadrature rules may not be available. Nevertheless we can still introduce approximate quadrature rules using the HEALPix based sampling defined previously. Indeed the HEALPix sampling scheme on $\mathbb{S}^2$ leads to an approximate quadrature rule on $\mathbb{S}^2$ with a very good accuracy.[56] The following corollary extends this quadrature rule to the rotation group $SO(3)$.

Corollary 2 (Approximate quadrature rules). *Let $\mathcal{X}_{ortho}$ the HEALPix based sampling as constructed in section 3.2.2, with resolution parameter n_{side}. Consider a L-band-limited function f. Then we have the following approximate quadrature rule*

$$\int_{SO(3)} f(\boldsymbol{R}) \mathrm{d}\mu(\boldsymbol{R}) \simeq \frac{1}{M} \sum_{i=0}^{M} f\left(\boldsymbol{R}_i\right), \quad \boldsymbol{R}_i \in \mathcal{X}_{ortho}, \tag{3.53}$$

provided that $L \leq 2n_{side} + 1$.

Proof. The HEALPix grid at resolution n_{side} allows the accurate integration of spherical harmonics up to order $2n_{\text{side}}$, leading to an approximate quadrature rule of degree $L-1 = 2n_{\text{side}} - 1$ with uniform weights $w_i = 1/n_{\text{pix}}$. Now, following our construction of the HEALPix based sampling on $SO(3)$, we discretize uniformly $\mathbb{S}^1$ at a step $\tilde{\alpha} = \lceil 2\pi/(\frac{2\pi}{\alpha}) \rceil$, which leads to $N \simeq \lceil 2\pi/(\sqrt{(\pi/3)} n_{\text{side}} \rceil - 1$ points. This set of equidistant points defines a regular polygon on $\mathbb{S}^1$, and therefore leads to an exact quadrature rule[79] with equal weights $w_j = 1/N$ for $L' - 1 = N - 1$. Since it is clear that $L' > L$, the quadrature rule on $\mathbb{S}^1$ is also valid for L-band-limited functions. Applying theorem 2 leads to the result. ∎

From our application perspective, the two types of quadrature rules have their interest. Since computation time is the most critical constraint, the choice of the type of quadrature rule will be strongly tied with the number of nodes needed to evaluate the integral, *i.e.* the size of the sampling set involved. A nice property of the exact quadrature formulæ is that they require only a few nodes and are probably optimal in terms of sampling set size. However, one is not able to evaluate integrals of L-band-limited functions if $L \geq 1$. Despite its larger size, the HEALPix based sampling allows the accurate approximation of integrals of such functions, and offers a hierarchical structure via the refinement parameter n_{side}. The general properties of each sampling scheme are summarized in Table 3.2.

CHAPTER 4

A spherical-symmetry approach to the EMC algorithm

4.1 Three-dimensional intensity reconstruction by expectation-maximization

Single-particle imaging experiments promise to make the determination of atomic-resolved biomolecular structures realizable. We saw earlier that the ability to decipher the high-resolution structure of biomolecules involves two distinct processes. First the three-dimensional intensity function has to be estimated given the noisy, unoriented two-dimensional diffraction patterns. Then the electron density can be recovered during a so-called phase retrieval step.
We focus here on the intensity reconstruction problem. To this aim, Loh and Elser introduced the Expansion-Maximization-Compression (EMC) algorithm,[27] which has now been successfully applied to experimental data.[28] The algorithm is based upon an Expectation-Maximization (EM) algorithm.[80] The general feature of EM algorithms is that they provide an efficient way to estimate a model given missing or incomplete statistical data.
The EMC algorithm consists in an update rule of an intensity model $I_{\mathcal{G}} \rightarrow \tilde{I}_{\mathcal{G}}$ based on the definition of an appropriate likelihood function. In this section, we start by introducing the different notations, and then define each step of the EMC algorithm. We finally identify the limitations of the original algorithm and motivate our approach to the EMC algorithm.

4.1.1 Notations and assumptions

A dataset consists in K diffraction patterns, which are indexed by $k = 0 \dots K-1$. The diffraction patterns are recorded on a pixelated detector, where each pixel is labeled by index $i = 0 \dots N-1$ and has coordinates in reciprocal space $\boldsymbol{q}_i$. The $\boldsymbol{q}_i$ vectors describe a portion of an Ewald sphere, see section 1.2.2. We denote by Π_{ik} the photon count at pixel i, for an unknown orientation of the molecule $\boldsymbol{R}_k$ Throughout this work the random rotations $\boldsymbol{R}_k$ are assumed to be distributed uniformly on $SO(3)$ as free falling particules have no preferred orientation, especially with the use of aerosol injectors. We explained in section 3.2.2 how such rotations could be simulated. Given the low photon counts expected in single-particle experiments, a good approximation is that the photon count Π_{ik} follows a Poisson process, where the underlying parameter is given by $I(\boldsymbol{q}_i, \boldsymbol{R}_k)$, which is the value of the continuous intensity function I at the pixel i, for a rotation of the molecule $\boldsymbol{R}_k$. The formal expression of $I(\boldsymbol{q}_i, \boldsymbol{R}_k)$ is given in section 1.2.3, equation (1.13). In mathematical terms,

$$\Pi_{ik} \sim \mathcal{P}\left(I(\boldsymbol{q}_i, \boldsymbol{R}_k)\right), \tag{4.1}$$

where $\mathcal{P}(\lambda)$ denotes the Poisson process of parameter λ.
The EMC algorithm requires a deterministic rotation set $\mathcal{X} \subset SO(3)$ to compensate the missing information about the molecule orientation in the k-th experiment. Namely, the set $\mathcal{X}$ is defined by

$$\mathcal{X} \triangleq \{\boldsymbol{R}_j \in SO(3),\ j = 0 \dots M-1\}. \tag{4.2}$$

With the deterministic rotations $\boldsymbol{R}_j$ at hand, we are able to construct the tomographic grid. The combination of the reciprocal space coordinates $\boldsymbol{q}_i$ of the detector with the rotations $\boldsymbol{R}_j$ leads to the sequence of points $\boldsymbol{q}_{ij} \triangleq \boldsymbol{R}_j \cdot \boldsymbol{q}_i$ that constitutes the tomographic grid. We define the tomographic

[80] Arthur P Dempster, Nan M Laird, and Donald B Rubin. *Journal of the royal statistical society B*, 1–38, 1977.

intensities as

$$I_{ij} \triangleq I(\boldsymbol{R}_j \cdot \boldsymbol{q}_i) = I(\boldsymbol{q}_{ij}) \tag{4.3}$$

which is a redundant representation of the three-dimensional intensity model since it is possible to find i' and j' such that the points $\boldsymbol{q}_{i'j'}$ and $\boldsymbol{q}_{ij}$ are very close to each other. The tomographic intensities I_{ij} are at the heart of the EMC algorithm, as we shall see further.
The redundancy of the tomographic grid motivates the introduction of a regular grid to represent efficiently the estimated intensity model. We define the intensity model $I_{\mathcal{G}}$, which corresponds to the estimated intensity on a regular grid $\mathcal{G}$. The grid $\mathcal{G}$ is composed of N_{grid} nodes labeled by the index μ. In the original paper,[27] a regular three-dimensional Cartesian grid was used, whereas the work described in this chapter takes a different approach by using a spherical grid.

4.1.2 Principle

We start by defining the likelihood function, which will lead to the maximization step of the EMC algorithm. The log-likelihood function of the tomographic intensity $\tilde{I}_{ij}$ given the photon count Π_{ik} is given by

$$\mathcal{L}_{ijk}(\tilde{I}_{ij}, \boldsymbol{R}_j | \Pi_{ik}) = \log P(\Pi_{ik} | I_{ij}, \boldsymbol{R}_j) = \Pi_{ik} \log \tilde{I}_{ij} - \tilde{I}_{ij}, \tag{4.4}$$

where we have stripped away the irrelevant constant factor. If we assume that in a single experiment k, the Poisson processes on every pixel i are independent, we obtain the log-likelihood per orientation j and experiment k by simply summing over the detector pixels i:

$$\mathcal{L}_{jk}\left(\{\tilde{I}_{ij}\}_i, \boldsymbol{R}_j \middle| \{\Pi_{ik}\}_i\right) = \sum_{i=1}^{N} \mathcal{L}_{ijk}(\tilde{I}_{ij}, \boldsymbol{R}_j | \Pi_{ik}), \tag{4.5}$$

where the subscript i is a shorthand notation for $i = 0 \dots N$. The goal now is to obtain the total log-likelihood $\mathcal{L}$. First, we need to compute the probability P_{jk}, that is the probability that the diffraction pattern k corresponded to an orientation j of the molecule, conditionally on the current values of the tomographic intensity values I_{ij}. The unnormalized conditional probability is given by the joint Poisson probability distribution on every pixel i,

$$\prod_{i=0}^{N-1} P(\Pi_{ik} | I_{ij}, \boldsymbol{R}_j) = \prod_{i=0}^{N-1} I_{ij}^{\Pi_{ik}} \exp(-I_{ij}), \tag{4.6}$$

where again we have exploited the independence of the Poisson processes on each pixel, and omitted the j-independent factor in the Poisson probability distribution. The normalized probability distribution P_{jk} is given by

$$P_{jk} \triangleq P_{jk}\left(\boldsymbol{R}_j | \{\Pi_{ik}\}_i, \{I_{ij}\}_i\right) = \frac{w_j \prod_{i=0}^{N-1} I_{ij}^{\Pi_{ik}} \exp(-I_{ij})}{\sum_{j=0}^{M-1} w_j \prod_{i=0}^{N-1} I_{ij}^{\Pi_{ik}} \exp(-I_{ij})}. \tag{4.7}$$

The presence of the rotation weights w_j results from two different aspects. First, it can describe a non-uniform deterministic sampling of the rotation group $SO(3)$, which may be needed if the random rotations that affect the molecule are non-uniform (this may be the case with liquid-based molecule injectors). However the vast majority of the literature considers the uniform random rotation assumption, which is satisfied experimentally with aerosol injectors. In that case, the deterministic rotation sampling $\mathcal{X}$ needs to be uniform. As pointed out by Loh and Elser,[27] the rotation weights w_j may still be needed in the uniform case since it is not possible in general to obtain a sampling set such that the weights are uniform. This work circumvents this issue by using the sampling sets developed earlier in chapter 3.
The total likelihood function of the tomographic intensities $\tilde{I}_{ij}$ given the photon counts Π_{ik} and the current tomographic intensities I_{ij} is therefore given by

$$\mathcal{L}\left(\{\tilde{I}_{ij}\}_{i,j} \middle| \{\Pi_{ik}\}_{i,k}, \{I_{ij}\}_{i,j}\right) = \sum_{k=1}^{K} \sum_{j=0}^{M-1} P_{jk} \mathcal{L}_{jk}\left(\{\tilde{I}_{ij}\}_i, \boldsymbol{R}_j \middle| \{\Pi_{ik}\}_i\right). \tag{4.8}$$

$$I_{\mathcal{G}}(\boldsymbol{q}_\mu) \xrightarrow{\mathbf{E}} I_{ij} \xrightarrow{\mathbf{M}} \tilde{I}_{ij} \xrightarrow{\mathbf{C}} \tilde{I}_{\mathcal{G}}(\boldsymbol{q}_\mu)$$

Figure 4.1 : A single iteration of the EMC algorithm. The current model $I_{\mathcal{G}}$ is expanded on the tomographic grid such that $I_{ij} = I(\boldsymbol{q}_{ij})$. The current tomographic model I_{ij} is updated, leading to a new tomographic model $\tilde{I}_{ij}$ and compressed back to a new intensity model $\tilde{I}_{\mathcal{G}}$.

The maximization rule is obtained by taking the derivative of the total likelihood function with respect to the tomographic intensities $\tilde{I}_{ij}$. The likelihood expression (4.8) is quite practical since it allows an explicit and simple update rule:

$$(\mathbf{M}) : I_{ij} \to \tilde{I}_{ij} = \frac{\sum_{k=1}^{K} P_{jk}\Pi_{ik}}{\sum_{k=1}^{K} P_{jk}}. \tag{4.9}$$

The tomographic intensities I_{ij} give a redundant representation of the estimated intensity model. This over-specification of the intensity is solved by *compressing* or *condensing* the tomographic model I_{ij} back to the intensity model $I_{\mathcal{G}}$, which is defined on a regular grid $\mathcal{G}$,

$$(\mathbf{C}) : I_{ij} \to I_{\mathcal{G}}(\boldsymbol{q}_\mu). \tag{4.10}$$

The compression step has an intrinsic smoothing character: because the tomographic grid defined by the vectors $\boldsymbol{q}_{i,j}$ is much larger than the regular grid $\mathcal{G}$, the intensity $I_{\mathcal{G}}$ corresponds to an averaged version of the tomographic intensity.
The expansion step is the reverse of the compression step, that is from a regular intensity model $I_{\mathcal{G}}$ it creates the tomographic model needed by the maximization step:

$$(\mathbf{E}) : I_{\mathcal{G}}(\boldsymbol{q}_\mu) \to I_{ij}. \tag{4.11}$$

Here, the expansion step corresponds to an interpolation between the smaller grid, the regular grid, and the overspecified grid, the tomographic grid.
A single iteration $I_{\mathcal{G}} \to \tilde{I}_{\mathcal{G}}$ of the EMC therefore consists into three steps, the expansion step (E), the maximization step (M) and the compression step (C). This is summarized on figure 4.1. As a side note, we point out that the most computationally expensive step is the maximization step where we have to calculate the cross-probabilities P_{jk}, whereas the expansion and compression steps are much less expensive.

Remark It is interesting to note that the cross-probabilities P_{jk} are actually a discrete version of a continuous probability density function of the intensity given the orientation of the molecule. As a consequence the weights w_j can be seen as quadrature weights, and the discrete sum over the rotations in the likelihood function corresponds to the Expectation step in the EM algorithm.

4.1.3 Limitations of the original EMC algorithm and proposed improvements

The EMC algorithm, in its form presented by Loh and Elser presents several limitations. First it does not account for the particular geometry of the three-dimensional intensity function; as we have seen earlier in chapter 1 the intensity function is defined within a ball of certain radius. In its original form, the algorithm compresses the tomographic model to a regular model defined on a 3D Cartesian grid. In this work, we propose a spherical grid design in accordance with the intensity function geometry. The second limitation resides in the absence of control of the resolution of the reconstructed intensity $I_{\mathcal{G}}$. Even though the ultimate goal of single-particle experiments is atomically-resolved structures, we believe that intermediate resolutions are desirable, especially in experiments where they can be used to monitor in real-time the incoming data. In our work, we take advantage of both the Fourier-Laguerre sampling theorem on the ball and the Fourier-Laguerre transform on the ball to build intensity models at the desired resolution. This corresponds to the harmonic analysis on the ball developed earlier in chapter 2. We eventually note that the use of the Fourier-Laguerre expansion allows us to encode the different algebraic properties of the three dimensional intensity in its Fourier-Laguerre decomposition, as seen in section 2.1.3.

Thirdly, to the best of our knowledge, the only rotation group sampling $\mathcal{X}$ used today in the EMC is the one introduced by Loh and Elser, based on a regular polytope in $\mathbb{R}^4$, the 600-cell.[81,82] However the link between the reconstruction resolution and the sampling set size is rather qualitative, and the weights w_j defined above are non-uniform. Our approach proposes to use the sampling sets developed in chapter 3, where the weights w_j are uniform and the relationship between sampling size and resolution is clearly established.
Overall, we will show in the next section that these improvements effectively scale the problem, both in terms of complexity and computing time.

4.2 Equivalent spherical shell reconstruction problem

Taking into account the spherical geometry of the intensity function allows us to rephrase the estimation of the intensity function in a simpler way. Since an intensity function is defined within a ball of radius $q_{\text{max}}^{\text{dec}}$, we may represent the intensity function as a collection of concentric spherical shells, just like an onion. As a consequence, if we label the shells by $s = 0, 1, \ldots$, the three-dimensional intensity reconstruction problem boils down to the ability to solve a collection of two-dimensional intensity reconstruction problems, each on a spherical shell s.
This mental leap from three-dimensional reconstruction to two-dimensional reconstruction is depicted in figure 4.2. In figure 4.2.**A** we drew two circles on a typical (continuous) Bence-Jones protein diffraction pattern, where the radii correspond to reciprocal space values q_{in} and q_{out}. These two cases, which are further denoted as the *inner shell* and *outer shell* are chosen so that they represent well the nature of the estimation problem. Recall that a diffraction pattern is a spherical slice through the intensity function, known as the Ewald sphere, see section 1.2.2. The intersection between this spherical slice and the inner (resp. outer) shell defines a circle on the shell, as seen in figure 4.2.**B** and 4.2.**C**. These circles are indeed sampling points on the inner and outer shells, denoted by $\mathcal{D}^{\text{in}}$ and $\mathcal{D}^{\text{out}}$ respectively. Since each diffraction pattern correspond to a random orientation of the molecule, the equivalent sampling points on spherical shells are *rotated* versions of the reference sampling points $\mathcal{D}^{\text{in}}$ and $\mathcal{D}^{\text{out}}$, as represented in 4.2.**D** and 4.2.**E**. Finally, the actual measurements are Poisson realizations of the intensity defined at the sampling points $\mathcal{D}^{\text{in}}_{\boldsymbol{R}_k}$ and $\mathcal{D}^{\text{out}}_{\boldsymbol{R}_k}$. We note that the sparse measurements in the outer shell are characteristic of the single-particle imaging context and constitute a challenging problem.
In the remaining of this section, we first give the formal definition of equivalent measurement model on a single spherical shell, and then we detail the implementation of the spherical EMC algorithm. The formulation proposed here is a simplified version of the actual reconstruction problem, however it highlights the main features of the reconstruction process, and allows us to consider separately the mapping between the intensity measured on the planar detector and the corresponding point sampled on the sphere.

4.2.1 Equivalent measurement model on a single shell

Rephrasing the estimation problem within a signal processing framework start by defining an equivalent measurement model. As shown in figure 4.2.**A**, on a spherical shell s the corresponding *diffraction patterns* are mono-dimensional, as circles on this spherical shell. Formally, we will denote by $\mathcal{D}^s$ the *detector* on the shell, that is the reference sampling points. We define $\mathcal{D}^s$ as the set of N *pixels* coordinates on the sphere,

$$\mathcal{D}^s \triangleq \{\boldsymbol{q}_i = (q_s, \boldsymbol{\Omega}_i) | i = 1, 2, \ldots, N\}, \tag{4.12}$$

where $\boldsymbol{\Omega}_i = (\varphi_i, \theta(q_s)) \in [0, 2\pi) \times [0, \pi]$ are the angular coordinates, and q_s the radius of the spherical shell. The dependence of θ on the radius q_s is a consequence of the scattering geometry, as shown previously in equation (1.12). For completeness we recall that the relation is given by

$$\theta(q_s) = \frac{\pi}{2} - \arcsin \frac{q}{q_{\text{max}}}, \tag{4.13}$$

where q_{max} is defined in terms of the wavelength λ, see section 1.2.3.

[81] JOHN HORTON CONWAY and NEIL JAMES ALEXANDER SLOANE. *Sphere packings, lattices and groups*. vol. 290 Springer Science & Business Media, 2013.
[82] HAROLD SCOTT MACDONALD COXETER. *Regular polytopes*. Courier Corporation, 1973.

The number of pixels contributing to a shell, *i.e.* the number of pixels on a circle on the diffraction pattern increases with the radius q_s. Therefore to be consistent with the diffraction imaging context, the number of points N on the detector are also scaled as a function of q_s, such that:

$$N = \left\lceil \frac{2\pi q_s}{\Delta q} \right\rceil, \quad \varphi_i = \frac{2\pi}{N} i,\ i \in \{0, 1, \ldots, N-1\}, \tag{4.14}$$

where $\lceil \cdot \rceil$ denotes the ceiling function, and Δq is the reciprocal space pixel size.
Finally, each measurement, or diffraction pattern on a shell consists in a set of N samples Π_{ik}, $i = 0, \ldots, N-1$ given by:

$$\Pi_{ik} = \mathcal{P}\left(I(\boldsymbol{q}_i, \boldsymbol{R}_k)\right). \tag{4.15}$$

We also define the corresponding sampling points, for a rotation $\boldsymbol{R}_k$ by

$$\mathcal{D}^s_{\boldsymbol{R}_k} \triangleq \{\boldsymbol{R}_k \cdot \boldsymbol{q}_i | i = 0, 1, \ldots, N-1\}. \tag{4.16}$$

4.2.2 Spherical EMC algorithm implementation

We denote by I^s the intensity on the spherical shell s. We are interested in the reconstruction of sub-resolved intensity models, that is we look at models which read

$$I^s(\boldsymbol{\Omega}) = \sum_{l=0}^{L-1} \sum_{m=-l}^{l} I_l^m(q_s) Y_l^m(\boldsymbol{\Omega}) \tag{4.17}$$

where $L < L_s^{\lim}$ is the bandlimit of the reconstruction. To this aim, the spherical EMC algorithm proposed here consists of an update rule $I_l^m(q_s) \rightarrow \tilde{I}_l^m(q_s)$ of the spherical harmonic coefficients $I_l^m(q_s)$ of the intensity I^s. We recall that the spherical harmonic coefficients are a sparse representation of the intensity I^s, since they fulfill the properties enumerated in section 2.3.2.
Extending the EMC algorithm presented in section 4.1.2 to the single shell reconstruction problem is done easily, as we now describe.
In the spherical setting, the compression step corresponds to two distinct steps. First, the tomographic intensity model I_{ij} has to be compressed to a regular spherical grid $\mathcal{G}$, and thus the spherical harmonic coefficients can be retrieved with the Spherical Harmonic Transform (SHT)

$$(\mathbf{C}):\ \tilde{I}_{ij} \rightarrow \tilde{I}_{\mathcal{G}} \rightarrow \tilde{I}_l^m(q_s). \tag{4.18}$$

The expansion step is the reverse part, where we first apply the inverse SHT to get the intensity on the grid $I_{\mathcal{G}}$, and the tomographic model is obtained by interpolation between the grid $\mathcal{G}$ and the tomographic grid $\boldsymbol{q}_{ij}$,

$$(\mathbf{E}):\ I_l^m(q_s) \rightarrow I_{\mathcal{G}} \rightarrow I_{ij}. \tag{4.19}$$

The maximization step is left unchanged, but we slightly modify the definition of the cross probabilities P_{jk} such that

$$P_{jk} = \frac{\prod_{i=0}^{N-1} I_{ij}^{\Pi_{ik}} \exp(-I_{ij})}{\sum_{j=0}^{M-1} \prod_{i=0}^{N-1} I_{ij}^{\Pi_{ik}} \exp(-I_{ij})}, \tag{4.20}$$

inducing that the weights w_j have disappeared due to an appropriate choice of the rotation group sampling $\mathcal{X}$.

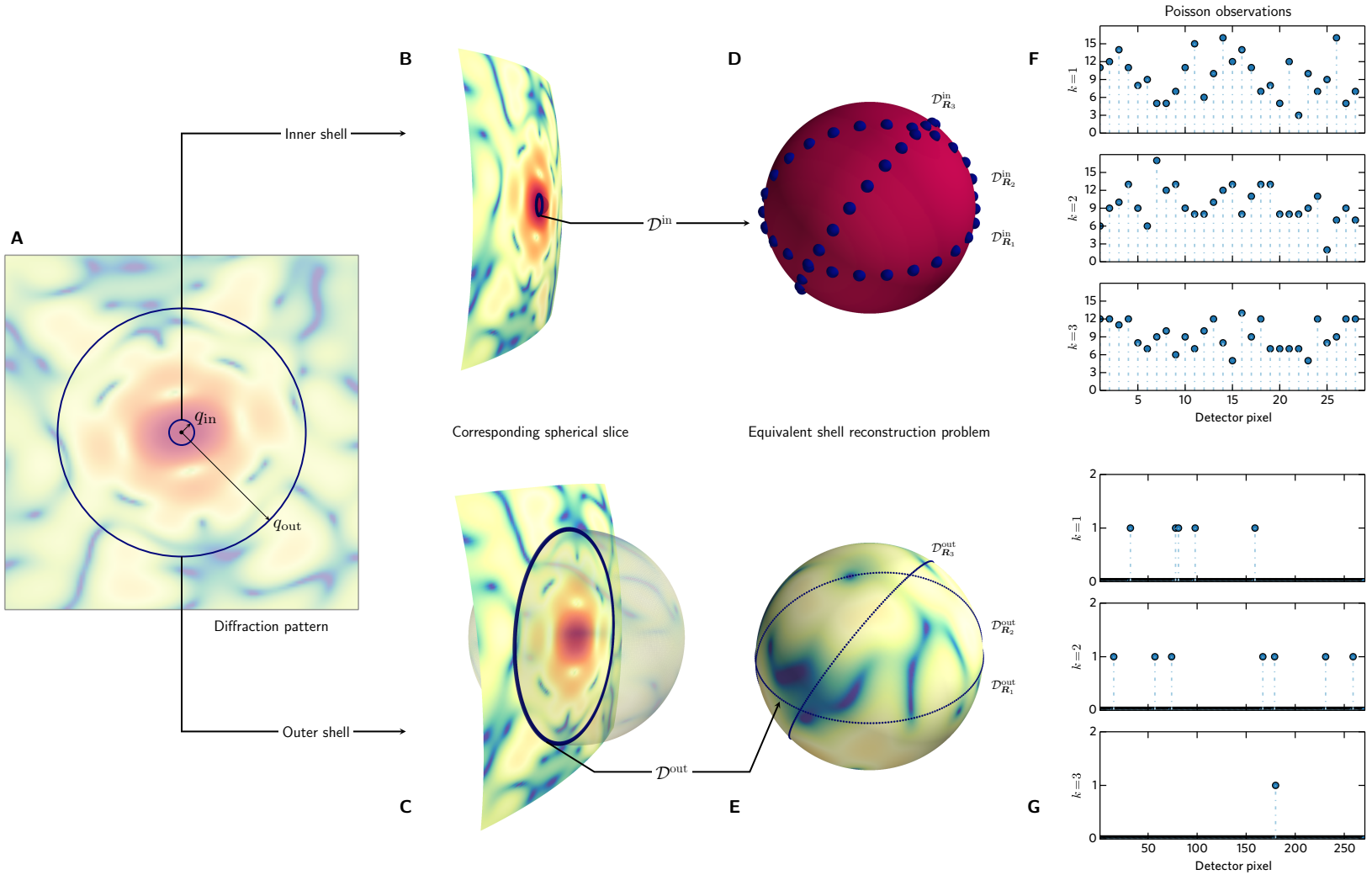

Figure 4.2 : Spherical shell equivalency for single-particle imaging. **A**: typical diffraction pattern, with two shells labelled (inner and outer). **B** and **C**: corresponding spherical slices through the shell intensity function. **D** and **E**: Equivalent shell reconstruction problem using one dimensional circular sampling points. **F** and **G**: Corresponding Poisson samples for the sampling locations labeled on **D** and **E**.

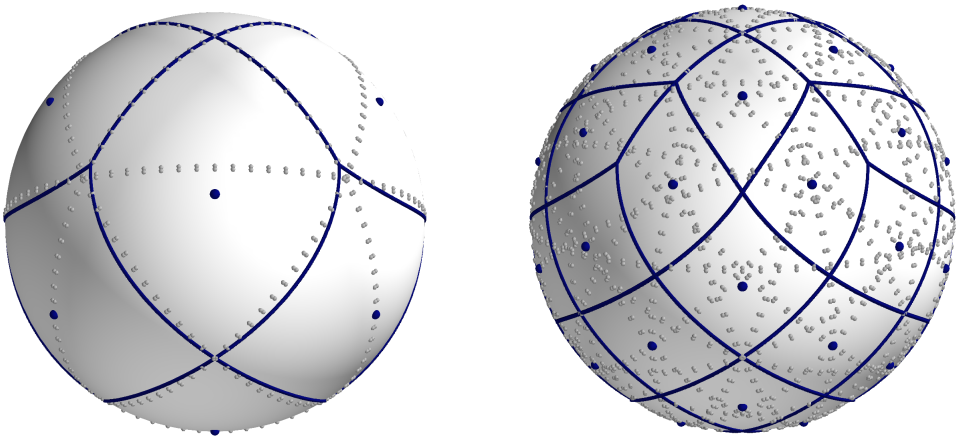

(a) $n_{\text{side}} = 1$, HEALPix-based sampling with $n_{\text{side}}^{\text{rot}} = 1$ (b) $n_{\text{side}} = 2$, HEALPix-based sampling with $n_{\text{side}}^{\text{rot}} = 2$

Figure 4.3 : Correspondence between the tomographic grid and the regular grid $\mathcal{G}$. The redundancy introduced by the tomographic grid (grey points) is compressed onto the regular grid $\mathcal{G}$ (blue points) by Inverse Distance Weighting (IDW) between the pixel center and the tomographic grid points belonging to this pixel.

Grid $\mathcal{G}$ and implementation of Expansion and Compression steps

We make use of the material introduced earlier in this manuscript by choosing the HEALPix sampling scheme on the sphere for our grid $\mathcal{G}$. For completeness we recall that this sampling scheme lacks an exact quadrature formula on the sphere, however it provides a good approximation of integrals of L-bandlimited functions provided that[56]

$$L \leq 2n_{\text{side}} + 1 \text{ with weights } w_\mu = \frac{4\pi}{n_{\text{pix}}},\ \mu = 1, 2, \ldots, n_{\text{pix}}, \tag{4.21}$$

where n_{side} is a resolution parameter and $n_{\text{pix}} = 12n_{\text{side}}^2$. Each point $\boldsymbol{q}_\mu$ in the HEALPix grid $\mathcal{G}$ is located at the center of its associated pixel. The pixels define an equal-area partition of the sphere.
The compression step is done as follows. We first determine the tomographic points $\boldsymbol{q}_{ij}$ belonging to each HEALPix pixel, and then the intensity value on this pixel is given by Inverse Distance Weighting (IDW) between the respective $\boldsymbol{q}_{ij}$ and the pixel center $\boldsymbol{q}_\mu$,

$$I(\boldsymbol{q}_\mu) = \frac{\sum_{\text{neighbors}} I_{ij}/\|\boldsymbol{q}_{ij} - \boldsymbol{q}_\mu\|^2}{\sum_{\text{neighbors}} 1/\|\boldsymbol{q}_{ij} - \boldsymbol{q}_\mu\|^2}. \tag{4.22}$$

The coefficients $I_l^m(q_s)$ are then computed up to order $L-1$ as given by the sampling theorem (4.21) using the set of routines available in the HEALPix package. The Friedel symmetry is restored by canceling the coefficients for odd values of l. The correspondence between the regular grid $\mathcal{G}$ and the tomographic grid is shown in figure 4.3, for the first two resolutions $n_{\text{side}} = 1, 2$ and HEALPix-based rotation group sampling with $n_{\text{side}}^{\text{rot}} = 1, 2$.
The expansion step is done by the successive expansion of the coefficients $I_l^m(q_s)$ to obtain $I_{\mathcal{G}}$, then by computation of the tomographic intensities by interpolation on the sphere. Precisely the intensity $I_{\mathcal{G}}$ is obtained by inverse SHT, again implemented using the HEALPix package routines. The interpolation from the regular grid $\mathcal{G}$ to the tomographic grid is done by bilinear interpolation using the four nearest-neighbors on the regular grid.

Rotation group sampling sets adaptative choice

The main purpose of the work presented in this manuscript is to give more insight on the choice of parameters of the EMC algorithm. Specifically, the focus is put on the choice of the rotation sampling set $\mathcal{X}$ with respect to the desired resolution of the reconstructed intensity. The motivation arises from the simple thought that it is more likely that estimating a low-resolution intensity model with a very large rotation sampling set will be a waste of time and computational resources.

Bandlimit L	Optimal grid $\mathcal{G}$		Optimal rotation group sampling $\mathcal{X}$	
	n_{side}	Size	Type	Size
3	1	12	$\mathcal{X}_T$	12
5	2	48	$\mathcal{X}_I$	60
9	4	192	HEALPix, $n_{\text{side}}^{\text{rot}} = 4$	4608
17	8	768	HEALPix, $n_{\text{side}}^{\text{rot}} = 8$	37632
33	16	3072	HEALPix, $n_{\text{side}}^{\text{rot}} = 16$	301056

Table 4.1 : Corresponding optimal choices of grid parameters and rotation sampling schemes, for increasing values of bandlimit L.

We have introduced earlier in chapter 3 several rotation sampling sets, and we gave the respective bandlimit $L_{\mathcal{X}}$ of the associated quadrature formula on $SO(3)$ for each of these sampling sets. The strong connection between $SO(3)$ and the sphere $\mathbb{S}^2$ leads to a simple choice criterion for the rotation sampling set given the bandlimit L of the reconstruction. Precisely, we consider that the quadrature bandlimit of the sampling set should be larger than the desired reconstruction bandlimit, that is

$$L_{\mathcal{X}} \geq L. \tag{4.23}$$

The *optimal* choice of $\mathcal{X}$ satisfying equation (4.23) is thus made by finding a rotation sampling set such that its size $|\mathcal{X}|$ is minimal. We give in table 4.1 the corresponding optimal choices of grids $\mathcal{G}$ and rotation sampling sets $\mathcal{X}$ for different values of bandlimit L.

4.2.3 Miscellaneous

We conclude this section with several technicalities, from numerical considerations to iterations convergence assessment.

Numerical considerations

Several numerical precautions need to be taken to make the numerical implementation of the algorithm more efficient. The most consuming time step is the computation of the probabilities P_{jk} (4.20). This step involves the computation of the joint probability (4.6) over the sampling points $\mathcal{D}^s$ on the spherical shell s. To avoid overflow/underflow in the computation of these probabilities, we rewrite (4.6) as

$$\log \prod_{i=0}^{N-1} P(\Pi_{ik} | I_{ij}, \boldsymbol{R}_j) = \sum_{i=0}^{N-1} \Pi_{ik} \log I_{ij} - I_{ij} \tag{4.24}$$

which is more efficient numerically. The value of the joint probability is then obtained by taking the exponential of the latter expression (4.24) and using an appropriate numerical library which allows the manipulation of very large and small numbers. Another improvement can be made given the sparse nature of the measurements Π_{ik}. In the outer shells, the scattering intensity is very low, and therefore the majority of the Π_{ik} values are equal to zero. Skipping the i values where the photon count Π_{ik} vanishes improves tremendously the execution time of the algorithm in the outer shells.

Initialization and convergence assessment

Initialization of EM algorithms is in general a critical step, since EM methods only ensure the convergence to a local maximum of the expectation value of the likelihood function. Therefore a badly-initialized algorithm may never reach a global maximum, and remain stuck in a local maximum, even with a large number of iterations.
We propose to initialize the EMC algorithm from a random perturbation of the spherical average of the measurements Π_{ik},

$$I_{ij}^{(0)} = \frac{1}{K} \sum_{k=1}^{K} \Pi_{ik} + u_{ij}, \quad u_{ij} \sim \mathcal{U}([0,1]). \tag{4.25}$$

The algorithm also needs a stopping criterion based on the evolution of the values of the reconstructed model coefficients $I_l^m(q_s)$. We evaluate the "gradient" $\Delta I_l^m(q_s)$ between two successive iterations by

$$\Delta I_l^m(q_s) = \sum_{l=0}^{L-1} \sum_{=-l}^{l} \frac{|\tilde{I}_l^m(q_s) - I_l^m(q_s)|}{|I_l^m(q_s)|}, \tag{4.26}$$

where normalizing by the previous estimate norm ensure that the stopping criterion below is independent from the total shell energy. The EMC algorithm stops when the following criterion is satisfied,

$$\Delta I_l^m(q_s) < \eta, \tag{4.27}$$

where η is typically, in our experiments, about the order of magnitude of a percent.

4.3 Full reconstruction

We have presented in the last section a simplified version of the actual reconstruction problem. We now translate this work back to the full reconstruction problem, that is the reconstruction of the three-dimensional intensity given two-dimensional diffraction patterns.

4.3.1 A 3D spherical grid

As shown in the last section, the three-dimensional reconstruction can be decomposed into a collection of two-dimensional reconstruction problems on spherical shells $s = 0, 1, \ldots$. The first question that arises is how should we choose the shells radii, so that we efficiently reconstruct the full three-dimensional intensity function at some given resolution? A natural answer to this question is to make use of the spherical Fourier-Laguerre expansion presented earlier in chapter 2.
If we fix a radial bandlimit P in the spherical Fourier-Laguerre domain, then we are given a set of P radial nodes, namely $q_0, q_1, \ldots, q_{P-1}$ defined in terms of the roots of Laguerre polynomials. If we are able to compute or estimate the spherical harmonic coefficients of the intensity function on each of these shells, we can obtain the corresponding spherical Fourier-Laguerre coefficients using the Spherical Laguerre Transform (SLT) as explained in chapter 2.
As a consequence, we choose our three-dimensional grid as follows. First, we fix the bandlimit tuple (P, L), where P is the radial bandlimit and L the angular bandlimit. Using the sampling theorem for the Spherical Fourier-Laguerre Transform, this choice gives us directly the regular grid $\mathcal{G}$,

$$\mathcal{G} \triangleq \left\{ \boldsymbol{q}_\mu(q_s, \varphi_\alpha, \theta_\alpha) \middle| \; s = 0, 1, \ldots, P-1, \; \alpha = 0, 1, \ldots, n_{\text{pix}} - 1 \right\}. \tag{4.28}$$

In the sequel, we fix $P = 8$ and we let L vary to obtain different angular bandlimits.

Remark As mentioned earlier in chapter 2, the choice of the radial bandlimit P with respect to radial resolution is a bit more complex than usual, since the radial transform is not harmonic in the Fourier sense, and because the radial nodes are not equispaced. As a consequence it is not straightforward to establish a criterion based on the Shannon-Nyquist sampling rate. We define instead a upper-bound P^{lim} based on the definition of the radial resolution (2.68) and on the detector geometric properties. In short, the upper bound P^{lim} corresponds to the maximum value of P such that the two conditions below are satisfied simultaneously:

$$\Delta q = \min_{0 \leq i < j < P} |q_i - q_j| > \Delta q(\text{inter pixels}) \quad \text{and} \quad q_0 > q(\text{first pixel}). \tag{4.29}$$

We note eventually that with the detector parameters used in our simulations (see appendix A for more details) the upper-bound is given by $P = P^{\text{lim}} = 8$, corresponding to choice made throughout the sequel.

4.3.2 Pixels contributing to a shell

Since rotations are isometries, the intensity measured at a given pixel i for an arbitrary rotation of the molecule lies on a spherical shell of radius q_i. For a ring on the detector of width $2\varepsilon_{\text{radial}}$, the measured intensities lie within a spherical volume of same width.
In the present setting with $P = 8$, we are given a radial sampling scheme $q_0, q_1, \ldots, q_7$. The radial nodes are drawn on figure 4.4. We are now interested in the determination of the contributing pixels

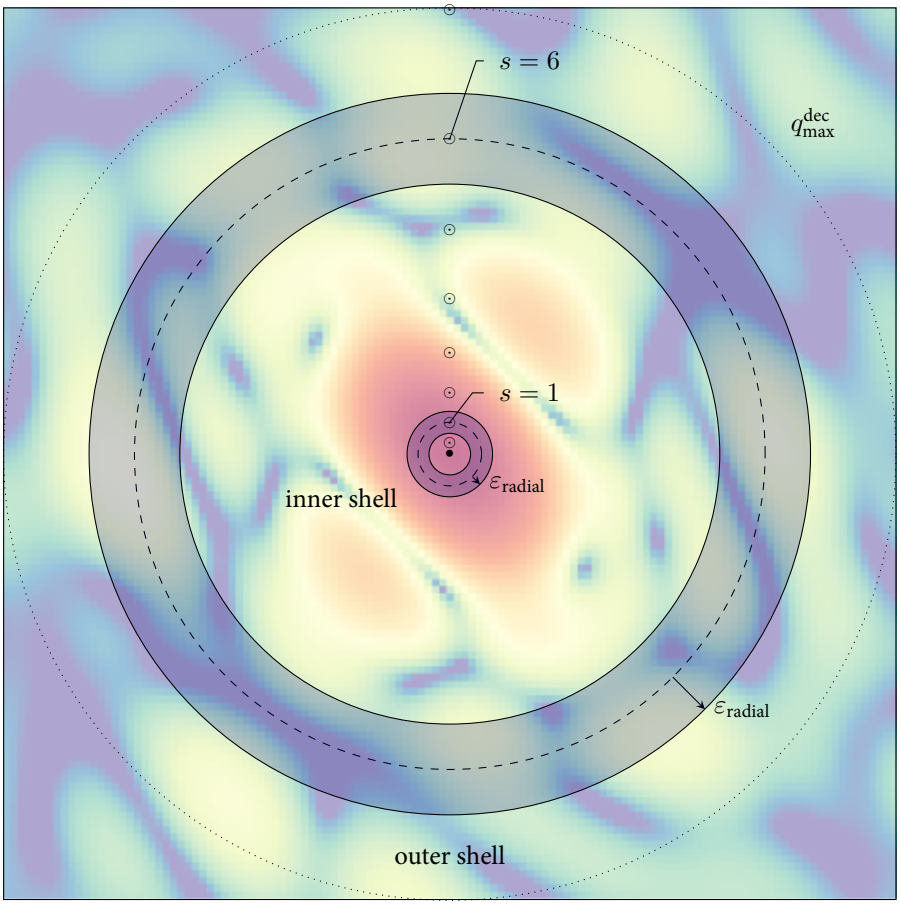

Figure 4.4 : Selection of detector pixels with the considered shell for $P = 8$.

i to the shell s. The specificity of the radial nodes lies in their non-uniform distribution, and therefore no natural choice is available. However, since it appears that the spacing between nodes increases as we go towards the outer shells, we postulate that a convenient choice for the pixels contributing to the shell s is such that the ring half-width $\varepsilon_{\text{radial}}$ is equal to

$$\varepsilon_{\text{radial}} \triangleq \frac{1}{2}\left(q_s - q_{s-1}\right),\ s \geq 1, \quad \varepsilon_{\text{radial}} \triangleq \frac{1}{2}(q_1 - q_0),\ s = 0. \tag{4.30}$$

This particular choice of $\varepsilon_{\text{radial}}$ ensures that there is no overlap between the shells, that is there is no pixel contribution to two consecutive shells. In figure 4.4 we represented the pixels contributing to shells $s = 1$ and $s = 6$, respectively. We notice that a consequence of the radial Laguerre sampling is that the ring width increases with the shell index. Also, we have far more pixels contributing to the outer shell $s = 6$ than the inner shell $s = 1$, with $N_{\text{shell}} = 3428$ pixels and $N_{\text{shell}} = 76$ pixels respectively. It is interesting that the higher number of pixels in the outer shell is balancing the fewer photons, and conversely the fewer pixels are balancing the high photon counts in the inner shell part.

4.3.3 Iterative shell by shell reconstruction

The algorithm presented in section 4.2 was, by simplicity, only described on a single spherical shell. However since the goal is to reconstruct the three-dimensional intensity function, we have to expand the same approach to the whole set of shells that constitute the grid $\mathcal{G}$.
At first, a naive approach would lead us to the following reasoning. Since it is possible to perform a spherical EMC on each single shell, why not performing separately P spherical EMC algorithms on each of these shells that constitute the grid $\mathcal{G}$? Given that computation time is critical in this setting, one would greatly take advantage of this induced parallelization property. This proposition however eclipses an intrinsic property of the EMC algorithm, that is it converges to a randomly oriented shell. This feature corresponds to the fact that a "rotated" intensity shell has the same likelihood that the

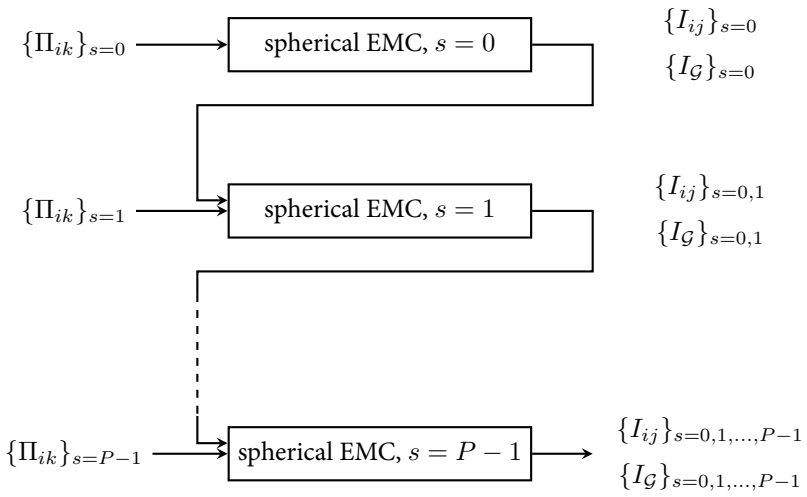

Figure 4.5 : Proposed iterative shell-by-shell EMC algorithm based on the cascade of single shell EMC.

"non-rotated" version, therefore running separately the spherical EMC algorithms on the spherical shells does not ensure that these shells are angularly aligned.
This first approach may be however useful in the future if an efficient way to re-align the shells can be formulated, thus allowing an efficient parallelization property.
The three-dimensional reconstruction algorithm presented here does not exhibit the same drawback as our first naive proposition, and still builds upon the EMC algorithm on a single shell. The main idea is to work iteratively, from the inner shells to the outer shells, and such that the reconstructed model grows with every new shell. To simplify the reasoning, we consider the same angular grid resolution on every shell, that is $L_s = L$ for all shells s.
We start by the first shell ($s = 0$) and perform the spherical EMC algorithm on this shell, as described in section 4.2. Once the algorithm has converged, we store both the values of the reconstructed model on this shell $I_{\mathcal{G}}$ and of the tomographic intensities on this shell I_{ij}. The second shell ($s = 1$) is now computed as before, at the exception that the maximization step is now different. To ensure that the shells are aligned, the computation of the probabilities P_{jk} is done on the tomographic model composed of the first shell and of the second shell, instead of being computed on the second shell only. The update however only concerns the current shell, which also ensures the coherence of the model with the previous estimated shells. The other shells are computed using the same method, and the EMC algorithm grows in complexity as we move to the outer shells. The principle of this iterative shell-by-shell EMC algorithm is depicted in figure 4.5.
We note that this method is made possible by the fact that the tomographic models for two consecutive shells do not overlap, which is a consequence of the choice of the pixels contributing to one shell developed earlier in section 4.2.

Remark In the iterative shell-by-shell version introduced here, the spherical grid resolution is the same for every shell. In practice, since the energy distribution of the coefficients widens as we go to the outer shells, one may want to adapt the spherical grid resolution with the spherical shell considered. Such a refinement is possible in the present context, by adjusting the size of the previous tomographic grid accordingly with the current shell tomographic grid.

4.4 Results

In this section, we present some numerical results which validate our spherical geometry approach to the EMC algorithm. We start by introducing an appropriate error metric, and we present a detailed statistical analysis of the spherical EMC algorithm. Finally we show an example of a three-dimensional low-resolution reconstruction using the iterative EMC scheme proposed in the last section.
All simulations presented here were performed for a Bence-Jones protein (PDB entry: 1REI), which has a molecular weight of 24 kDa. This molecule is relatively small, which helps making the simulation

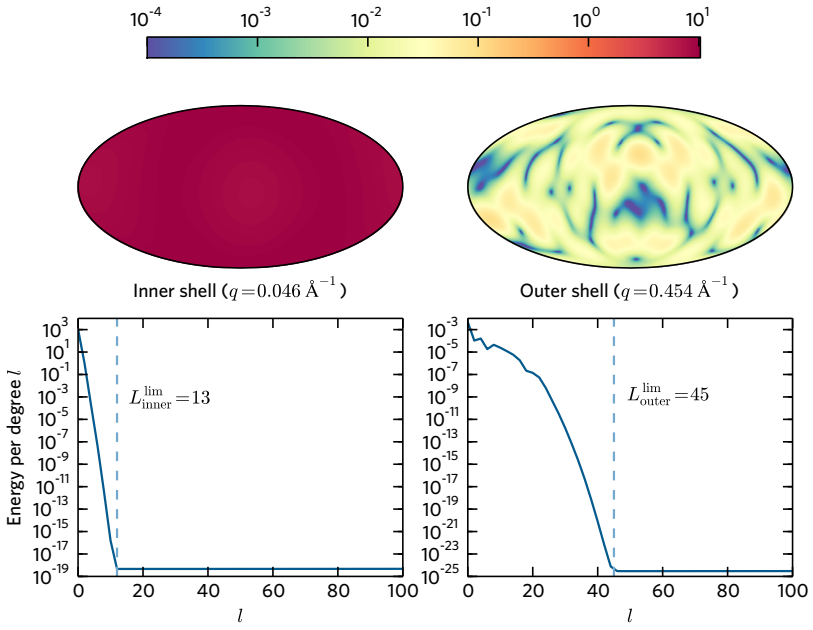

Figure 4.6 : Energy distribution in the spherical harmonic domain for the inner shell ($s = 1$) and the outer shell ($s = 6$), in the case $P = 8$ for the Bence-Jones protein. The distribution is wider in the outer shell case, with a lower total energy than in the inner shell case, as expected.

of a large number of diffraction patterns more tractable.

4.4.1 Evaluation of the reconstruction accuracy

We recall that the spherical EMC algorithm presented in this manuscript is an iterative update of the spherical harmonic coefficients $I_l^m(q_s)$ where q_s is the radius of the shell s. In the full reconstruction problem the shell index s ranges from $s = 0, 1, \ldots, P-1$ where P is the radial bandlimit whereas s is fixed in the single shell framework.

To perform a statistical performance analysis of the proposed spherical EMC algorithm, an appropriate error metric has to be introduced. Such a metric has various requirements to fulfill, namely (i) it has to be a rotation-invariant metric, because each estimate of the intensity function has a different orientation than the "true" intensity function, as mentioned earlier, (ii) it has to separate the contribution of each degree l in the spherical harmonic decomposition and (iii) it has to be normalized so that it corresponds to a *relative* error.

We propose an error metric agreeing with the points (i)–(iii) as follows. We define the *relative error per degree* l on the shell s as

$$\varepsilon_l = \frac{|\hat{E}_l - E_l|}{E_l}, \quad E_l = \sum_{m=-l}^{l} |I_l^m(q_s)|^2 \tag{4.31}$$

where $\hat{E}_l$ and E_l are respectively the estimated and theoretical energy of degree l. The normalization ensures that ε_l is a relative quantity, allowing the comparison between shells with different energy per degree. The terms E_l and $\hat{E}_l$ are rotation-invariant, as explained earlier in chapter 2.

4.4.2 Single shell reconstruction statistical analysis

In this section we look at the reconstruction performance of the spherical EMC algorithm for two typical cases. We consider the inner and outer shells depicted in figure 4.6, computed from the structure of the Bence-Jones protein. For both shells we evaluated the energy distribution in the spherical harmonic domain, and to avoid any aliasing phenomenon, the theoretical intensity functions were computed on a large spherical grid $\mathcal{G}$ with resolution parameter $n_{\text{side}} = 128$, allowing the accurate evaluation of the spherical harmonic coefficients up to degree $l = 256$.

We note that we have removed the odd degrees of l in figure 4.6 since the energy is equal to zero thanks to the Friedel symmetry (2.70). In both inner and outer shell cases, the distribution of the energy per degree reaches machine precision once the threshold L^{lim} is attained. This shows that the choice $n_{\text{side}} = 128$ respects the sampling theorem on the sphere.
As expected, the energy per degree distribution is wider in the outer shell than in the inner shell, with threshold values $L^{\text{lim}}_{\text{outer}} = 45$ and $L^{\text{lim}}_{\text{inner}} = 13$, respectively. We note as well that the total energy in the outer shell is much lower than in the inner shell, as shown by the low-photon counts in the outer parts.

Procedure

The goal here is to obtain the average behavior of the spherical EMC algorithm as the number of patterns K (observations) increases. The procedure is as follows: first, we fix a bandlimit L, which is typically $L = 3$ and $L = 5$ in our case, that is we are interested in low-resolution reconstructions. Moreover, we choose the adequate rotation group sampling with our optimality criterion given in table 4.1. Now, for a given number of patterns K, we simulate K uniform random rotations $\boldsymbol{R}_k \sim \mathcal{U}(SO(3))$ to obtain the sample points $\mathcal{D}^s_{\boldsymbol{R}_k}$, and the measurements Π_{ik} are obtained by the Poisson model described in section 4.2.1. The algorithm is initialized at random using the procedure described in section 4.2.3 and the values of the spherical harmonics coefficients $I^m_l(q_s)$ are stored after convergence of the algorithm. We finally compute the error ε_l.
The average behavior of the algorithm is obtained by *quasi*-Monte Carlo method, and with $N_{\text{MC}} = 100$ runs. Indeed, the computational cost of the algorithm prevents us from using a large number of Monte-Carlo iterations to obtain the average behavior.
We now discuss the results obtained for the inner and outer shells, in the case of low-resolution reconstruction with $L = 3$ and $L = 5$, that is the rotation group sampling sets are chosen to be the tetrahedron-based rotation group sampling $\mathcal{X}_T$ and the icosahedron-based rotation group sampling $\mathcal{X}_I$, respectively. In this case, the appropriate resolution parameter choices for the HEALPix spherical grid are $n_{\text{side}} = 1$ and $n_{\text{side}} = 2$.

Discussion of the simulation results

In figure 4.7, one can see the convergence of the estimation of the spherical harmonic coefficients for $L = 3$ and $L = 5$ as a function of the number of diffraction patterns, in both inner and outer shell cases. For the inner shell, depicted in the top row, the relative error per degree ε_l is low for $l = 0$ and $l = 2$ for the two low-resolutions ($L = 3$ and $L = 5$). We note that the case $l = 4$ exhibits a large relative error, but this case is special since the relative energy contribution of the spherical harmonic coefficients of degree l is very low in the reconstruction.
For the outer shell, as shown in the bottom row of figure 4.8, convergence is achieved slower, as expected due to the sparse measurements in the outer shells.
For all cases we note that the relative error does not go to zero as the number of observations increases, and reaches instead some finite threshold. This is explained by several aspects. First, the estimation bias can arise from interpolation errors in the compression and expansion steps of the spherical EMC algorithm. More importantly, the estimation bias results from aliasing of the higher order coefficients, which are not estimated while considering low-resolution reconstructions. Indeed, we have considered the case $L \leq L^{\text{lim}}$, and therefore sampled, *i.e.* chosen the spherical grid $\mathcal{G}$ according to the value of L nor the value of L^{lim}. The resulting sub-Nyquist sampling therefore induces an aliasing phenomenon, which is unavoidable.
As the chosen reconstruction bandlimit increases, the aliasing bias is reduced, and will disappear once L is larger than the value of L^{lim} on the spherical shell considered. However in practice the value of L^{lim} can only be guessed, and it does not seem reasonable to increase brutally L to ensure there is no aliasing, since computational cost is critical in our application. We shall point out that the true quantity of interest here is not the set of coefficients $I^m_l(q_s)$ in itself, but rather the reconstructed intensity from these coefficients. The fact that they provide a sensible low-resolution approximation to the true intensity function is here the main desired property.
Figure 4.8 indeed presents reconstructions from the set of coefficients estimated in the case $K = 400$ observations, with a grid $n_{\text{side}} = 128$. A first feature of the spherical EMC algorithm emphasized here is that the reconstruction orientation is not preserved as there is no orientation reference to "fix" the reconstruction in a particular orientation.

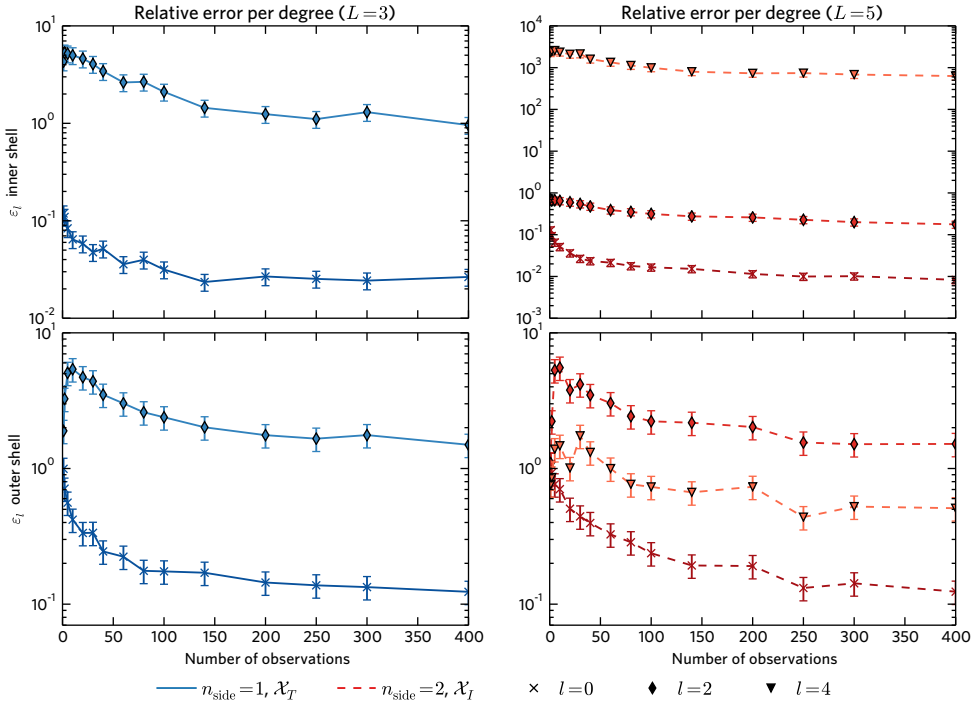

Figure 4.7 : Reconstruction error ε_l as a function of the number of observations, *i.e.* diffraction patterns. Results are presented for low-resolution reconstructions, with $L = 3$ and $L = 5$, in both inner and outer shell cases.

For the inner shell, despite the different orientations of the reconstructions, the features of the intensity function are well recovered, showing that our choice of a low-resolution reconstruction does not have a large impact on the accuracy of the reconstruction of the true intensity function. For the outer shell, we see that the low-resolution reconstructions remain quite far from the true intensity function: in that case, spherical harmonic coefficients of higher degree l would be needed to give an accurate reconstruction of the true intensity function. Nevertheless these low-resolution reconstructions provide a sensible reconstruction of a low-pass version of the true intensity function, as said earlier. Also we mention that the spherical harmonics do not ensure the positivity of the reconstructed intensity function. The possible negative values in the intensity reconstruction are set to zero to this aim. This phenomenon is typical with the outer shells, where the spherical harmonics distribution is wide and where a low-resolution reconstruction only corresponds to a small fraction of the total shell energy. This effect can be seen with the case $L = 3$ in the outer shell depicted in figure 4.8.

Finally we recall that by using a spherical harmonic decomposition of the intensity function, or more generally using any orthonormal basis, allow us to oversample the reconstruction at will (for instance here we used $n_{\text{side}} = 128$ as resolution parameter for the regular grid $\mathcal{G}$). It should allow much more flexibility for phase retrieval algorithms to be performed after intensity reconstruction.

4.4.3 A shell-by-shell low-resolution intensity reconstruction

The end of this chapter is dedicated to an example of a three-dimensional intensity reconstruction performed with the iterative shell-by-shell EMC algorithm. For computational cost, we illustrate only a low-resolution reconstructed model, but the same ideas can be transposed to higher resolutions.

We used 100 simulated diffraction patterns from the Bence-Jones protein, and such that the average number of photon per diffraction pattern is equal to 3570. The resolution of the grid was taken as $n_{\text{side}} = 2$, and we used the HEALPix rotation group sampling with $n_{\text{side}}^{\text{rot}} = 2$. The stop criterion was fixed at $\eta = 10^{-2}$. After convergence of the algorithm, we computed the spherical harmonic coefficients $I_l^m(q_s)$ and re-expanded on a larger angular grid of resolution $n_{\text{side}} = 16$. The obtained reconstruction is 5-bandlimited, and is depicted in figure 4.9, alongside the true intensity function computed for $P = 8$.

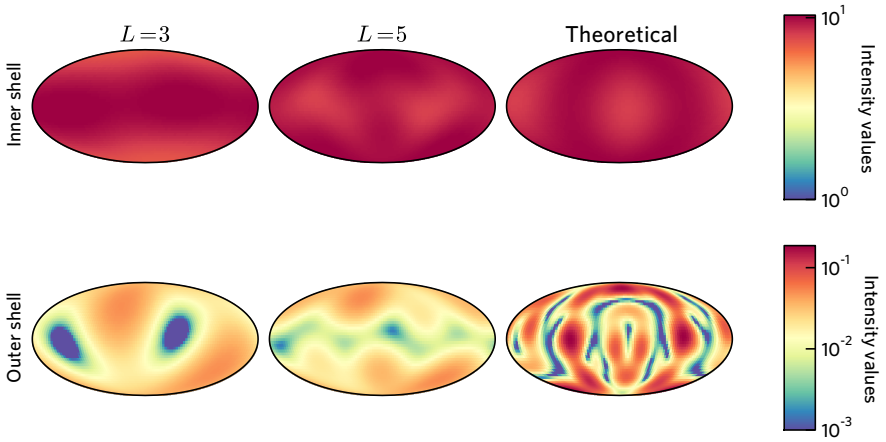

Figure 4.8 : Reconstruction in the best case error, for $K = 400$ and different bandlimits $L = 3, 5$ for inner and outer shells. The colormaps were chosen differently to highlight the proper features of each case, inner and outer shell.

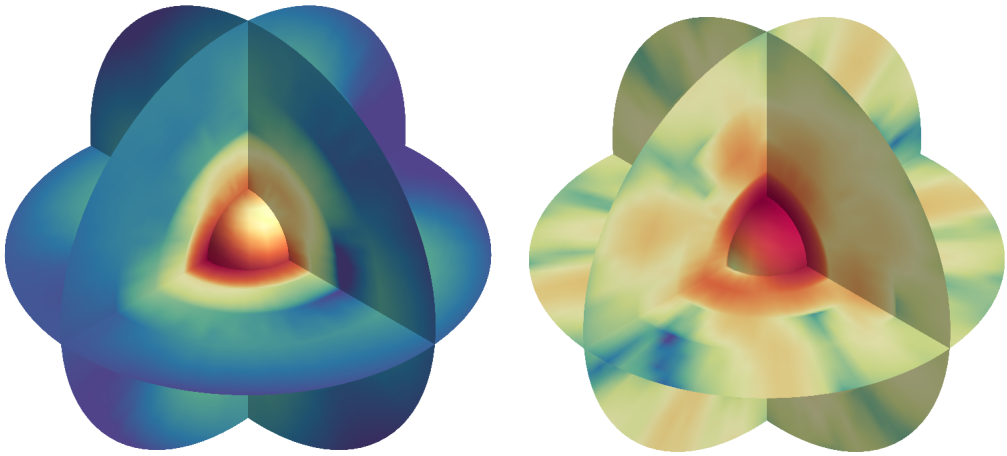

(a) (b)

Figure 4.9 : (a) Low-resolution reconstruction of the intensity function of 1REI molecule, bandlimited at $L = 5$, $P = 8$. (b) Corresponding true intensity function computed for $P = 8$.

The reconstruction exhibits slowly varying features, as expected. In the inner shell part, where the intensity function has a low bandlimit, the reconstructed intensity features are close the "true" ones. In the outer shell region however more spherical harmonic coefficient would be needed to obtain an accurate high-resolution reconstruction. We note finally that the reconstructed intensity function is rotated by some unknown rotation from the reference frame of the computed intensity function, as already mentioned in the single shell case.

CHAPTER 5

Conclusion and perspectives

5.1 Summary of contributions

The work presented in this manuscript was motivated by the three dimensional intensity reconstruction in single-particle experiments. The first aims were to study the most popular algorithm used today in three-dimensional intensity reconstructions, the Expansion-Maximization-Compression algorithm, and to rephrase it taking into account the spherical geometry of the intensity function. In chapter 1 we gave a rapid overview of the single-particle experiment Physics, and we motivated the use of a spherical geometry approach to reconstruction algorithms.
Following our motivation, we reviewed harmonic analysis on the solid sphere, *i.e.* the ball, in chapter 2. This preliminary chapter is indeed vital towards the use of sparse representations of functions defined on the three-dimensional ball. Building upon the work of Leistedt and McEwen,[44] we introduced a Spherical Fourier Laguerre Transform which allows an efficient spectral representation of three-dimensional intensity functions.
Analysis on the sphere, and by extension analysis on the ball, naturally involves working with rotations. In particular, the rotations in three-dimensional space are at the heart of the single-particle experiment. They arise from the random rotations applied to the molecule during the imaging process as well as the deterministic sampling sets on the rotation group used in the EMC algorithm. Chapter 3 studied in detail these problems, and we left aside the single-particle imaging context for a moment to obtain more general results on sampling sets and quadrature formulæ on the rotation group.
Finally, we proposed in chapter 4 to rephrase the original EMC algorithm in a spherical setting using the tools developed in chapter 2 and chapter 3. This transposition was done in two parts, we first studied in detail the spherical EMC algorithm for a single shell, and we finally make use of the spherical Laguerre radial transform to solve the full three-dimensional intensity reconstruction problem. Simulations results were presented to illustrate the feasibility of the approach.
In short, the contributions of the work presented in this manuscript are twofold: the reconstruction problem has been rephrased in a spherical setting using a sparse intensity representation, and the proposed algorithm exhibits scalability upon some radial-angular resolution tuple (P, L).

5.2 Perspectives

The work presented here can be seen as a direct extension of the EMC algorithm, rather than a complete reformulation of the reconstruction algorithm. Future work will rewrite the reconstruction algorithm using the Expectation-Maximization formalism, and make use of the spherical harmonic representation to remove the compression and expansion steps. This will result into a direct update of the spherical harmonic coefficients, while limiting the interpolation errors due to the compression and expansion steps.
The next idea to explore comes from the distribution of the radial nodes with the discrete spherical Laguerre transform. Indeed, as the radial bandlimit P increases the distribution of radial nodes becomes more concentrated towards the origin. This is a main drawback, for two principal reasons. First it appears that in the actual single-particle experiments the center of the diffraction pattern is not measured, to avoid the detector to measure the huge amount of unscattered photons. This central region corresponds to the $q \simeq 0$ values, and therefore at large P one may have nodes located in the *masked* region. On the other hand, the intensity function varies slowly in the vicinity of the origin, therefore having a lot of nodes in this region would provide a redundant description. We think that an algorithm working with spherical shells defined at arbitrary nodes would be more attractive in practice.

Finally, an interesting track could be to investigate other estimations approaches: sparsity-based, such as wavelets decomposition of the intensity function, or kernel density estimators on the sphere. Both ideas arise from the speckle structure in the outer shells, where the intensity function is very localized. Hope is that these descriptions of the intensity function will overcome the performance of the direct spherical harmonics approach.

APPENDIX A

Simulation of diffraction patterns

We give here some details about the evaluation of the intensity measured on the pixelated detector, given by equation (1.13). We recall the expression of the intensity, at reciprocal coordinates $\boldsymbol{q}$ for a rotation of the molecule $\boldsymbol{R}_k$,

$$I(\boldsymbol{q}, \boldsymbol{R}_k) = \left| \sum_j f_j(q) \exp\left(i\boldsymbol{q} \cdot (\boldsymbol{R}_k \boldsymbol{r}_j)\right) \right|^2 I_T \Delta\Omega, \tag{A.1}$$

where f_j is the scattering factor of atom j, $\boldsymbol{r}_j$ is the position vector of the j-th atom, I_T is the Thomson scattering intensity (see below), and $\Delta\Omega$ is the solid angle subtended by the detector pixel whose reciprocal coordinates are given by $\boldsymbol{q}$. In the following, we derive the expression of the solid angle $\Delta\Omega$, and we give the expression of the Thomson scattering intensity for our simulations.

A.1 Expression of the solid angle

By definition, the solid angle $\Delta\Omega$ subtended by a surface $\mathcal{S}$ is given in spherical coordinates by

$$\Delta\Omega = \iint_{\mathcal{S}} \sin\theta \mathrm{d}\theta \mathrm{d}\varphi. \tag{A.2}$$

In general, $\mathcal{S}$ corresponds to a spherical cap on the sphere. However, in our case the detector is located in the far field, and therefore we can approximate $\mathcal{S}$ by a square surface. We introduce $\delta = p_w / z_D \ll 1$, where p_w is the pixel size and z_D is the sample-detector distance. The integration bounds are now given by $[\theta_0 - \delta/2, \theta_0 + \delta/2]$ for the angle θ, and $[\varphi_0\delta/2, \varphi_0 + \delta/2]$ for the angle φ, where $(\theta_{\text{sc}}, \varphi_{\text{sc}})$ are the spherical coordinates in physical space of the considered pixel. We can now write $\Delta\Omega$ as

$$\begin{aligned}
\Delta\Omega &= \int_{\theta_0-\delta/2}^{\theta_0+\delta/2} \int_{\varphi_0-\delta/2}^{\varphi_0+\delta/2} \sin\theta \mathrm{d}\theta \mathrm{d}\varphi && \text{(A.3)}\\
&= \delta \left[\cos\theta\right]_{\theta_0-\delta/2}^{\theta_0+\delta/2} && \text{(A.4)}\\
&= \delta \left[\cos\left(\theta_0 + \delta/2\right) - \cos\left(\theta_0 - \delta/2\right)\right] && \text{(A.5)}\\
&= 2\delta \sin\theta_0 \sin\delta/2 && \text{(A.6)}\\
&\simeq \delta^2 \sin\theta_0 && \text{(A.7)}
\end{aligned}$$

Now, some simple scattering geometry yields to the relation $\theta_{\text{sc}}(q) = \pi/2 - \theta_0$, and hence we have the result

$$\Delta\Omega \simeq \left(\frac{p_w}{z_D}\right)^2 \cos\theta_{\text{sc}}(q). \tag{A.8}$$

A.2 Simulation parameters

The Thomson intensity corresponds to the intensity scattered by a free electron under the same incoming beam conditions as those used in the actual experiments. Its expression is given in 1.2, which we recall here

$$I_T = \pi r_e^2 \mathcal{P}(\theta_{\text{sc}}) I_0, \tag{A.9}$$

Parameter	Value	Unit
n_{photons}	10^{13}	-
S	10	μm^2
p_w	3.38×10^{-5}	m
z_D	10^{-2}	m

Table A.1 : Numerical values of the simulation parameters.

where $r_e = 2.82\ 10^{-15}$ m is the classical radius of the electron, $\mathcal{P}(\theta_{\text{sc}})$ is a function depending of the polarization of the incoming beam, and I_0 is the incoming beam intensity. The latter quantity is defined as the ratio of the number of photons n_{photons} in one pulse by the beamarea S. For simplicity, we consider $\mathcal{P}(\theta_{\text{sc}}) = 1$, that is the polarization is set in the plane perpendicular to the scattering direction. Finally, we give the practical expression of the scattered intensity measured on the detector,

$$I(\boldsymbol{q}, \boldsymbol{R}_k) = \left| \sum_j f_j(q) \exp\left(i\boldsymbol{q} \cdot (\boldsymbol{R}_k \boldsymbol{r}_j)\right) \right|^2 \frac{\pi r_e^2}{S} n_{\text{photons}} \left(\frac{p_w}{z_D}\right)^2 \cos\theta_{\text{sc}}(q). \tag{A.10}$$

The numerical values of simulation parameters used for our experiments are given explicitly in table A.1.

Bibliography

1. Anton Barty, Jochen Küpper, and Henry N Chapman. Molecular imaging using X-ray free-electron lasers. *Annual review of physical chemistry*, **64**: 415–435, 2013. (see pp. 1, 13)
2. VL Shneerson, A Ourmazd, and DK Saldin. Crystallography without crystals. I. The common-line method for assembling a three-dimensional diffraction volume from single-particle scattering. *Acta Crystallographica Section A: Foundations of Crystallography*, **64**: 303–315, 2008. (see pp. 1, 13)
3. Weilun Chao, Bruce D Harteneck, J Alexander Liddle, Erik H Anderson, and David T Attwood. Soft X-ray microscopy at a spatial resolution better than 15 nm. *Nature*, **435**: 1210–1213, 2005. (see p. 1)
4. D. Sayre and H. N. Chapman. X-ray microscopy. *Acta Crystallographica Section A*, **51**: 237–252, 1995. (see p. 1)
5. D. Sayre, H. N. Chapman, and J. Miao. On the Extendibility of X-ray Crystallography to Non-crystals. *Acta Crystallographica Section A*, **54**: 232–239, 1998. (see p. 1)
6. Henry N Chapman, Anton Barty, Stefano Marchesini, Aleksandr Noy, Stefan P Hau-Riege, Congwu Cui, Malcolm R Howells, Rachel Rosen, Haifeng He, John CH Spence, et al. High-resolution ab initio three-dimensional x-ray diffraction microscopy. *JOSA A*, **23**: 1179–1200, 2006. (see pp. 1, 9, 10, 12)
7. Andrew V Martin and Ne-Te Duane Loh. X-ray Free-Electron Lasers: Illuminating a New Path to Single Particle Imaging. *Synchrotron Radiation News*, **26**: 11–19, 2013. (see p. 1)
8. KJ Gaffney and HN Chapman. Imaging atomic structure and dynamics with ultrafast X-ray scattering. *Science*, **316**: 1444–1448, 2007. (see p. 1)
9. Richard Neutze, Remco Wouts, David van der Spoel, Edgar Weckert, and Janos Hajdu. Potential for biomolecular imaging with femtosecond X-ray pulses. *Nature*, **406**: 752–757, 2000. (see p. 2)
10. Andrew V Martin, Justine K Corso, Carl Caleman, and Harry M Quiney. Single molecule imaging with longer x-ray laser pulses. *arXiv preprint arXiv:1502.00737*, 2015. (see p. 2)
11. Robin Santra. Concepts in x-ray physics. *Journal of Physics B: Atomic, Molecular and Optical Physics*, **42**: 023001, 2009. (see p. 3)
12. David M Paganin. *Coherent X-ray optics*. Oxford University Press, 2006. (see pp. 4, 6)
13. M. H. Pirenne. *The diffraction of X-Rays and electrons by free molecules*. Cambridge University Press, 1946. (see p. 4)
14. Bertram Eugene Warren. *X-ray Diffraction*. Courier Dover Publications, 1969. (see p. 4)
15. Theo Hahn, Uri Shmueli, Arthur James Cochran Wilson, and Edward Prince. *International tables for crystallography*. D. Reidel Publishing Company, 2005. (see p. 4)
16. D Waasmaier and A Kirfel. New analytical scattering-factor functions for free atoms and ions. *Acta Crystallographica Section A: Foundations of Crystallography*, **51**: 416–431, 1995. (see p. 4)
17. Don T Cromer and Joseph B Mann. X-ray scattering factors computed from numerical Hartree–Fock wave functions. *Acta Crystallographica Section A: Crystal Physics, Diffraction, Theoretical and General Crystallography*, **24**: 321–324, 1968. (see p. 5)
18. Arthur James Cochran Wilson. *Elements of X-ray Crystallography*. Addison-Wesley Reading, Massachusetts, 1970. (see p. 6)
19. Kerstin Braig, Zbyszek Otwinowski, Rashmi Hegde, David C Boisvert, Andrzej Joachimiak, Arthur L Horwich, and Paul B Sigler. The crystal structure of the bacterial chaperonln GroEL at 2.8 Å. *Nature*, 1994. (see pp. 9, 11)

20. OTTO EPP, EATON E LATTMAN, MARIANNE SCHIFFER, ROBERT HUBER, and WALTER PALM. Molecular structure of a dimer composed of the variable portions of the Bence-Jones protein REI refined at 2.0-Å resolution. *Biochemistry*, **14**: 4943–4952, 1975. (see p. 9)

21. PIERRE THIBAULT and IVAN C RANKENBURG. Optical diffraction microscopy in a teaching laboratory. *American Journal of Physics*, **75**: 827–832, 2007. (see p. 9)

22. M PORRO, L ANDRICEK, L BOMBELLI, G DE VITA, C FIORINI, P FISCHER, K HANSEN, P LECHNER, G LUTZ, L STRÜDER, et al. Expected performance of the DEPFET sensor with signal compression: A large format X-ray imager with mega-frame readout capability for the European XFEL. *Nuclear Instruments and Methods in Physics Research Section A: Accelerators, Spectrometers, Detectors and Associated Equipment*, **624**: 509–519, 2010. (see p. 12)

23. G HULDT, A SZŐKE, and JANOS HAJDU. Diffraction imaging of single particles and biomolecules. *Journal of structural biology*, **144**: 219–227, 2003. (see p. 13)

24. RUSSELL FUNG, VALENTIN SHNEERSON, DILANO K SALDIN, and ABBAS OURMAZD. Structure from fleeting illumination of faint spinning objects in flight. *Nature Physics*, **5**: 64–67, 2009. (see p. 13)

25. DK SALDIN, VL SHNEERSON, R FUNG, and A OURMAZD. Structure of isolated biomolecules obtained from ultrashort X-ray pulses: exploiting the symmetry of random orientations. *Journal of Physics: Condensed Matter*, **21**: 134014, 2009. (see p. 13)

26. DMITRI STARODUB, ANDREW AQUILA, SAŠA BAJT, MIRIAM BARTHELMESS, ANTON BARTY, CHRISTOPH BOSTEDT, JOHN D BOZEK, NICOLA COPPOLA, R BRUCE DOAK, SASCHA W EPP, et al. Single-particle structure determination by correlations of snapshot X-ray diffraction patterns. *Nature communications*, **3**: 1276, 2012. (see pp. 13, 31)

27. NE-TE DUANE LOH and VEIT ELSER. Reconstruction algorithm for single-particle diffraction imaging experiments. *Physical Review E*, **80**: 026705, 2009. (see pp. 13, 15, 49, 50)

28. TOMAS EKEBERG, MARTIN SVENDA, CHANTAL ABERGEL, FILIPE RNC MAIA, VIRGINIE SELTZER, JEAN-MICHEL CLAVERIE, MAX HANTKE, OLOF JÖNSSON, CARL NETTELBLAD, GIJS VAN DER SCHOT, et al. Three-dimensional reconstruction of the giant mimivirus particle with an x-ray free-electron laser. *Physical review letters*, **114**: 098102, 2015. (see pp. 13, 49)

29. MICHAŁ WALCZAK and HELMUT GRUBMÜLLER. Bayesian orientation estimate and structure information from sparse single-molecule x-ray diffraction images. *Physical Review E*, **90**: 022714, 2014. (see pp. 13, 41)

30. VEIT ELSER. Strategies for processing diffraction data from randomly oriented particles. *Ultramicroscopy*, **111**: 788–792, 2011. (see p. 13)

31. VEIT ELSER. Three-dimensional structure from intensity correlations. *New Journal of Physics*, **13**: 123014, 2011. (see p. 13)

32. DAVID SAYRE. Some implications of a theorem due to Shannon. *Acta Crystallographica*, **5**: 843–843, 1952. (see p. 14)

33. J MIAO, D SAYRE, and HN CHAPMAN. Phase retrieval from the magnitude of the Fourier transforms of nonperiodic objects. *JOSA A*, **15**: 1662–1669, 1998. (see p. 14)

34. VEIT ELSER. Phase retrieval by iterated projections. *JOSA A*, **20**: 40–55, 2003. (see p. 14)

35. STEFANO MARCHESINI, H HE, HENRY N CHAPMAN, STEFAN P HAU-RIEGE, A NOY, MALCOLM R HOWELLS, U WEIERSTALL, and JOHN CH SPENCE. X-ray image reconstruction from a diffraction pattern alone. *Physical Review B*, **68**: 140101, 2003. (see p. 14)

36. D RUSSELL LUKE. Relaxed averaged alternating reflections for diffraction imaging. *Inverse Problems*, **21**: 37, 2005. (see p. 14)

37. STEFANO MARCHESINI. Invited article: A unified evaluation of iterative projection algorithms for phase retrieval. *Review of Scientific Instruments*, **78**: 011301, 2007. (see p. 14)

38. YOAV SHECHTMAN, YONINA C ELDAR, OREN COHEN, HENRY NICHOLAS CHAPMAN, JIANWEI MIAO, and MORDECHAI SEGEV. Phase retrieval with application to optical imaging: a contemporary overview. *Signal Processing Magazine, IEEE*, **32**: 87–109, 2015. (see p. 14)

39. RODNEY A KENNEDY and PARASTOO SADEGHI. *Hilbert Space Methods in Signal Processing*. Cambridge University Press, 2013. (see p. 17)

40. ZUBAIR KHALID, RODNEY A KENNEDY, and JASON D MCEWEN. Slepian spatial-spectral concentration on the ball. *Applied and Computational Harmonic Analysis*, 2015. (see pp. 17, 21)

41. MILTON ABRAMOWITZ and IRENE A STEGUN. *Handbook of mathematical functions: with formulas, graphs, and mathematical tables*. 55 Courier Corporation, 1964. (see p. 21)

42. QING WANG, OLAF RONNEBERGER, and HANS BURKHARDT. Rotational invariance based on Fourier analysis in polar and spherical coordinates. *Pattern Analysis and Machine Intelligence, IEEE Transactions on*, **31**: 1715–1722, 2009. (see p. 21)

43. QING WANG, OLAF RONNEBERGER, and HANS BURKHARDT *Fourier analysis in polar and spherical coordinates* tech. rep. 2008 (see p. 21)

44. BORIS LEISTEDT and JASON D MCEWEN. Exact wavelets on the ball. *Signal Processing, IEEE Transactions on*, **60**: 6257–6269, 2012. (see pp. 22, 24, 25, 65)

45. FRANÇOIS LANUSSE, ANAIS RASSAT, and J-L STARCK. Spherical 3D isotropic wavelets. *Astronomy & Astrophysics*, **540**: A92, 2012. (see p. 24)

46. JACQUES DELABROUILLE, J-F CARDOSO, M LE JEUNE, M BETOULE, G FAY, and F GUILLOUX. A full sky, low foreground, high resolution CMB map from WMAP. *Astronomy & Astrophysics*, **493**: 835–857, 2009. (see p. 26)

47. A KOGUT, DN SPERGEL, C BARNES, CL BENNETT, M HALPERN, G HINSHAW, N JAROSIK, M LIMON, SS MEYER, L PAGE, et al. First-year Wilkinson microwave anisotropy probe (WMAP) observations: temperature-polarization correlation. *The Astrophysical Journal Supplement Series*, **148**: 161, 2003. (see p. 26)

48. PAR ADE, N AGHANIM, C ARMITAGE-CAPLAN, M ARNAUD, M ASHDOWN, F ATRIO-BARANDELA, J AUMONT, C BACCIGALUPI, ANTHONY J BANDAY, RB BARREIRO, et al. Planck 2013 results. XVI. Cosmological parameters. *Astronomy & Astrophysics*, **571**: A16, 2014. (see p. 26)

49. JM LAMARRE, JL PUGET, FREDDY BOUCHET, PETER AR ADE, A BENOIT, JP BERNARD, J BOCK, P DE BERNARDIS, J CHARRA, F COUCHOT, et al. The Planck High Frequency Instrument, a third generation CMB experiment, and a full sky submillimeter survey. *New Astronomy Reviews*, **47**: 1017–1024, 2003. (see p. 26)

50. DAVID N SPERGEL, LICIA VERDE, HIRANYA V PEIRIS, E KOMATSU, MR NOLTA, CL BENNETT, M HALPERN, G HINSHAW, N JAROSIK, A KOGUT, et al. First-year Wilkinson Microwave Anisotropy Probe (WMAP) observations: determination of cosmological parameters. *The Astrophysical Journal Supplement Series*, **148**: 175, 2003. (see p. 26)

51. J.-F. CARDOSO. Precision cosmology with the cosmic microwave background. *IEEE Signal Processing Magazine*, **27**: 55–66, 2010. (see p. 26)

52. JAMES R DRISCOLL and DENNIS M HEALY. Computing Fourier transforms and convolutions on the 2-sphere. *Advances in applied mathematics*, **15**: 202–250, 1994. (see p. 26)

53. JASON D MCEWEN and YVES WIAUX. A novel sampling theorem on the sphere. *Signal Processing, IEEE Transactions on*, **59**: 5876–5887, 2011. (see p. 27)

54. AG DOROSHKEVICH, PD NASELSKY, OLEG V VERKHODANOV, DI NOVIKOV, VI TURCHANINOV, ID NOVIKOV, PR CHRISTENSEN, and L-Y CHIANG. Gauss–Legendre sky pixelization (GLESP) for CMB maps. *International Journal of Modern Physics D*, **14**: 275–290, 2005. (see p. 27)

55. ROBERT G CRITTENDEN and NEIL G TUROK. Exactly azimuthal pixelizations of the sky. *arXiv preprint astro-ph/9806374*, 1998. (see p. 27)

56. KRZYSZTOF M GORSKI, ERIC HIVON, AJ BANDAY, BENJAMIN D WANDELT, FRODE K HANSEN, MSTVOS REINECKE, and MATTHIA BARTELMANN. HEALPix: a framework for high-resolution discretization and fast analysis of data distributed on the sphere. *The Astrophysical Journal*, **622**: 759, 2005. (see pp. 27, 43, 48, 55)

57. NASA *anafast reference and documentation* June 2010 URL: http://healpix.jpl.nasa.gov/html/facilitiesnode7.htm (see p. 29)

58. MANUEL GRÄF, STEFAN KUNIS, and DANIEL POTTS. On the computation of nonnegative quadrature weights on the sphere. *Applied and Computational Harmonic Analysis*, **27**: 124–132, 2009. (see p. 29)

59. ROGER G NEWTON. *Scattering theory of waves and particles*. Springer Science & Business Media, 2013. (see p. 32)

60. HEINRICH B. STUHRMANN. Interpretation of small-angle scattering functions of dilute solutions and gases. A representation of the structures related to a one-particle scattering function. *Acta Crystallographica Section A: Crystal Physics, Diffraction, Theoretical and General Crystallography*, **26**: 297–306, 1970. (see p. 32)

61. MICHAEL TINKHAM. *Group theory and quantum mechanics*. Courier Corporation, 2003. (see pp. 32, 38, 40)

62. SIMON L ALTMANN. *Rotations, quaternions, and double groups*. Courier Corporation, 2005. (see p. 37)

63. JOHN H CONWAY and DEREK A SMITH. On quaternions and octonions. *AMC*, **10**: 12, 2003. (see p. 38)

64. JULIE C MITCHELL. Sampling rotation groups by successive orthogonal images. *SIAM Journal on Scientific Computing*, **30**: 525–547, 2008. (see pp. 39, 40, 43)

65. MANUEL GRÄF and DANIEL POTTS. Sampling sets and quadrature formulae on the rotation group. *Numerical Functional Analysis and Optimization*, **30**: 665–688, 2009. (see pp. 39, 40, 43, 46, 47)

66. ASIM ORHAN BARUT and RYSZARD RACZKA. *Theory of group representations and applications*. vol. 2 World Scientific, 1986. (see p. 39)

67. SALEM SAID, CHRISTIAN LAGEMAN, NICOLAS LE BIHAN, and JONATHAN H MANTON. Decompounding on compact Lie groups. *arXiv preprint arXiv:0907.2601*, 2009. (see p. 39)

68. ANNA YERSHOVA, SWATI JAIN, STEVEN M LAVALLE, and JULIE C MITCHELL. Generating uniform incremental grids on SO (3) using the Hopf fibration. *The International journal of robotics research*, 2009. (see p. 40)

69. ANNA YERSHOVA and STEVEN M LAVALLE. "Deterministic sampling methods for spheres and SO (3)" in: *Robotics and Automation, 2004. Proceedings. ICRA'04. 2004 IEEE International Conference on*. vol. 4 IEEE 2004. 3974–3980 (see pp. 40, 43)

70. JAMES J KUFFNER. "Effective sampling and distance metrics for 3D rigid body path planning" in: *Robotics and Automation, 2004. Proceedings. ICRA'04. 2004 IEEE International Conference on*. vol. 4 IEEE 2004. 3993–3998 (see p. 41)

71. KEN SHOEMAKE. "Uniform random rotations" in: *Graphics Gems III*. Academic Press Professional, Inc. 1992. 124–132 (see p. 41)

72. PHILIP J DAVIS and PHILIP RABINOWITZ. *Methods of numerical integration*. Courier Corporation, 2007. (see p. 46)

73. LUCA BRANDOLINI, CHRISTINE CHOIRAT, LEONARDO COLZANI, GIACOMO GIGANTE, RAFFAELLO SERI, and GIANCARLO TRAVAGLINI. Quadrature rules and distribution of points on manifolds. *Annali della Scuola Normale Superiore di Pisa Classe di Scienze*, **13**: 889–923, 2014. (see p. 46)

74. KENDALL ATKINSON. Numerical integration on the sphere. *The Journal of the Australian Mathematical Society. Series B. Applied Mathematics*, **23**: 332–347, 1982. (see p. 46)

75. OSCAR L COLOMBO *Numerical methods for harmonic analysis on the sphere* tech. rep. DTIC Document, 1981 (see p. 46)

76. MANUEL GRÄF. *Efficient algorithms for the computation of optimal quadrature points on riemannian manifolds*. 2013. (see p. 46)

77. VYACHESLAV IVANOVICH LEBEDEV. Quadratures on a sphere. *USSR Computational Mathematics and Mathematical Physics*, **16**: 10–24, 1976. (see p. 46)

78. VI LEBEDEV and DN LAIKOV. "A quadrature formula for the sphere of the 131st algebraic order of accuracy" in: *Doklady. Mathematics*. vol. 59 3 MAIK Nauka/Interperiodica 1999. 477–481 (see p. 46)

79. YIMING HONG. On Spherical t-designs in ⊠ 2. *European Journal of Combinatorics*, **3**: 255–258, 1982. (see pp. 47, 48)

80. ARTHUR P DEMPSTER, NAN M LAIRD, and DONALD B RUBIN. Maximum likelihood from incomplete data via the EM algorithm. *Journal of the royal statistical society. Series B (methodological)*, 1–38, 1977. (see p. 49)

81. John Horton Conway and Neil James Alexander Sloane. *Sphere packings, lattices and groups*. vol. 290 Springer Science & Business Media, 2013. (see p. 52)

82. Harold Scott Macdonald Coxeter. *Regular polytopes*. Courier Corporation, 1973. (see p. 52)